UNIVERSITY OF CALIFORNIA
SANTA CRUZ

STAR FORMATION IN GRAVITATIONALLY UNSTABLE DISK GALAXIES: FROM CLOUDS TO DISKS

A dissertation submitted in partial satisfaction of the
requirements for the degree of

Doctor of Philosophy

in

ASTRONOMY & ASTROPHYSICS

by

Nathan J. Goldbaum

September 2015

The Dissertation of Nathan J. Goldbaum
is approved:

Professor Mark R. Krumholz, Chair

Professor J. Xavier Prochaska

Professor Joel R. Primack

Tyrus Miller
Vice Provost and Dean of Graduate Studies

Contents

List of Figures

List of Tables

Abstract

Star Formation in Gravitationally Unstable Disk Galaxies: From Clouds to Disks

by

Nathan J. Goldbaum

In Part I, I examine the dynamics of giant molecular clouds through simplified semianalytic models. I focus on the growth of clouds as they accrete gas. Our model clouds reproduce the scaling relations observed in both galactic and extragalactic clouds: clouds attain virial equilibrium and grow maintaining roughly constant surface densities, $\Sigma \simeq 50$–$200\ M_\odot\ pc^{-2}$ and that clouds grow along the well-known linewidth-size relation. We compare our models to observations of giant molecular clouds and associated young star clusters in the Large Magellanic Cloud, finding good agreement between our models and the relationship between H II regions, young star clusters, and giant molecular clouds.

The role of gravitational-instability driven turbulence in determining the structure and evolution of disk galaxies, and the extent to which gravity rather than feedback can explain galaxy properties, remains an open question. To address it, in Part II I present high resolution adaptive mesh refinement simulations of Milky Way-like isolated disk galaxies, including realistic heating and cooling rates and a physically motivated prescription for star formation. The simulations resolve densities typical of the transition from atomic to molecular hydrogen, capturing the formation of gravitationally bound clouds. We present simulations both with and without stellar feedback from Type II

supernova blast waves. We find gravitational instability alone can drive substantial turbulence in galactic disks and reproduce some properties of nearby star forming galaxies: $Q_{\rm total} \gtrsim 1$, $c_{\rm eff} \sim 10$ km/s, without stellar feedback. Including feedback produces an ISM with a structure similar to observed disks, with the bulk of the gas in the warm or cold atomic phase, and the remainder locked up in short-lived gravitationally bound clouds. We investigate radial flows of gas and find that radial migration of gas due to gravitational instability can supply a substantial fraction of the gas needed for star formation in the inner parts of star forming galaxies.

Dedicated to my grandmother, Ruth Turner, who always believed in me.

Acknowledgments

My sincerest thanks to my thesis advisor Mark Krumholz, who helped guide me through turbulent patches in my PhD experience with ease and confidence. This work would not have been possible without his support, feedback, and advice. I would also like to thank my dissertation committee members, J. Xavier Prochaska and Joel Primack for serving on my committee and offering productive and useful feedback.

I would like to thank the graduate students, postdocs, and faculty in Astronomy & Astrophysics department at the University of California Santa Cruz. I have been offered generous support, help with a smile, and a amiable, collegial atmosphere for the past six years. In particular, I would like to thank my the students in my cohort, Rosalie McGurk, Angie Wolfgang, Jerome Fang, and Claire Dorman. I also thank my officemate Elizabeth Lovegrove for putting up with me while I finished my thesis and for offering an obliging ear and sharp eye for a nice plot. I received mentorship, good advice, stimulating conversations and excellent company from many graduate students, but would particularly like to thank Robert da Silva, Valery Rashkov, Anne Medling, Maria Duran, Michele Fumagalli, James Guillochon, Kevin Schlaufmann, and Stefano Meschiari for advice and mentorship during my first few years as a graduate student.

I would like to thank the `yt` and `enzo` development community for their help, advice, and support in my modifications and contributions to these codebases. I would not have been able to perform the simulations described in Chapter 3 and 4 if these codes were not Free Software with communities committed to open science. I would particularly like to thank Matthew Turk, Britton Smith, John Wise, Cameron Hummels,

John ZuHone, Sam Skillman, Christine Simpson, Greg Bryan, Brian O'Shea, Tom Abel, and Mike Norman.

Paper Acknowledgments

The text of this dissertation includes reprints of the following published and in-preparation material by Nathan Goldbaum: Goldbaum et al. (2011), Goldbaum et al. (2015, in prep.a), Goldbaum et al. (2015, in prep.b).

The contents of Goldbaum et al. (2011) make up part of Chapter 1 and all of Chapter 2. I was responsible for the necessary code modifications and additions in `gmcevol`, for writing the bulk of the text and producing all of the figures. I would like to thank my co-authors Mark Krumholz, Chris Matzner, and Chris McKee for their support and permission to reuse materials from the paper for my dissertation.

The contents of Goldbaum et al. (2015, in prep.a) and Goldbaum et al. (2015, in prep.b) make up part of Chapter 1 and all of Chapter 3 and 4. I was responsible for implementing the isolated galaxy problem initializer, star formation implementation, and the momentum supernova feedback implementation to the `enzo` code, running the simulations, writing the analysis code, writing the bulk of the text and producing all of the figures. I would like to thank my co-authors Mark Krumholz and John Forbes for their permission to reuse materials from the papers for my dissertation.

Science Acknowledgments

This material is based in part upon work supported by the National Science Foundation under award numbers AST-0807739, AST-0955300, AST-1405962, and

NASA through Astrophysics Theory and Fundamental Physics grant NNX09AK31G, TCAN grant NNX14AB52G, a Spitzer Space Telescope Theoretical Research Program grant, and Hubble Archival Research grant HST-AR-13909.

This work utilized the Hyades supercomputer at the University of California Santa Cruz, which is supported by the National Science Foundation through award AST-1229745, and the Pleiades supercomputer, which is supported by the NASA Advanced Supercomputing Division.

The computations and analysis described in this dissertation rely heavily on open source software packages, including the `Enzo`, `Python`, `yt`, `IPython`, `NumPy`, `SciPy`, `matplotlib`, `Cython`, `hdf5`, `h5py`, and `numexpr`. We thank the developer communities of these packages for their contributions.

Chapter 1

Introduction

1.1 Gravitational Instability as a Driver of Galactic Evolution

Until the past few years, most theoretical work on galaxy evolution has focused on reproducing observed correlations in the bulk properties of galaxies, such as the stellar mass-halo mass relation (e.g., Moster et al., 2013; Behroozi et al., 2013), the stellar mass-star formation relation (e.g., Daddi et al., 2007; Elbaz et al., 2007; Noeske et al., 2007), and the mass-metallicity relation (e.g., Tremonti et al., 2004; Pilyugin et al., 2004). In such correlations, galaxies are treated as single points, and theoretical models have been largely content to treat them as such. In these models, the behavior of galaxies is almost entirely dictated by a balance between cosmological accretion and feedback (e.g., Bouché et al., 2010; Lilly et al., 2013; Forbes et al., 2014b; Mitra et al., 2014), and for this reason most theoretical attention has been focused on stellar feedback as the

dominant driver of galaxy evolution. However, the recent availability of large samples of spatially-resolved maps of gas, metals, and star formation in nearby galaxies has opened up a new frontier in the study of galaxies: explaining the radial distribution of these quantities. The observational studies conducted to date have turned up a few puzzling facts that demand explanation, which cannot obviously be explained simply by a local balance of accretion versus feedback in radial bins. Instead, they point to a potentially significant role for redistribution of material by gravitational instability as a driver of ISM structure over cosmological times.

The first surprise concerns the radial distribution of gas and star formation in present-day disk galaxies. Observations show that the neutral gas in such galaxies is distributed with an approximately universal exponential profile, with typical gas scale lengths of $\sim 0.5 r_{25}$, where r_{25} is the optical radius of the galaxy (Regan et al., 2001; Schruba et al., 2011a; Bigiel & Blitz, 2012). The gas is dominated by H_2 inside $\sim 0.4 r_{25}$, while H I predominates at larger radii (e.g., Leroy et al., 2008a). The radial distribution of star formation is, to first approximation, simply linearly proportional to the H_2 distribution (Bigiel et al., 2008a; Schruba et al., 2011a; Leroy et al., 2013), so star formation is much more radially concentrated than the total neutral gas, and predominantly occurs inside $\sim 0.5 r_{25}$. In such regions, the time required to convert all the available gas to stars is ~ 2 Gyr, much less than a Hubble time (Bigiel et al., 2008a; Leroy et al., 2013). Thus the inner parts of galaxies will become gas-depleted and cease star formation unless fresh gas is supplied at an equal rate, which for L_* galaxies is a few $M_\odot$ yr^{-1} (Kennicutt & Evans, 2012). While some disk galaxies, including the Milky

Way, do have inner gas holes and quenched central star formation, such systems appear to be the exception rather than the rule among the local disk galaxy population (Bigiel & Blitz, 2012).

How the fresh gas responsible for the lack of quenched centers can be explained is an unsolved problem. Condensation of gas from the hot halo (Marinacci et al., 2010; Fraternali et al., 2013; Hobbs et al., 2013) and direct accretion of cold gas from the intergalactic medium (IGM; e.g., Kereš et al., 2005; Dekel et al., 2009b) can in principle provide enough mass, but both tend to deposit gas primarily at large galactocentric radii, far from the actively star-forming regions that need to be refueled. Gas recycling from evolved stellar populations can potentially provide some of the required mass (Leitner & Kravtsov, 2011), but, in addition to uncertainties about whether this channel provides enough mass and is consistent with various chemical evolution constraints, the radial distribution of recycled gas has not been explored. In summary, the lack of quenched, gas-depleted centers in local disk galaxies seems to require some form of gas redistribution within the disk, for which gravitational instability is an obvious candidate.

A second surprising observation regarding the radial distribution of gas concerns gas velocity dispersions. H I lines in disk galaxies show super-thermal velocity dispersions of ~ 10 km s^{-1} (e.g., van Zee & Bryant, 1999; Petric & Rupen, 2007; Tamburro et al., 2009; Ianjamasimanana et al., 2012, 2015). Velocity dispersions are highest toward the centers of galaxies, but they decline only shallowly with radius, and remain superthermal even well outside r_{25}. While star formation feedback alone appears able to drive the observed velocity dispersion in inner disks, the same is not true outside

r_{25}, where the star formation rate drops precipitously but the velocity dispersion does not (Tamburro et al., 2009; Ianjamasimanana et al., 2015). Dwarf galaxies represent an extreme in this regard: due to their very low rates of star formation, supernova feedback cannot plausibly provide enough energy to drive the observed turbulence *anywhere* within them (Stilp et al., 2013). Nor do magneto-rotational or thermal instability appear to be sufficient (Kim et al., 2003; Piontek & Ostriker, 2004, 2005, 2007). Again, gravitational instability is an obvious candidate to drive the turbulence in the weakly star-forming portions of galaxies.

A final surprising observation concerns the metallicity distributions of galaxies. Observations of disk galaxies show that they have slightly negative gas-phase metallicity gradients inside r_{25} (e.g., Vila-Costas & Edmunds, 1992; Pilyugin et al., 2004; Henry et al., 2010; Balser et al., 2011; Ho et al., 2015), and nearly flat distributions of metallicity outside r_{25} (Bresolin et al., 2009, 2012; Werk et al., 2011). Dwarf galaxies show no metallicity gradients at all (Croxall et al., 2009). While the gradients in inner disks might be explicable simply via a balance between inflow, outflow, and star formation (e.g., see Portinari & Chiosi 2000 and Spitoni & Matteucci 2011 versus Ho et al. 2015), this is not the case for the flat gradients in outer disks. In these strongly gas-dominated regions, the metallicity should simply scale with the stellar mass fraction, regardless of the presence of either inflow or outflow. While the stellar mass fraction changes sharply with galactocentric radius outside r_{25}, the metallicity does not, a finding that seems extremely difficult to explain without invoking some form of metal distribution. As with the previous two results, gravitational instability seems a candidate redistribution

mechanism worthy of further exploration.

1.2 Theoretical Studies of Gravitational Instability

Given the likely importance of gravitational instability as a driver of galaxy evolution, it is not surprising that there have been a number of theoretical studies devoted to it. Some of the earliest were 1D models by Lin & Pringle (1987a,b), Olivier et al. (1991), and Ferguson & Clarke (2001), who argued that the observed exponential distribution of stars in galactic disks could only be understood if gas undergoes significant viscous transport on a timescale comparable to the timescale over which the stellar disk forms. These models assumed a fixed dimensionless viscosity, but Krumholz & Burkert (2010) (generalizing earlier work by Bertin & Lodato (1999) in the context of Keplerian disks with no stars) showed that the viscosity and thus the rates of mass and angular momentum transport could be computed self-consistently by balancing energy loss against turbulence generation by gravitational instability.

Building on this work, (Forbes et al., 2012, 2014a) argue that the observed structure of the star forming disks is a natural result of an equilibrium between gravitational instability and accretion, and star formation. Cosmological accretion brings gas to the disk outskirts, where the gas is in general stable to collapse. Over the course of a few rotation periods, gravitational instability drives torques that tend to move gas to smaller galactocentric radii. The inward flow of gas feeds active ongoing star formation in the inner disk, such that the total star formation in the inner disk is ultimately modulated by the accretion of gas at large galactocentric radii. In these models the

bulk disk is at all times near $Q_{\rm total} \sim 1$. In this paper we are interested in building on these 1D models by directly resolving the process inward mass transport driven by gravitation instability.

Our motivation for 3D simulations is that, while the 1D models are instructive and useful for exploring parameter space quickly, they have substantial limitations. Both the gas and stars both contribute to the self-gravity of the disk, so the degree of gravitational instability of both components must be considered (Lin & Shu, 1966; Jog & Solomon, 1984b,a; Bertin & Romeo, 1988; Wang & Silk, 1994; Romeo & Wiegert, 2011), in the form of the Toomre (1964) stability criterion. This means that an accurate numerical realization of this the gravitational instability process requires detailed modeling of both the gas and stars embedded in a realistic galactic gravitational potential field.

Recently, a new class of high resolution numerical galaxy formation simulations have arisen that begin to probe the density and resolution scales necessary to resolve star forming clouds. These models include varying simplifying assumptions, including an analytic stellar background potential, both with and without imposed spiral arms (Dobbs et al., 2006; Tasker & Tan, 2009; Tasker, 2011; Smith et al., 2014; Dobbs et al., 2015; Tasker et al., 2015). Others resolve the gas to very high spatial resolution at the cost of capturing only a fraction of a galactic dynamical time, or of simulating a galaxy much smaller than the Milky Way (Bournaud et al., 2010; Renaud et al., 2013). Still others take a similar approach to ours (Agertz et al., 2009; Hopkins et al., 2012; Fujimoto et al., 2014b,a), including runs based on the same AGORA (Kim et al., 2014)

initial conditions that we use (Agertz et al., 2015).

1.3 Giant Molecular Clouds

Giant molecular clouds (GMCs) are the primary reservoir of molecular gas in the galaxy (Williams & McKee, 1997; Rosolowsky, 2005; Stark & Lee, 2006). Since the surface density of star formation shows a strong correlation with the surface density of molecular gas (Wong & Blitz, 2002; Kennicutt et al., 2007; Bigiel et al., 2008b; Schruba et al., 2011b), GMCs must also be the primary site of star formation in the Milky Way. However, recent high-resolution observations have shown that the Kennicutt-Schmidt law breaks down when the resolution of an observation is finer than the typical length scales of GMCs (Onodera et al., 2010; Schruba et al., 2010). Thus, in order to develop a detailed theoretical understanding of the relationship between star formation and molecular gas, it is necessary to first understand the formation, evolution, and destruction of giant molecular clouds.

One stumbling block in this effort is the substantial disagreement in the literature regarding both the formation mechanism and typical lifetimes of GMCs (see e.g. Goldreich & Kwan, 1974; Zuckerman & Evans, 1974; Blitz & Shu, 1980; Ballesteros-Paredes et al., 1999; McKee & Ostriker, 2007; Murray, 2011, and references therein). Some authors suggest that GMCs form out of bound atomic gas as a result of gravitational instability (Kim et al., 2002, 2003; Kim & Ostriker, 2006; Li et al., 2006b; Tasker & Tan, 2009), surviving as roughly virialized objects for many cloud dynamical times (Tan et al., 2006; Tamburro et al., 2008). In support of this picture is the observation

that massive clouds are found to be marginally bound, with typical virial parameters of order unity (Heyer et al., 2001; Rosolowsky, 2007; Roman-Duval et al., 2010). Since supersonic isothermal turbulence is found to decay via radiative shocks in one or two crossing times (Mac Low et al., 1998; Stone et al., 1998; Mac Low & Klessen, 2004; Elmegreen & Scalo, 2004), this model must invoke a mechanism to drive supersonic motions for the lifetime of a cloud, which could be several crossing times. Possible turbulent driving mechanisms include protostellar outflows (Norman & Silk, 1980; McKee, 1989; Li & Nakamura, 2006; Li et al., 2010), H II regions (Matzner, 2002; Krumholz & Matzner, 2009, hereafter KM09) , supernovae (Mac Low & Klessen, 2004), or, as investigated here, mass accretion (Klessen & Hennebelle, 2010; Vázquez-Semadeni et al., 2010).

Accretion driven turbulence in molecular clouds has received little attention in the literature. However, as Klessen & Hennebelle (2010) point out, the kinetic energy of accreted material can power the turbulent motions observed in molecular clouds with energy conversion efficiencies of only a few percent. While there has been no systematic study of the kinetic energy budget of a molecular cloud formed via gravitational instability, this problem has been examined in the context of the formation of protogalaxies at high redshift. In one example, Wise & Abel (2007) analyzed simulations of virializing high redshift minihalos, tracking the thermal, kinetic, and gravitational potential energy of gas in protogalactic dark matter halos. In their models, which included a nonequilibrium cooling model, gas collapsed onto the halo and cooled quickly, causing turbulent velocities to become supersonic. As pointed out by Wang & Abel

(2008), this means that the virialization process is a local one: gravitational potential energy can be converted directly into supersonically turbulent motions characterized by a volume-filling network of shocks. The turbulence in turn provides much of the kinetic support for the newly virialized gaseous component of the dark matter halo. If a similar mechanism is at work as gas cools and collapses onto GMCs then gravitational potential energy alone may be sufficient to power turbulence in GMC.

The most detailed simulations of simultaneously accreting and star forming giant molecular clouds were recently completed by Vázquez-Semadeni et al. (2010). These numerical models included a simplified subgrid prescription for stellar feedback by the ionizing radiation of newborn star clusters and focused on the balance between accretion and feedback in clouds formed via thermal instability in colliding flows. Throughout the course of the simulation, dense molecular gas condensed out of a warm atomic envelope, allowing a study of the interplay between accretion and feedback in the simulated clouds. The resulting clouds were able to attain a state of quasi-virial equilibrium, in which the supply of gas from the ambient medium balanced the formation of stars and ejection of gas from H II regions. Due to the idealized nature of the subgrid star formation feedback prescription, in which all H II regions were powered by a cluster with the same ionizing luminosity, star formation feedback was unable to act on the cloud as a whole but could reduce the global star formation rate by destroying overdensities. Since the simulation did not include star clusters with large ionizing luminosities, the cloud as a whole could not be destroyed and star formation would have eventually consumed all of the gas had the simulation not been cut off. Even though the simulations

employed a highly idealized star formation prescription, the computations still required substantial resources to complete and only allowed insight into the evolution of a single cloud. It seems that a computationally inexpensive model that includes a somewhat more sophisticated treatment of star formation feedback is called for.

In this work, we model the global evolution of giant molecular clouds from their birth as low-mass seed clouds to their dispersal after a phase of massive star formation. This is done using an updated version of the semianalytical model of Krumholz et al. (2006). Using a virial formalism, we compute the global dynamical evolution of a single cloud while simultaneously tracking its energy budget. Model clouds form stars, launch H II regions and undergo accretion from their environments. With these models, we are able to investigate the role accretion plays in maintaining turbulence in molecular clouds and directly compare to observations of GMCs in the Milky Way and nearby external galaxies. This work is complementary to the simulations of Vázquez-Semadeni et al. (2010), since our simplified global models allow us to survey a large variety of GMCs at little computational cost while including a much more sophisticated star formation feedback prescription. We are able to capture model clouds with masses comparable to the most massive clouds observed in the Milky Way and nearby galaxies, allowing us to simulate the sites of the majority of star formation in these systems (Williams & McKee, 1997; Fukui & Kawamura, 2010).

Part I

Formation and Evolution of Giant Molecular Clouds

Chapter 2

GMC Models

We proceed by describing the formulation and implementation of our GMC model in section 2.1. Next, in section 2.5, we test our implementation of accretion. Following this, in section 2.6 we perform full simulations and describe the gneral features of our simulated clouds. In section 2.7 we make comparisons to observations, focusing on the scaling relations observed to hold for GMCs as well as the high quality multiwavelength observations available for GMCs in the LMC. Lastly, in section 2.8, we discuss the limitations inherent in the simplifying assumptions we make to derive the cloud evolution equations.

2.1 Governing Equations

The GMC evolution model described below allows us to solve for the time-evolution of the global properties of model molecular clouds. In contrast with previous work, we follow the flow of gas as it condenses out of the diffuse gas in the envelope

surrounding the GMC and falls onto the cloud. Employing simplifying assumptions as well as the results of simulations of compressible MHD turbulence, we derive a set of coupled ordinary differential equations that govern the time evolution of the cloud's mass, radius, and velocity dispersion. Combining the governing evolution equations with a set of initial conditions, model parameters, and a model for the time dependence of the mass accretion rate based on the gravitational collapse of the GMC envelope, we can solve for the time evolution of the cloud. Below, we give an overview of the model, discuss the formulation of our numerical scheme, describe our parameter choices, and give a brief description of our treatment of star formation and our model for the GMCs gas supply.

2.2 Derivation of the Virial Theorem for an accreting cloud

Here we derive an equation governing the virial balance of a cloud that is simultaneously forming stars and accreting material. This is a generalization of the analysis of Krumholz et al. (2006) (hereafter KMM06) and McKee & Zweibel (1992). We refer the reader to those papers for details that are unrelated to the accretion flow and to subsection 2.4.1 for a general overview of the model.

Consider a single molecular cloud contained within an Eulerian volume $V_{\rm vir}$ with bounding surface $S_{\rm vir}$. We assume that $V_{\rm vir}$ is sufficiently large to contain the cloud at all times. Material within the virial volume is apportioned into three components: virial material, a gaseous reservoir, and material in a photoionized wind. Locally, each component satisfies its own continuity equation,

$$\frac{\partial \rho}{\partial t} = -\boldsymbol{\nabla} \cdot \rho \mathbf{v} + \dot{\rho} \tag{2.1}$$

$$\frac{\partial \rho_{\rm res}}{\partial t} = -\boldsymbol{\nabla} \cdot \rho_{\rm res} \mathbf{v}_{\rm res} - \dot{\rho}_{\rm acc} \tag{2.2}$$

$$\frac{\partial \rho_{\rm w}}{\partial t} = -\boldsymbol{\nabla} \cdot \rho_{\rm w} \mathbf{v}_{\rm w} - \dot{\rho}_{\rm ej}. \tag{2.3}$$

These equations are coupled via the source and sink terms,

$$\dot{\rho} = \dot{\rho}_{\rm acc} + \dot{\rho}_{\rm ej}. \tag{2.4}$$

We assume that accretion can only transport material onto the cloud and that the wind can only carry material away from the cloud, implying $\dot{\rho}_{\rm acc} \geq 0$ and $\dot{\rho}_{\rm ej} \leq 0$.

The local equation of momentum conservation for the virial material is (c.f. equation [A2] in KMM06)

$$\frac{\partial}{\partial t}(\rho \mathbf{v}) = -\boldsymbol{\nabla} \cdot (\Pi - \mathbf{T}_{\rm M}) + \rho \mathbf{g} + \mathbf{F}_* + \dot{\rho}_{\rm ej}(\mathbf{v} + \mathbf{v}'_{\rm ej}) + \dot{\rho}_{\rm acc} \mathbf{v}_{\rm res} \tag{2.5}$$

where $\Pi = P_{\rm th}\mathbf{I} + \rho \mathbf{v}\mathbf{v} - \pi$ is the gas pressure tensor, π is the viscous stress tensor, $\mathbf{T}_{\rm M} = [\mathbf{B}\mathbf{B} - (1/2)B^2\mathbf{I}]/(4\pi)$ is the Maxwell stress tensor, $\mathbf{B}$ is the magnetic field, $\mathbf{I}$ is the unit tensor, $\mathbf{g}$ is the gravitational force per unit mass, and $\mathbf{F}_* + \dot{\rho}_{\rm ej}(\mathbf{v} + \mathbf{v}'_{\rm ej})$ is the local body force due to the interaction between expanding H II regions and the cloud. We write the stellar forcing term in this form so as to separate the random component, $\mathbf{F}_*$, from the spherically symmetric component $\dot{\rho}_{\rm ej}(\mathbf{v} + \mathbf{v}'_{\rm ej})$.

$\mathbf{F}_*$ is a function of time and position in the cloud and depends on the precise location and history of massive star formation. Due to the nature of supersonic turbulence, we expect turbulent overdensities to be randomly scattered throughout the cloud. Thus, we expect $\mathbf{F}_*$ to be randomly oriented with respect to the position vector, implying $\int_{V_{\rm vir}} \mathbf{r} \cdot \mathbf{F}_* dV = 0$. While $\mathbf{F}_*$ is randomly oriented, $\dot{\rho}_{\rm ej}(\mathbf{v} + \mathbf{v}'_{\rm ej})$ should on average be purely radial because the photoionized wind will be blown out preferentially along the pressure gradient. Neither $\mathbf{F}_*$ nor the viscous stress tensor is included in the momentum equation used in KMM06. A detailed comparison of the two approaches leads us to conclude that the formulation used here more properly follows the transport of energy through the turbulent cascade.

After taking the second time derivative of the cloud moment of inertia, $I_{\rm cl} = \int_{V_{\rm vir}} \rho r^2 dV$, and substituting the momentum equation (Equation 2.5) into the resulting expression, we find

$$\begin{aligned}\frac{1}{2}\ddot{I}_{\rm cl} = &\frac{1}{2}\frac{d}{dt}\int_{V_{\rm vir}} \dot{\rho} r^2 dV - \frac{1}{2}\frac{d}{dt}\int_{S_{\rm vir}} \rho \mathbf{v} r^2 \cdot d\mathbf{S} \\ &+ \int_{V_{\rm vir}} \mathbf{r} \cdot [\rho \mathbf{g} + \mathbf{F}_* - \boldsymbol{\nabla} \cdot (\Pi - \mathbf{T}_{\rm M})] dV \\ &+ \int_{V_{\rm vir}} \dot{\rho}_{\rm ej} \mathbf{r} \cdot (\mathbf{v} + \mathbf{v}'_{\rm ej}) dV + \int_{V_{\rm vir}} \dot{\rho}_{\rm acc} \mathbf{r} \cdot \mathbf{v}_{\rm res} dV.\end{aligned} \tag{2.6}$$

Upon evaluating the integrals in Equation 2.6 term by term, we obtain the Eulerian Virial Theorem,

$$\begin{aligned}\frac{1}{2}\ddot{I}_{\rm cl} = &2(\mathcal{T} - \mathcal{T}_0) + \mathcal{B} + \mathcal{W} - \frac{1}{2}\frac{d}{dt}\int_{S_{\rm vir}} (\rho \mathbf{v} r^2) \cdot d\mathbf{S} + a_{\rm I} \dot{M}_{\rm cl} R_{\rm cl} \dot{R}_{\rm cl} \\ &+ \frac{1}{2} a_{\rm I} \ddot{M}_{\rm cl} R_{\rm cl}^2 + a_{\rm I} \dot{M}_{\rm ej} R_{\rm cl} \dot{R}_{\rm cl} + \frac{3 - k_\rho}{4 - k_\rho} R_{\rm cl} (\dot{M}_{\rm ej} v'_{\rm ej} - \xi \dot{M}_{\rm acc} v_{\rm esc})\end{aligned} \tag{2.7}$$

Here $\mathcal{T}$, $\mathcal{T}_0$, $\mathcal{B}$, and $\mathcal{W}$ are respectively the standard kinetic, surface kinetic, magnetic, and gravitational terms (see KMM06 for precise definitions) and $a_{\rm I} = (3-k_\rho)/(5-k_\rho)$. The final term in Equation 2.7 does not appear in the EVT derived in KMM06 and is due to the presence of the accretion flow. This has the same form as the wind recoil term except for the presence of a dimensionless factor

$$\xi = \int_0^1 (4-k_\rho) x^{3-k_\rho} \left\{ 1 + f \left[\frac{1-x^{2-k_\rho}}{2-k_\rho} + \int_x^1 \frac{y(x')}{x'^2} dx' \right] \right\} dx \tag{2.8}$$

which arises because material is accreted at a velocity that depends on the depth of the cloud potential well. The dimensionless variables $x, y,$ and f are defined explicitly in section 2.3.

The magnetic term $\mathcal{B}$ retains the form used in KMM06 and derived by (McKee & Zweibel, 1992) because we assume any deformation of the magnetic field in the ambient medium caused by the presence of the cloud is negligible at the virial surface, allowing us to approximate that the virial volume is threaded by a constant magnetic field B_0. Here B_0 is the RMS value of the true magnetic field at the virial surface, which may fluctuate around B_0. Since material in the reservoir should also carry currents and thus generate magnetic fields, this parameterization underestimates the total magnetic energy. However, we expect the mean density of reservoir material within the virial volume to be an order of magnitude smaller than the density of cloud material (see section 2.3), so the contribution of the reservoir to the magnetic energy is small compared to the contribution due to the cloud.

2.3 Properties of the Reservoir

Consider an accreting cloud that is not forming stars and thus not generating a wind. Let $M_{\rm res}(r,t)$ be the mass of material in the accretion flow contained within a radius r at time t and let $\Delta r = v_{\rm res,sys}\Delta t$ be the distance that the accreting gas falls in a time Δt. In the same time, a fraction of the material in the accretion flow will be converted into cloud material. In the frame comoving with the accretion flow, the change in the mass of reservoir interior to a radius r in a time Δt is,

$$M_{\rm res}(r,t) - M_{\rm res}(r-\Delta r, t+\Delta t) = -\Delta t \int_0^r \dot{\rho}_{\rm acc} dV. \tag{2.9}$$

Upon Taylor expanding in Δt and Δr, dropping the nonlinear terms, and evaluating the integral on the right hand side of Equation 2.11, we find,

$$\Delta r \frac{\partial M_{\rm res}(r,t)}{\partial r} - \Delta t \frac{\partial M_{\rm res}(r,t)}{\partial t} = -\dot{M}_{\rm acc}(r,t)\Delta t. \tag{2.10}$$

If the accretion flow is in quasi-steady state, the time derivative vanishes and $M_{\rm res}(r,t) = M_{\rm res}(r)$. Integrating to obtain $M_{\rm res}(r)$, we find

$$M_{\rm res}(r) = -\int_0^r \frac{\dot{M}_{\rm acc}(r')}{v_{\rm res,sys}(r')} dr' \tag{2.11}$$

If we wish to evaluate the above integral and obtain an expression for $M_{\rm res}(r)$, we need to know $v_{\rm res,sys}(r)$. Expanding Equation 2.35, we see

$$\frac{1}{2}v_{\mathrm{res,sys}}^2(r) = \\ -\int_{\infty}^{R_{\mathrm{cl}}} \frac{G(M_{\mathrm{cl}}+M_{\mathrm{res}})}{r'^2}dr' - \int_{R_{\mathrm{cl}}}^{r} \frac{GM_{\mathrm{cl}}(r')}{r'^2}\left[\left(\frac{r'}{R_{\mathrm{cl}}}\right)^{3-k_\rho} + \frac{M_{\mathrm{res}}(r')}{M_{\mathrm{cl}}(r')}\right]dr'. \tag{2.12}$$

Equation 2.11 and Equation 2.12 constitute a system of integral equations that must be simultaneously solved to obtain a solution for the velocity and mass profile of reservoir material within the cloud volume. If we define the functions $x = r/R_{\mathrm{cl}}$, $y(x) = M_{\mathrm{res}}(R_{\mathrm{cl}}x)/M_{\mathrm{cl}}$, and $f = M_{\mathrm{cl}}/(M_{\mathrm{res}}+M_{\mathrm{cl}})$, Equation 2.12 reduces to

$$v_{\mathrm{res,sys}}(r) = -v_{\mathrm{esc}}\left[1 + f\left(\frac{1-x^{2-k_\rho}}{2-k_\rho} - \int_1^x \frac{y(x')}{x'^2}dx'\right)\right]^{1/2}. \tag{2.13}$$

Defining $\zeta = \dot{M}_{\mathrm{acc}}t_{\mathrm{ff}}/M_{\mathrm{cl}}$ and $z(x) = \int_x^1 y(x')/x'^2dx'$, we see that the problem of determining both $v_{\mathrm{res,sys}}(r)$ and $M_{\mathrm{res}}(r)$ reduces to solving the following system of nonlinear ordinary differential equations:

$$\frac{dy}{dx} = \frac{2}{\pi}\zeta x^{3-k_\rho}\left[1 + f\left(\frac{1-x^{2-k_\rho}}{2-k_\rho} + z(x)\right)\right]^{-1/2}, \tag{2.14}$$

$$\frac{dz}{dx} = -\frac{y(x)}{x^2}. \tag{2.15}$$

These equations can be solved numerically using the shooting method as follows. Since there should be no unmixed accreted material at $r = 0$, we expect $y(0) = 0$. Since $z(x)$ is defined in terms of an integral, we have no *a priori* knowledge of $z(0)$. However, we do know that $z(1) = 0$ and we expect $y(1) \leq \zeta$. If we impose $y(1) = c\zeta$

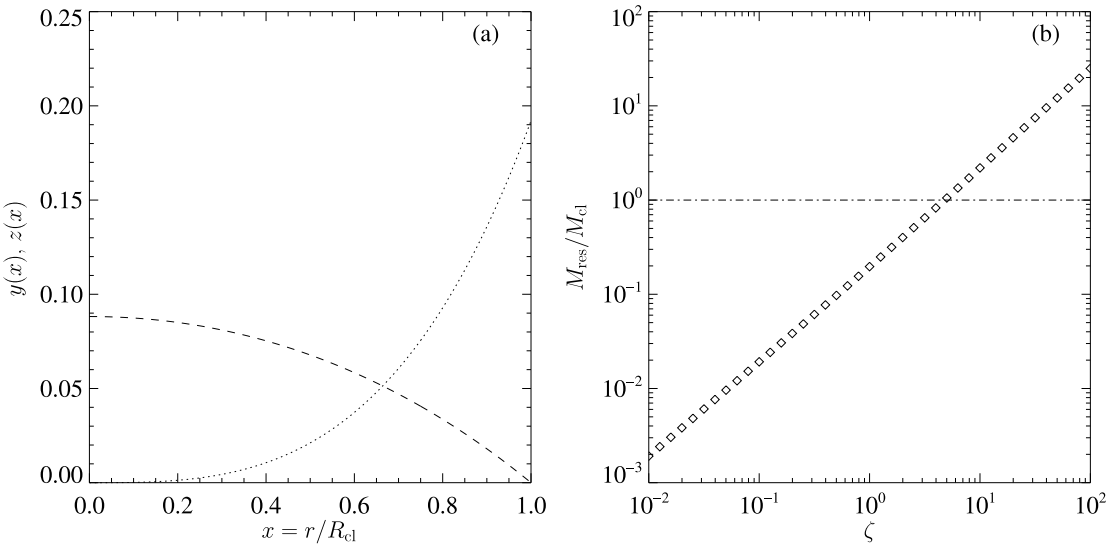

Figure 2.1: (a): y (dotted line) and z (dashed line) as a function of $x = r/R_{\rm cl}$. (b): $y(1) = M_{\rm res}(R_{\rm cl})/M_{\rm cl}$ as a function of $\zeta = \dot{M}_{\rm acc} t_{\rm ff}/M_{\rm cl}$. We see $M_{\rm res}(R_{\rm cl}) \geq M_{\rm cl}$ for $\zeta \gtrsim 5$.

where c is a constant of order unity, we can integrate the above system and obtain a trial solution for $y(x)$ and $z(x)$. The constant c can then be varied until a solution is obtained with $y(0) = 0$. There is a unique solution for each value of ζ and thus a new solution must be obtained if ζ varies.

A key assumption in this analysis was that the accretion rate is approximately constant over the cloud free-fall timescale. This is equivalent to the assumption that $\zeta \lesssim 1$. This is a reasonable assumption, which we can see by making an analogy to the case of a protostellar core. Since we expect $\dot{M}_{\rm cl} \approx M_{\rm cl}/t_{\rm ff,r}$ where $t_{\rm ff,r}$ is the free-fall time for all of the gas in the reservoir (Stahler et al., 1980; McKee & Tan, 2003) and since the reservoir should be significantly more extended than the cloud, we expect the mean density of the reservoir to be much lower than the mean density in the cloud. This implies $t_{\rm ff,r} \gg t_{\rm ff,cl}$. If this condition does hold, then the condition $\zeta \leq 1$ is automatically

satisfied.

In Figure 2.1a we present a numerical solution for $y(x)$ and $z(x)$ obtained for $\zeta = 1.0$. We see for this case that $M_{\rm res}(R_{\rm cl}) \approx 0.2 M_{\rm cl}$, showing that even for substantial accretion rates, the gas within $V_{\rm cl}$ is primarily composed of cloud material. In Figure 2.1b we show $y(1) = M_{\rm res}(R_{\rm cl})/M_{\rm cl}$ as a function of ζ. Reservoir material becomes the primary component of the volume occupied by the cloud for $\zeta \gtrsim 5.0$. For this reason, we reject as unphysical any portion of cloud history with $\zeta \geq 5$. In practice, we find $\zeta \lesssim 1.0$ for the lifetime of all clouds we simulate.

2.4 Derivation of the Equation of Energy Conservation for an Accreting Cloud

Here we derive the global equation of energy conservation for a cloud undergoing accretion and star formation. We begin by writing the equation of momentum conservation (Equation 2.5) in Lagrangian form,

$$\rho \frac{d\mathbf{v}}{dt} = -\boldsymbol{\nabla} P - \rho \boldsymbol{\nabla} \phi + \boldsymbol{\nabla} \cdot \pi + \frac{\mathbf{J} \times \mathbf{B}}{c} + \dot{\rho}_{\rm ej} \mathbf{v}'_{\rm ej} + \mathbf{F}_* + \dot{\rho}_{\rm acc} (\mathbf{v}_{\rm res} - \mathbf{v}). \tag{2.16}$$

Upon contracting the above equation with $\mathbf{v}$, we obtain the nonthermal energy evolution equation,

$$\frac{\partial}{\partial t}\left(\frac{1}{2}\rho v^2 + \rho\phi_{\rm cl} + \frac{B^2 - B_0^2}{8\pi}\right) + \boldsymbol{\nabla}\cdot\rho\mathbf{v}\left(\frac{1}{2}v^2 + \phi_{\rm cl}\right) + \boldsymbol{\nabla}\cdot\mathbf{S}_{\rm P} =$$
$$-\mathbf{v}\cdot\boldsymbol{\nabla}P + \rho\frac{\partial\phi_{\rm cl}}{\partial t} + \rho\mathbf{v}\cdot\mathbf{g}_{\rm res} + \boldsymbol{\nabla}\cdot(\pi\cdot\mathbf{v}) - \pi : \boldsymbol{\nabla}\mathbf{v} + \dot{\rho}\left(\frac{1}{2}v^2 + \phi_{\rm cl}\right) \tag{2.17}$$
$$+\mathbf{v}\cdot\mathbf{F}_* + \dot{\rho}_{\rm ej}\mathbf{v}\cdot\mathbf{v}'_{\rm ej} + \dot{\rho}_{\rm acc}(\mathbf{v}\cdot\mathbf{v}_{\rm res} - v^2)$$

where $\mathbf{S}_{\rm P}$ is the Poynting vector. Combining the first law of thermodynamics with the continuity equation yields the evolution equation for the thermal energy of the cloud,

$$\frac{\partial}{\partial t}(\rho e) + \boldsymbol{\nabla}\cdot\rho\mathbf{v}\left(e + \frac{P}{\rho}\right) = \dot{\rho}e + \mathbf{v}\cdot\boldsymbol{\nabla}P + \Gamma - \Lambda \tag{2.18}$$

where e is the internal energy per unit mass and Γ and Λ are respectively the rates of energy gain and loss per unit volume. Here we've assumed that accreted material has the same thermal energy density as cloud material, which will be true if the radiative timescales are short compared to the mechanical timescales, as in molecular cloud conditions. Summing Equation 2.17 and Equation 2.18, we obtain the evolution equation for the total energy of the system

$$\frac{\partial}{\partial t}\left[\rho\left(\frac{1}{2}v^2 + e + \frac{1}{2}\phi_{\rm cl}\right) + \frac{B^2 - B_0^2}{8\pi}\right] + \boldsymbol{\nabla}\cdot\rho\mathbf{v}\left(\frac{1}{2}v^2 + e + \frac{P}{\rho} + \phi_{\rm cl}\right)$$
$$+\boldsymbol{\nabla}\cdot\mathbf{S}_{\rm P} = \frac{1}{2}\left(\rho\frac{\partial\phi_{\rm cl}}{\partial t} - \frac{\partial\rho}{\partial t}\phi_{\rm cl}\right) + \dot{\rho}\left(\frac{1}{2}v^2 + e + \frac{1}{2}\phi_{\rm cl}\right) + \frac{1}{2}\dot{\rho}\phi_{\rm cl} + \rho\mathbf{v}\cdot\mathbf{g}_{\rm res} \tag{2.19}$$
$$+\dot{\rho}_{\rm ej}\mathbf{v}\cdot\mathbf{v}'_{\rm ej} + \dot{\rho}_{\rm acc}(\mathbf{v}\cdot\mathbf{v}_{\rm res} - v^2) + \boldsymbol{\nabla}\cdot(\pi\cdot\mathbf{v}) + \mathbf{v}\cdot\mathbf{F}_* - \Lambda.$$

Here we've assumed that $\Gamma = \pi : \boldsymbol{\nabla}\mathbf{v}$, the scalar rate of viscous dissipation. This

is equivalent to the statement that turbulent kinetic energy is converted into heat at viscous scales whereupon the energy is quickly radiated away. While there may be other heating mechanisms, including cosmic rays and protostellar radiation, we neglect these sources by noting that any local heating should be offset in a time much shorter than the dynamical time.

If we define the total energy due to the presence of the cloud,

$$\mathcal{E}_{\rm cl} = \int_{V_{\rm cl}} \rho \left(\frac{1}{2} v^2 + e + \frac{1}{2}\phi_{\rm cl} \right) dV + \int_{V_{\rm vir}} \frac{B^2 - B_0^2}{8\pi} dV \tag{2.20}$$

and the total energy in the ambient medium,

$$\mathcal{E}_{\rm amb} = \int_{V_{\rm vir} - V_{\rm cl}} \rho \left(\frac{1}{2} v^2 + e + \frac{1}{2}\phi_{\rm cl} \right) dV, \tag{2.21}$$

we can integrate Equation 2.19 over the virial volume and obtain an evolution equation for $\mathcal{E}_{\rm cl}$. Portions of this calculation are performed explicitly in KMM06 and we do not reproduce those results here. The new terms stem from our inclusion of accretion as well as the inclusion of $\mathbf{F}_*$, the random component of the stellar forcing term. The integrals over the new terms are evaluated below.

The first new term is due to the gravitational influence of the reservoir,

$$\int_{V_{\rm vir}} \rho \mathbf{v} \cdot \mathbf{g}_{\rm res} dV = -\chi \frac{\dot{R}_{\rm cl}}{R_{\rm cl}} \frac{G M_{\rm cl}^2}{R_{\rm cl}} \tag{2.22}$$

where

$$\chi = (3 - k_\rho) \int_0^1 x^{1-k_\rho} y(x) dx. \tag{2.23}$$

This is the gravitational work done on the cloud by the reservoir material as the cloud expands and contracts.

The random stellar forcing term can be evaluated by noting that $\mathbf{r}$ and $\mathbf{F}_*$ are assumed to be uncorrelated, so $\int_{V_{\rm vir}} \mathbf{v} \cdot \mathbf{F}_* dV = \int_{V_{\rm vir}} \mathbf{v}_{\rm turb} \cdot \mathbf{F}_* dV$. This integral depends on the degree of correlation between two randomly oriented vectors, $\mathbf{v}_{\rm turb}$ and $\mathbf{F}_*$. Since, at a fixed time, the direction of expansion of an H II region is the same as the direction of momentum injection, these vectors should indeed be highly correlated. This term then corresponds to the net injection of energy by H II regions,

$$\mathcal{G}_{\rm cl} = \int_{V_{\rm vir}} \mathbf{v}_{\rm turb} \cdot \mathbf{F}_* dV. \tag{2.24}$$

For the terms proportional to $\dot{\rho}_{\rm acc}$, we have

$$\int_{V_{\rm vir}} \dot{\rho}_{\rm acc} \mathbf{v} \cdot \mathbf{v}_{\rm res} dV = -\left(\frac{3 - k_\rho}{4 - k_\rho}\right) \xi \dot{R}_{\rm cl} \dot{M}_{\rm acc} v_{\rm esc} + \int_{V_{\rm vir}} \dot{\rho}_{\rm acc} \mathbf{v}_{\rm turb} \cdot \mathbf{v}_{\rm res} dV \tag{2.25}$$

and

$$\int_{V_{\rm vir}} \dot{\rho}_{\rm acc} v^2 dV = a_{\rm I} \dot{M}_{\rm acc} \dot{R}_{cl}^2 + 3 \dot{M}_{\rm acc} \sigma_{\rm cl}^2 \tag{2.26}$$

where we've used our assumption that $\mathbf{v}_{\rm res,rand}$ is randomly oriented with respect to $\mathbf{r}$.

We are left with one last integral on the right hand side of Equation 2.25 that depends on the correlation between two vector fields, $\mathbf{v}_{\rm turb}$ and $\mathbf{v}_{\rm res}$. Suppose $\mathbf{v}_{\rm res}$ and $\mathbf{v}_{\rm turb}$ are perfectly correlated. In that case, the integral we are concerned with can be readily evaluated in three limits, $|\mathbf{v}_{\rm res}| = |\mathbf{v}_{\rm turb}|$, $|\mathbf{v}_{\rm res}| \gg |\mathbf{v}_{\rm turb}|$, and $|\mathbf{v}_{\rm res}| \ll |\mathbf{v}_{\rm turb}|$. In the first limit $|\mathbf{v}_{\rm res}| = |\mathbf{v}_{\rm turb}|$ the transfer of material to the cloud is merely an act of relabeling, so $\mathbf{v}_{\rm turb} \cdot \mathbf{v}_{\rm res} = \mathbf{v}_{\rm res}^2$. Now consider the limit $|\mathbf{v}_{\rm res}| \gg |\mathbf{v}_{\rm turb}|$. We approximate that a parcel of reservoir material mixes with the cloud once it has swept up a mass of cloud material equal to its own mass. Since the interaction between cloud material and reservoir material must be inelastic if they are to mix, the velocity of cloud material must be driven by the act of mixing to $\mathbf{v}_{\rm turb} = \mathbf{v}_{\rm res}/2$. Conversely, if $|\mathbf{v}_{\rm res}| \ll |\mathbf{v}_{\rm turb}|$, the reservoir material is driven to a velocity $\mathbf{v}_{\rm res} = \mathbf{v}_{\rm turb}/2$. We obtain the correct answer in all three limits if we assume

$$\int_{V_{\rm vir}} \dot{\rho}_{acc} \mathbf{v}_{\rm turb} \cdot \mathbf{v}_{\rm res} dV = \frac{1}{2} \int_{V_{\rm vir}} \dot{\rho}_{acc} (\mathbf{v}_{\rm res}^2 + \mathbf{v}_{\rm turb}^2) dV. \tag{2.27}$$

This is an upper bound on the value of the integral in the limit of perfect correlation between $\mathbf{v}_{\rm turb}$ and $\mathbf{v}_{\rm res}$. If $\mathbf{v}_{\rm turb}$ and $\mathbf{v}_{\rm res}$ are uncorrelated then the integrand should on average be zero. Thus we have,

$$0 \leq \int_{V_{\rm vir}} \dot{\rho}_{acc} \mathbf{v}_{\rm turb} \cdot \mathbf{v}_{\rm res} dV \leq \frac{1}{2} \int_{V_{\rm vir}} \dot{\rho}_{acc} (\mathbf{v}_{\rm res}^2 + \mathbf{v}_{\rm turb}^2) dV. \tag{2.28}$$

To evaluate this integral, we linearly interpolate between the upper limit and lower

limit,

$$\begin{aligned}
&\int_{V_{\rm vir}} \dot{\rho}_{acc}\mathbf{v}_{\rm turb}\cdot\mathbf{v}_{\rm res}dV \\
&= \varphi\frac{1}{2}\int_{V_{\rm vir}} \dot{\rho}_{acc}(\mathbf{v}_{\rm res}^2+\mathbf{v}_{\rm turb}^2)dV \\
&= \varphi(\frac{3}{2}\dot{M}_{\rm acc}\sigma_{\rm res}^2+\frac{3}{2}\dot{M}_{\rm acc}\sigma_{\rm cl}^2+\gamma\dot{M}_{\rm acc}v_{\rm esc}^2)
\end{aligned} \tag{2.29}$$

where φ is an interpolation parameter that ranges between zero and unity and

$$\gamma = \frac{1}{2}+f\left(\frac{1}{10-4k_\rho}-\frac{\chi}{6-2k_\rho}\right). \tag{2.30}$$

Summing the individual terms derived above yields the global form of the equation of energy conservation,

$$\begin{aligned}
\frac{d\mathcal{E}_{\rm cl}}{dt} &= \frac{\dot{M}_{\rm cl}}{M_{\rm cl}}[\mathcal{E}_{\rm cl}+(1-\eta_B^2)\mathcal{W}]+\frac{GM_{\rm cl}\dot{M}_{\rm cl}}{R_{\rm cl}}\chi\left(1-\frac{M_{\rm cl}\dot{R}_{\rm cl}}{\dot{M}_{\rm cl}R_{\rm cl}}\right) \\
&+\left(\frac{3-k_\rho}{4-k_\rho}\right)\dot{R}_{\rm cl}(\dot{M}_{\rm ej}v_{\rm ej}^{'}-\xi\dot{M}_{\rm acc}v_{\rm esc})-4\pi P_{\rm amb}R_{\rm cl}^2\dot{R}_{\rm cl} \\
&-a_{\rm I}\dot{M}_{\rm acc}\dot{R}_{\rm cl}^2-3\dot{M}_{\rm acc}\sigma_{cl}^2+\varphi(\frac{3}{2}\dot{M}_{\rm acc}\sigma_{\rm res}^2+\frac{3}{2}\dot{M}_{\rm acc}\sigma_{\rm cl}^2+\gamma\dot{M}_{\rm acc}v_{\rm esc}^2) \\
&+\mathcal{G}_{\rm cl}-\mathcal{L}_{\rm cl}
\end{aligned} \tag{2.31}$$

where $\mathcal{L}_{\rm cl}=\int_{V_{\rm vir}}\Lambda dV$.

2.4.1 Model Overview

The model we employ below is based on the global GMC model of KMM06, itself a generalization of the the global model for low mass star formation of McKee (1989), the Eulerian virial theorem (EVT) of McKee & Zweibel (1992), and the model

for star forming clumps of Matzner (2001). Employing a virial formalism, we account for the dynamics and energy budget of gas contained within an Eulerian volume, $V_{\rm vir}$. We separate the gas within $V_{\rm vir}$ into three species: virial material, a gaseous reservoir, and a photoionized wind. A schematic representation of the components of our model is presented in Figure 2.2.

By design, each of the three components has a straightforward physical interpretation. The first component, which we label virial material, consists of two physically distinct subcomponents: a molecular cloud and a warm atomic envelope that encloses the cloud. The cloud is assumed to be cold ($\sim$ 10K), molecular, and contained within a spherical volume of radius $R_{\rm cl}$. The ambient medium is composed of warm ($\sim 10^3$K) and diffuse atomic gas that encloses the cloud and extends beyond the virial volume. The second component is a gaseous reservoir, which we assume is composed of cold ($\sim 10^2$K) neutral material that flows onto the cloud at free-fall from beyond the virial volume. The last component is an ionized wind made up of hot ($\sim 10^4$K) ionized gas ejected from the ionization fronts of blister-type H II regions. All three components are allowed to mutually interpenetrate. We restrict interaction between the components to the transfer of mass between the accretion flow and cloud as well as between the cloud and wind. Since the envelope and cloud are not allowed to interpenetrate, we formally group the envelope and cloud together; this somewhat artificial choice significantly simplifies the virial analysis.

We make use of two simplifying assumptions regarding the distribution and flow of the virial material. First, we assume that the virial material follows a spherically

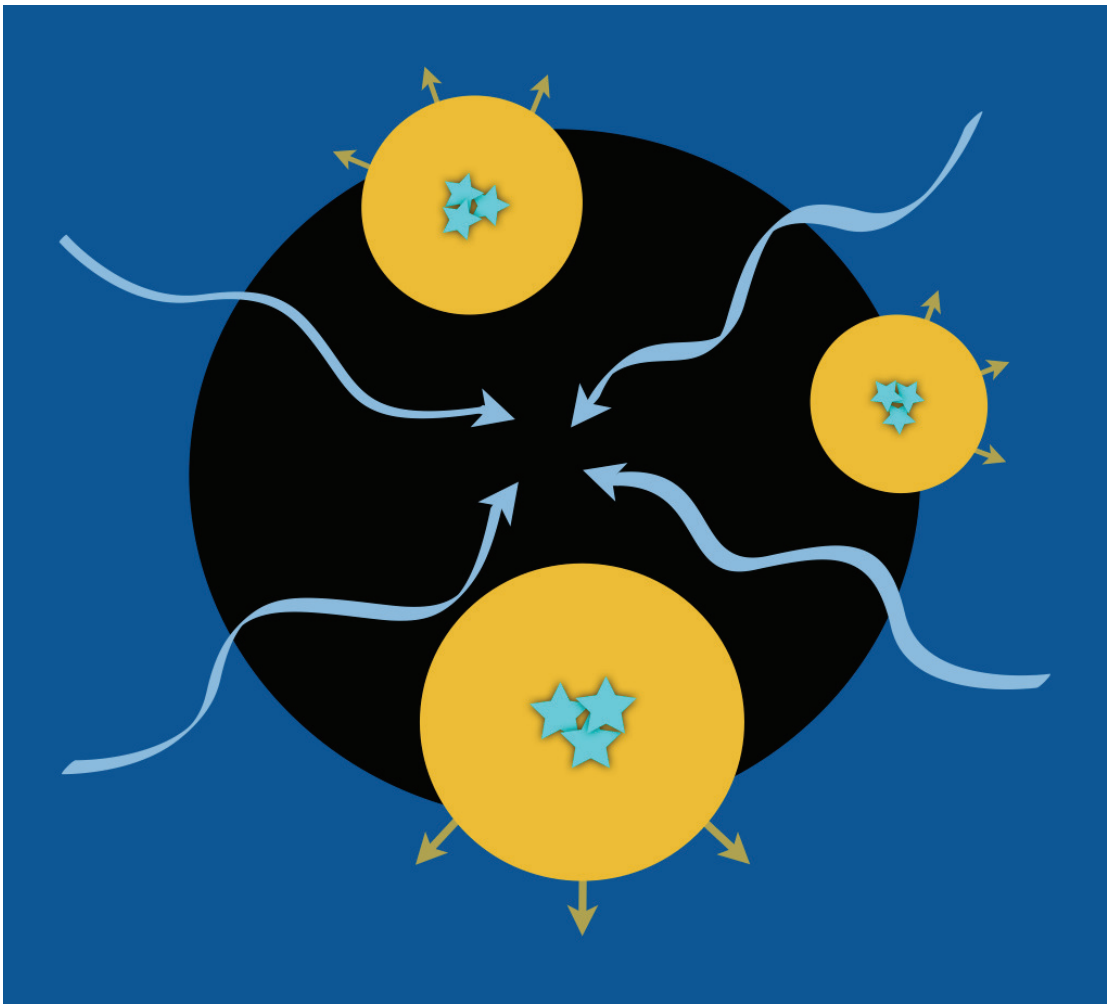

Figure 2.2: A schematic overview of the GMC model. A molecular cloud (*black*) is embedded in a warm atomic envelope (*dark blue*). Cool atomic gas (*light blue*) flows onto the cloud, where it condenses, recombines into molecules, and mixes with the cloud. Newborn OB associations (*blue stars*) drive H II regions (*orange*) and eject winds ionized winds back into the ambient medium.

symmetric, smoothly varying density profile. Second, we assume that the the cloud is homologous: the cloud expands, contracts, accretes, and sheds mass in such a way as to always maintain the same smooth density profile. We assume a density profile of the form

$$\rho(r) = \rho_0 \left(\frac{r}{R_{\rm cl}} \right)^{-k_\rho} \quad \text{for } r \leq R_{\rm cl} \tag{2.32}$$

where ρ_0 is the density at the edge of the cloud and k_ρ is assumed to be unity. This choice is consistent with the Larson scaling relations observed in galactic (Larson, 1981; Solomon et al., 1987; Heyer et al., 2001, 2009) and extragalactic (Mizuno et al., 2001; Engargiola et al., 2003; Rosolowsky, 2007; Bolatto et al., 2008; Hughes et al., 2010) GMCs. Our assumed cloud density profile effectively averages over clumpy and filamentary internal structure and oblate shapes of observed clouds. At $r = R_{\rm cl}$, the density of the ambient medium is assumed to smoothly transition from ρ_0 to $\rho_{\rm amb}$ in a thin boundary layer. We assume that the density of the ambient medium is negligible compared to the density of gas in the cloud, $\rho_{\rm amb} \ll \rho_0$. The density of the ambient medium remains $\rho_{\rm amb}$ out to the virial radius.

Beyond assuming a density profile, we must also specify the velocity structure of all three components of the model. We follow KMM06 in assuming that the velocity of the virial material can be decomposed into a systematic and turbulent component,

$$\mathbf{v} = \frac{\dot{R}_{\rm cl}}{R_{\rm cl}} \mathbf{r} + \mathbf{v}_{\rm turb}. \tag{2.33}$$

We assume that $\mathbf{v}_{\rm turb}$ is randomly oriented with respect to position so that turbulent

motions carry no net flux of matter. We make a similar assumption regarding the velocity structure of the reservoir,

$$\mathbf{v}_{\rm res} = v_{\rm res,sys}\hat{r} + \mathbf{v}_{\rm res,turb}. \tag{2.34}$$

The systematic component of $\mathbf{v}_{\rm res}$ is due to the gravitational attraction of material within the virial volume

$$\frac{v^2_{\rm res,sys}}{2} = \int_{\infty}^{r} \mathbf{g}\cdot d\mathbf{r}, \tag{2.35}$$

while the random component is such that $(M_{\rm cl}^{-1}\int_{V_{\rm cl}}\rho\mathbf{v}^2_{\rm res,turb}dV)^{1/2} = \sqrt{3}\sigma_{\rm res}$. Here $\mathbf{g}$ is the gravitational acceleration and $\sigma_{\rm res}$ is the velocity dispersion of gas in the reservoir feeding the accretion flow. Since the amount of material in the accretion flow is determined by how fast it can fall into the cloud, we must simultaneously determine both the density profile and radial velocity of material in the accretion flow (see section 2.3). Finally, for the wind material, we follow KMM06 in assuming

$$\mathbf{v}_{\rm w} = \mathbf{v} + \mathbf{v}'_{\rm ej} \tag{2.36}$$

where $\mathbf{v}'_{\rm ej} = 2c_{\rm II}\hat{r}$ and $c_{\rm II}$ is the ionized gas sound speed. We follow McKee & Williams (1997) in choosing $c_{\rm II} = 9.7{\rm kms}^{-1}$.

2.4.2 Momentum Equation

In section 2.2, we derive the EVT for a simultaneously evaporating and accreting cloud,

$$\begin{aligned}\frac{1}{2}\ddot{I}_{\rm cl} = 2(\mathcal{T}-\mathcal{T}_0)+\mathcal{B}+\mathcal{W}-\frac{1}{2}\frac{d}{dt}\int_{S_{\rm vir}}(\rho\mathbf{v}r^2)\cdot d\mathbf{S} \\ + a_{\rm I}\dot{M}_{\rm cl}R_{\rm cl}\dot{R}_{\rm cl}+\frac{1}{2}a_{\rm I}\ddot{M}_{\rm cl}R_{\rm cl}^2+a_{\rm I}\dot{M}_{\rm ej}R_{\rm cl}\dot{R}_{\rm cl} \\ + \frac{3-k_\rho}{4-k_\rho}R_{\rm cl}(\dot{M}_{\rm ej}v'_{\rm ej}-\xi\dot{M}_{\rm acc}v_{\rm esc})\end{aligned} \tag{2.37}$$

Here, $a_{\rm I}$ is a constant of order unity that depends on the distribution of material in the cloud, $I_{\rm cl}$ is the cloud moment of inertia, $\mathcal{T}$ is the combined turbulent and thermal kinetic energy of the cloud, $\mathcal{T}_0$ is the energy associated with interstellar pressure at the cloud surface, $\mathcal{B}$ is the net magnetic energy due to the presence of the cloud, $\mathcal{W}$ is the gravitational term (equal to the gravitational binding energy in the absence of an external potential [McKee & Zweibel 1992]), the surface integral is proportional to the rate of change of the moment of inertia inside the bounding viral surface, $M_{\rm cl}$ is the cloud mass, $R_{\rm cl}$ is the cloud radius, $\dot{M}_{\rm ej}$ is the mass ejection rate, $\dot{M}_{\rm acc}$ is the mass accretion rate, $v_{\rm esc}=\{2G[M_{\rm cl}+M_{\rm res}(R_{\rm cl})]/R_{\rm cl}\}^{1/2}$ is the escape velocity at the edge of the cloud, and ξ is a dimensionless factor we compute via Equation 2.8 that depends on the depth of the cloud potential well. The quantity $\xi v_{\rm esc}$ is the accretion rate weighted average infall velocity. Precise definitions for $\mathcal{T}$, $\mathcal{T}_0$, $\mathcal{B}$, and $\mathcal{W}$ are given in KMM06.

The EVT of a cloud without accretion or mass loss would only contain the terms up to the surface integral. The next three terms account for changes in the cloud moment of inertia due to changes in the mass of the cloud, while the last term accounts

for the rate at which the recoil of inflowing and outflowing mass injects momentum into the cloud. Inflows and outflows are treated separately because material is ejected at a constant velocity, but is accreted at a velocity that is a function of the depth of the potential well of the cloud. The dimensionless factor ξ appears due to this difference.

The mass of the cloud can only change via mass accretion or ejection,

$$\dot{M}_{\rm cl} = \dot{M}_{\rm ej} + \dot{M}_{\rm acc}. \tag{2.38}$$

We assume that ejection of material can only decrease the mass of the cloud and accretion can only increase the mass of the cloud. Since stars may not follow the homologous density profile we assume, we neglect the change in the cloud mass due to star formation. We expect the error incurred from this assumption will be small, since stars make up a small fraction of the mass of observed clouds (Evans et al., 2009; Lada et al., 2010) and our assumed star formation law converts a small fraction of the cloud's mass into stars per free-fall time.

We follow KMM06 in using the assumption of homology and the results of simulations of MHD turbulence to evaluate each term in the EVT in terms of constants and the dynamical variables $R_{\rm cl}$, $M_{\rm cl}$, and $\sigma_{\rm cl}$. In the end, we obtain a second order

nonlinear ordinary differential equation in $R_{\rm cl}$,

$$\begin{aligned} a_I \ddot{R}_{\rm cl} = & 3\frac{c_{\rm cl}^2}{R_{\rm cl}} + 3.9\frac{\sigma_{\rm cl}^2}{R_{\rm cl}} - \frac{3}{5}a'(1-\eta_B^2)\frac{GM_{\rm cl}}{R_{\rm cl}^2} \\ & - 4\pi P_{\rm amb}\frac{R_{\rm cl}^2}{M_{\rm cl}} - a_I\frac{\dot{M}_{\rm acc}}{M_{\rm cl}}\dot{R}_{\rm cl} \\ & + \left(\frac{3-k_\rho}{4-k_\rho}\right)\left(\frac{\dot{M}_{\rm ej}}{M_{\rm cl}}v'_{\rm ej} - \xi\frac{\dot{M}_{\rm acc}}{M_{\rm cl}}v_{\rm esc}\right). \end{aligned} \tag{2.39}$$

Here,

$$a' = \frac{15-5k_\rho}{15-6k_\rho}\left[1 + (3-2k_\rho)\int_0^1 x^{1-k_\rho}y(x)dx\right], \tag{2.40}$$

$y(x)$ is the ratio of the mass of reservoir material to the mass of cloud material contained within a normalized radius $x = r/R_{\rm cl}$ (see section 2.3), and $\eta_{\rm B}$ is the ratio of the magnetic critical mass to the cloud mass.

This equation governs the balance of forces acting on the cloud as a whole. Each term corresponds to a single physical mechanism that can alter the radial force balance. The first two terms are due to thermal and turbulent pressure support, respectively. The third is due to a combination of gravitational compression and magnetic support. The fourth is due to the confining interstellar pressure. The fifth comes from the exchange of momentum between the expanding cloud and infalling accretion flow. Finally, the last term is due to a combination of the recoil from ejected material and the ram pressure of accreting material. Although the two parts of the recoil term have opposite signs, $\dot{M}_{\rm ej}$ and $\dot{M}_{\rm acc}$ have opposite signs as well: $\dot{M}_{\rm ej} < 0$ and $\dot{M}_{\rm acc} > 0$. This implies that both the recoil due to launching wind material and the ram pressure of accreting reservoir material tend to confine the cloud.

Letting $M_{\rm cl,0}$, $R_{\rm cl,0}$, and $\sigma_{\rm cl,0}$ be the cloud mass, radius, and velocity dispersion at $t = 0$ and defining the initial cloud crossing time, $t_{\rm cr,0} = R_{\rm cl,0}/\sigma_{\rm cl,0}$, we can define the dimensionless variables $M = M_{\rm cl}/M_{\rm cl,0}$, $R = R_{\rm cl}/R_{\rm cl,0}$, $\sigma = \sigma_{\rm cl}/\sigma_{\rm cl,0}$, and $\tau = t/t_{\rm cr,0}$. Letting primes denote differentiation with respect to τ, we can write Equation 2.39 in dimensionless form

$$\begin{aligned} R'' =& \frac{3.9\sigma^2 + 3\mathcal{M}_0^{-2}}{a_I R} - \eta_G \frac{a' M}{R^2} - \eta_P \frac{R^2}{M} \\ & - \frac{M'_{\rm acc} R'}{M} + \eta_E \frac{M'_{\rm ej}}{M} - \eta_A \frac{\xi M'_{\rm acc}}{(fMR)^{1/2}} \end{aligned} \tag{2.41}$$

where

$$\mathcal{M}_0 = \sigma_{\rm cl,0}/c_{\rm cl} \tag{2.42}$$

is the initial turbulent Mach number and we define the dimensionless constants

$$\eta_G = \frac{3(1-\eta_B^2)}{a_I \alpha_{\rm vir,0}} \tag{2.43}$$

$$\eta_P = \frac{4\pi R_{\rm cl,0}^3 P_{\rm amb}}{a_I M_{\rm cl,0} \sigma_{\rm cl,0}^2} \tag{2.44}$$

$$\eta_E = \left(\frac{5-k_\rho}{4-k_\rho}\right) \frac{v'_{\rm ej}}{\sigma_{\rm cl,0}} \tag{2.45}$$

$$\eta_A = \left(\frac{5-k_\rho}{4-k_\rho}\right) \left(\frac{10}{\alpha_{\rm vir,0}}\right)^{1/2} \tag{2.46}$$

where

$$\alpha_{\rm vir,0} = \frac{5\sigma_{\rm cl,0}^2 R_{\rm cl,0}}{G M_{\rm cl,0}} \tag{2.47}$$

is the initial nonthermal virial parameter (Bertoldi & McKee, 1992). These constants are set by the ratios of various forces acting on the initial state of the cloud. $\eta_{\rm G}$ is

proportional to the ratio of the initial magnetic forces to the initial gravitational force, and η_P, η_E, and η_A are the ratios of the ambient pressure force, the mass ejection recoil force, and the initial accretion ram pressure force to the initial internal turbulent forces, respectively.

Comparing Equation 2.41 with the corresponding equation given in KMM06, we see that two new terms proportional to $M'_{\rm acc}$ have appeared. In practice, we find that, of the two terms, the one proportional to η_A dominates, implying that the primary direct impact of accretion on the radial force balance of the cloud is to provide a confining ram pressure. We will see in the next section that accretion also increases the turbulent velocity dispersion, implying that the kinetic pressure term also increases when accretion is included. The cloud radius is determined by a balance between kinetic pressure and a combination of gravity, accretion ram pressure, and wind recoil pressure. Thermal pressure support is negligible.

We also note that although the ambient pressure term is of the same form as in KMM06, we assume an observationally motivated value for the ambient pressure, $P_{\rm amb}/k_{\rm B} = 3\times10^4{\rm Kcm}^{-3}$ (McKee, 1999). This includes thermal and turbulent pressure but neglects magnetic and cosmic ray pressure, since magnetic fields and cosmic rays permeate both the cloud and the ambient ISM. We have also adjusted the ambient pressure upwards by a factor of two because GMCs form in overdense regions of the ISM where the hydrostatic pressure is higher than average. In KMM06, $P_{\rm amb}$ was chosen to be artificially high to ensure that the cloud would start its evolution in hydrostatic equilibrium. This choice was made to account for the weight of the gaseous reservoir

that was not explicitly included. In practice, by choosing a lower value for $P_{\rm amb}$, we find that the ambient pressure term is subdominant for most of the evolution of the cloud. This is expected, since we now correctly account for the pressure of the reservoir through the term proportional to $\eta_{\rm A}$. Once accretion halts, the cloud is left out of pressure equilibrium and must expand to match the ambient pressure. This effect is seen most clearly in the second column of Figure 2.4.

2.4.3 Energy Equation

In section 2.4, we derive the time evolution equation for the total energy of the cloud,

$$\begin{aligned}
\frac{d\mathcal{E}_{\rm cl}}{dt} &= \frac{\dot{M}_{\rm cl}}{M_{\rm cl}}[\mathcal{E}_{\rm cl} + (1-\eta_B^2)\mathcal{W}] - 4\pi P_{\rm amb} R_{\rm cl}^2 \dot{R}_{\rm cl} \\
&+ \frac{G M_{\rm cl}\dot{M}_{\rm cl}}{R_{\rm cl}}\chi\left(1 - \frac{M_{\rm cl}\dot{R}_{\rm cl}}{\dot{M}_{\rm cl}R_{\rm cl}}\right) \\
&+ \left(\frac{3-k_\rho}{4-k_\rho}\right)\dot{R}_{\rm cl}(\dot{M}_{\rm ej}v'_{\rm ej} - \xi\dot{M}_{\rm acc}v_{\rm esc}) \\
&+ \varphi(\frac{3}{2}\dot{M}_{\rm acc}\sigma_{\rm res}^2 + \frac{3}{2}\dot{M}_{\rm acc}\sigma_{\rm cl}^2 + \gamma\dot{M}_{\rm acc}v_{\rm esc}^2) \\
&- a_I\dot{M}_{\rm acc}\dot{R}_{\rm cl}^2 - 3\dot{M}_{\rm acc}\sigma_{cl}^2 + \mathcal{G}_{\rm cl} - \mathcal{L}_{\rm cl},
\end{aligned} \tag{2.48}$$

where $\mathcal{G}_{\rm cl}$ and $\mathcal{L}_{\rm cl}$ are the rates of energy gain and loss due to H II regions and turbulent dissipation, respectively, $\mathcal{E}_{\rm cl}$ is the total energy due to the presence of the cloud (see Equation 2.20), $\sigma_{\rm res}$ is the velocity dispersion of material that is being accreted, χ is given by Equation 2.23, γ is given by Equation 2.30, and φ is a free parameter that sets the amount of energy available to drive accretion driven turbulence. The parameter φ is the only adjustable constant in our model that is not constrained by the results of

simulations or observations and must be tuned to reproduce the observed properties of clouds. The evolution of the cloud is very sensitive to φ and we justify our fiducial choice, $\varphi = 0.75$, in section 2.5.

This equation governs the global energy budget of the cloud. Each term has a straightforward physical explanation. The term $(\dot{M}_{\rm cl}/M_{\rm cl})\mathcal{E}_{\rm cl}$ is the rate of change of the cloud's energy as mass is advectively added to or carried away from the cloud. Similarly, $(\dot{M}_{\rm cl}/M_{\rm cl})(1-\eta_{\rm B}^2)\mathcal{W}$ is the rate of change of the gravitational and magnetic energy due to changes in the mass of the cloud. The next term is the rate at which external pressure does compressional work on the cloud. This is followed by a term that accounts for the gravitational work done on the cloud by the reservoir as the cloud expands and contracts. The following term represents the rate at which mass inflows, outflows, and external thermal and turbulent pressure, respectively, do compressional work on the cloud. The next term, which is proportional to φ, represents the rate of kinetic energy injection via stirring of turbulence by accreted material. This is followed by two terms that are proportional to $\dot{M}_{\rm acc}$, which account for the fact that in the frame comoving with the motions of material in the cloud, accreted material is moving at the transformed velocity, $\mathbf{v}_{\rm res} - \mathbf{v}$, different than the velocity of the reservoir material in the rest frame, $\mathbf{v}_{\rm res}$. Lastly, $\mathcal{G}_{\rm cl}$ and $\mathcal{L}_{\rm cl}$ are the rate of energy injection by star formation and the rate at which energy is radiated away, respectively.

Noting that turbulent motions carry no net radial flux of matter and recalling that we had set $\mathcal{B}_{\rm turb} = 0.6\mathcal{T}_{\rm turb}$, we may evaluate Equation 2.20 and obtain for the

total cloud energy,

$$\begin{aligned}\mathcal{E}_{\rm cl} =& \frac{1}{2} a_I M_{\rm cl} \dot{R}_{\rm cl}^2 + 2.4 M_{\rm cl} \sigma_{\rm cl}^2 + \frac{3}{2} M_{\rm cl} c_{\rm cl}^2 \\ & - \left[\frac{3}{5} a'(1 - \eta_B^2) + \chi \right] \frac{G M_{\rm cl}^2}{R_{\rm cl}}.\end{aligned} \tag{2.49}$$

Taking the time derivative of this expression, substituting into Equation 2.48, and nondimensionalizing as in subsection 2.4.2 yields a time evolution equation for σ,

$$\begin{aligned}\frac{4.8}{a_I}\sigma' =& -\frac{R'R''}{\sigma} - \eta_G \frac{MR'}{R^2\sigma} - \eta_P \frac{R^2 R'}{M\sigma} \\ & + \eta_E \frac{M'_{\rm ej} R'}{M\sigma} - \eta_A \frac{M'_{\rm acc} R'}{(MR)^{1/2}\sigma} - \frac{M'_{\rm acc} R'^2}{M\sigma} \\ & - \frac{(3 - 1.5\varphi) M'_{\rm acc} \sigma}{a_I M} + \eta_D \frac{\varphi \varsigma M'_{\rm acc}}{M\sigma} + \eta_I \frac{\varphi\gamma M'_{\rm acc}}{fR\sigma} \\ & + \frac{\mathcal{G} - \mathcal{L}}{a_I M \sigma}\end{aligned} \tag{2.50}$$

where $\varsigma = \sigma_{\rm res}/\sigma_{\rm res,0}$,

$$\mathcal{G} - \mathcal{L} = \frac{R_{\rm cl,0}(\mathcal{G}_{\rm cl} - \mathcal{L}_{\rm cl})}{M_{\rm cl,0}\sigma_{\rm cl,0}^3}, \tag{2.51}$$

and we define the constants,

$$\eta_D = \frac{3\sigma_{\rm res,0}^2}{2a_{\rm I}\sigma_{\rm cl,0}^2}, \tag{2.52}$$

$$\eta_I = \frac{10}{a_{\rm I}\alpha_{\rm vir,0}}. \tag{2.53}$$

Here, η_D is propotional to the ratio of the initial turbulent kinetic energy in the reservoir and the initial turbulent kinetic energy in the cloud and η_I is proportional to the ratio of the initial kinetic energy due to the infall of the reservoir to the initial turbulent

kinetic energy of the cloud.

Since motions in GMCs are highly supersonic, the internal structure of a typical cloud is characterized by strong shocks. Because clouds have short cooling timescales, the shocks present throughout GMCs must be radiative. The braking of turbulent motions via radiative shocks has been extensively studied in numerical simulations (see e.g. Mac Low et al., 1998; Stone et al., 1998) in which the turbulent dissipation timescale is found to be $t_{\rm dis} = E_{\rm turb}/\dot{E} = k\lambda_{\rm in}/\sigma_{\rm cl}$ where k is a constant of order unity and $\lambda_{\rm in}$ is the characteristic length scale of turbulent energy injection. The simulations of Stone et al. (1998) give $k = 0.48$ and $E_{\rm turb} = 2.4 M_{\rm cl}\sigma_{\rm cl}^2$. Motivated by this result and using a scaling argument given by Matzner (2002) and McKee (1989), we assume that the dimensionless rate of energy loss is given by

$$\mathcal{L} = \frac{\eta_v}{\phi_{\rm in}}\frac{M\sigma^3}{R}. \tag{2.54}$$

Here η_v is a constant of order unity that depends on the nature of MHD turbulence in the cloud and we assume $\phi_{\rm in} = \lambda_{\rm in}/4R_{\rm cl}$. The factor of 4 in our expression for $\phi_{\rm in}$ comes from the fact that the largest wavelength mode supported by the cloud is $\lambda_{\rm max} = 4R_{\rm cl}$, corresponding to net expansion or compression of the cloud. We make use of the simulations of Stone et al. (1998) to calibrate this expression. For the run most resembling real molecular clouds, we find $\eta_v = 1.2$. We follow KMM06 in adopting $\phi_{\rm in} = 1.0$ below. This is motivated by the results of Brunt et al. (2009) (but see also Ossenkopf & Mac Low, 2002; Heyer & Brunt, 2004) who compared the velocity structure of observed clouds, where $\lambda_{\rm in}$ cannot be directly observed, with the velocity structure

of simulated clouds, where $\lambda_{\rm in}$ is known *a priori*, and found $\lambda_{\rm in} \gtrsim R_{\rm cl}$.

Comparing our velocity dispersion evolution equation (Equation 2.50) to the corresponding equation given in KMM06, we see there are four new terms proportional to $M'_{\rm acc}$. In practice, we find that the primary effect of accretion on the energy balance of the cloud is to increase the turbulent velocity dispersion via the terms proportional to φ. We will show in subsection 2.6.2 that the velocity dispersion is set by a balance between the decay of turbulence and energy injected by accretion and star formation.

2.4.4 Star Formation and H ii Regions

Star formation is able to influence the evolution of the cloud by ejecting mass and by injecting turbulent kinetic energy as expanding H II regions merge with and drive turbulent motions in the cloud. The first mechanism is accounted for in our models by including an ionized wind that decreases the mass of the cloud and confines the cloud by supplying recoil pressure. The second mechanism is accounted for by the $\mathcal{G}_{\rm cl}$ term in Equation 2.48 that represents energy injection by H II regions.

Since we only know the global properties of the cloud, we calculate the rate of star formation by making use of a power-law fit to the star formation law of Krumholz & McKee (2005). Stars form at a low efficiency per free-fall time, consistent with observations of star formation in nearby molecular clouds (Krumholz & Tan, 2007a). Individual star formation events occur once a sufficient amount of mass has accumulated to form a star cluster. Star cluster masses are found by drawing from a cluster mass function appropriate for a single cloud (see equation [44] of KMM06). We then populate the cluster with individual stars by picking masses from a Kroupa (2002) IMF. If the

total ionizing luminosity of the newborn star cluster is sufficient to drive the expansion of an H II region, we begin to track the resulting expansion.

Once a massive star cluster forms, it photoionizes gas in its surroundings and drives the expansion of an H II region. KMM06 tracked the expansion of individual H II regions by assuming the analytic self-similar solution for H II region expansion worked out by Matzner (2002). This solution uses the fact that once an H II region has expanded beyond the Strömgren radius, most of the mass in the H II region volume is in a thin shell of atomic gas at a radius $r_{\rm sh}$ from the center of the H II region. The ionized gas in the interior of the shell exerts a pressure on the surface of the shall, causing the shell to accelerate outwards. The shell evolution equation derived from this analysis admits a self-similar solution for the expansion of the H II region. This self-similar result does a good job of predicting the expansion if there is no characteristic scale in the problem.

However, the introduction of radiation pressure leads to a characteristic radius, $r_{\rm ch}$, and time, $t_{\rm ch}$, at which the gas pressure and radiation pressure at the inner surface of the shell are equal. Radiation pressure is the dominant force driving the expansion of the ionized bubble when $r_{\rm sh} < r_{\rm ch}$ and gas pressure dominates when $r_{\rm sh} > r_{\rm ch}$. KM09 modified the theory of Matzner (2002) to account for the effect of radiation pressure in the initial stages of the expansion. They derived an explicit functional form for $r_{\rm ch}$ and $t_{\rm ch}$ in terms of the bolometric and ionizing luminosity of the central star cluster, properties of the molecular cloud, and fundamental constants (see equations [4] and [9] in KM09). The numerical value of $r_{\rm ch}$ and $t_{\rm ch}$ depends on the the bolometric luminosity of the central star cluster and the ionizing photon flux of the central star cluster. The

value we choose for $f_{\rm trap}$, a factor that accounts for the trapping and reradiation of photons as well as the trapping of main sequence winds within the neutral shell, and ϕ, a factor that accounts for the absorption of radiation by dust, are the fiducial values quoted by KM09.

Defining the dimensionless variables $x_{\rm sh} = r_{\rm sh}/r_{\rm ch}$ and $\tau_{\rm sh} = t/t_{\rm ch}$, the equation of motion for the shell reduces to (KM09)

$$\frac{d}{d\tau_{\rm sh}}\left(x_{\rm sh}^2 \frac{dx_{\rm sh}}{d\tau_{\rm sh}}\right) = 1 + x_{\rm sh}^{1/2}. \tag{2.55}$$

This assumes that gas in the neighborhood of the H II region follows a density profile proportional to r^{-1}, effectively placing the H II region in the center of the cloud. This accounts for the fact that H II regions form in overdense regions of the cloud. In practice, we solve Equation 2.55 numerically to obtain $x_{\rm sh}$ and $dx_{\rm sh}/d\tau_{\rm sh}$ and thus $r_{\rm sh}(t)$ and $\dot{r}_{\rm sh}(t)$.

In a gas pressure driven H II region, the force exerted on the expanding bubble is twice the recoil force photoionized material imparts on the cloud as it is ejected (Matzner, 2002). The photoevaporation rate can then be straightforwardly calculated via $\dot{M}_{\rm ej} = -\dot{p}_{\rm sh}/2c_{\rm II}$. Here $p_{\rm sh}$ is the momentum of the shell and $\dot{p}_{\rm sh}$ is the force acting on the shell. In a radiation pressure driven H II region, the total force is given by the sum of the gas pressure and radiation pressure forces, $\dot{p}_{\rm sh} = \dot{p}_{\rm gas} + \dot{p}_{\rm rad}$. At early times, when $r_{\rm sh} \ll r_{\rm ch}$, the radiation force dominates, so $\dot{p}_{\rm rad} \gg \dot{p}_{\rm gas}$. Thus, If we calculate the mass ejection rate from the the total force acting on the shell, we will overestimate the mass ejection rate in a radiation pressure dominated H II region. To correct for this

effect, we modify the analysis of KMM06 by only including the gas pressure force when we calculate the mass ejection rate,

$$\dot{M}_{\rm ej} = -\frac{\dot{p}_{\rm gas}}{2c_{\rm II}} \tag{2.56}$$

where,

$$\dot{p}_{\rm gas} = \left(\frac{12S\phi\pi}{\alpha_{\rm B}}\right)^{1/2} 2.2 k_{\rm B} T_{\rm II} r_{\rm sh}^{1/2} \tag{2.57}$$

$$= 3.3 \times 10^{28} L_{39}\, x_{\rm sh}^{1/2} \text{dynes}. \tag{2.58}$$

Since we do not include the dynamical ejection of material as H II regions break out of the cloud surface, this is formally a lower limit on the true mass ejection rate. Since clouds are clumpy and somewhat porous (Lopez et al., 2011), we expect to make little error by neglecting dynamical ejection.

Once the stars providing 50% of the total ionizing luminosity of the central star cluster have left the main sequence, the H II region enters an undriven momentum-conserving snowplow phase. When the expansion velocity of the H II region is comparable to the turbulent velocity dispersion, we assume that the H II region breaks up and contributes turbulent kinetic energy to the cloud. H II regions can merge with the cloud during either the driven or undriven phases. If the radius of the H II region is greater than the radius of the cloud and the expansion velocity of the shell is greater than the cloud escape velocity, we say the H II region disrupts the cloud and end the global evolution.

If an H II region merges with the cloud at time $t = t_m$ when its radius is $r_{\rm sh} = r_{\rm m}$, the rate of energy injection from a single H II region is given by

$$\mathcal{G}_{\rm cl} = 1.6\eta_E \mathcal{T}_1(t_m) \left(\frac{r_m}{R_{\rm cl}}\right)^{1/2} \delta(t - t_m). \tag{2.59}$$

Here $\mathcal{T}_1(t_m) = p_{\rm sh}\sigma_{\rm cl}/2$, η_E paramaterizes the efficiency of energy injection, $\delta(t)$ is the Dirac delta function, and the factor of 1.6 arises because magnetic turbulence is slightly sub-equipartition compared to kinetic turbulence. The factor $(r_m/R_{\rm cl})^{1/2}$ accounts for the more rapid decay of turbulence when the driving scale is smaller (see KMM06).

2.4.5 Mass Accretion

Consistent with the analysis in section 2.3, we treat the reservoir as a gravitationally unstable spherical cloud undergoing collapse. The cloud is primarily composed of atomic gas in both warm and cold phases. We expect that as the reservoir collapses, material that is accreted onto the cloud will cool and become molecular. We approximate that the reservoir has approximately constant surface density, $\Sigma_{\rm res}$. To find an upper limit on the mass accretion rate, we can assume that the reservoir is undergoing collapse in the limit of zero pressure. It is straightforward to show that the resulting accretion rate onto the central condensation is given by

$$\dot{M}_{\rm acc,ff} = \frac{256}{\pi} G^2 \Sigma_{\rm res}^3 t^3 \tag{2.60}$$

Since the estimate for the accretion rate given in Equation 2.60 does not take into account pressure support, it is likely an overestimate of the true accretion rate. Indeed,

McKee & Tan (2003) considered the inside out collapse of equilibrium polytropic molecular cloud cores and, in the case of $k_\rho = 1$, found the same scaling with time and surface density but a substantially lower coefficient. Tan & McKee (2004) argued that subsonic inflow was a more realistic initial condition condition than the static equilibrium solution used by McKee & Tan (2003). Hunter (1977) found that the set of solutions for the collapse of an isothermal sphere starting at an infinite time in the past. The solution with an infall velocity of about $c_{\rm cl}/3$ corresponds well to the results of the simulation of the formation of a primordial star by Abel et al. (2002). Tan & McKee (2004) adopted this solution, noting that it has an accretion rate that is 2.6 times greater than that for a static initial condition (Shu, 1977) when expressed in dimensionless form. Our problem is quite different from Hunter's, since an equilibrium density gradient $k_\rho = 1$ corresponds to $\gamma = 0$ (McKee & Tan, 2003) rather than Hunter's $\gamma = 1$. Nonetheless, we assume that the accretion rate for our problem is also 2.6 times greater than that for a static initial condition and find

$$\dot{M}_{\rm acc,TM04} = 10.9\, G^2 \Sigma_{\rm res}^3 t^3. \tag{2.61}$$

Clearly, this result is uncertain, and magnetic fields introduce further uncertainty. Fortunately, we find that varying the numerical coefficient in Equation 2.61 does not affect the qualitative nature of the results discussed below.

To model the effect of a finite gas supply, once the total mass of gas that has fallen onto the cloud exceeds the total mass of the reservoir, $M_{\rm res}$, we set $\dot{M}_{\rm acc} = 0$. When comparing with galactic populations of GMCs, we set $M_{\rm res} = 6 \times 10^6 {\rm M}_\odot$, the

observed upper mass cutoff for GMCs (Williams & McKee, 1997; Fukui & Kawamura, 2010). This may underestimate the true upper mass since fragmentation may lead to a range of reservoir masses. Since $6 \times 10^6 \mathrm{M}_\odot$ GMCs are relatively rare, we set $M_{\rm res} = 2 \times 10^6 \mathrm{M}_\odot$ for the runs presented in Figure 2.4 as $\sim 10^6 \mathrm{M}_\odot$ is a more typical GMC mass.

If we also assume that the atomic reservoir is virialized such that the virial parameter of the reservoir, $\alpha_{\rm res}$, is constant with radius, we find

$$\sigma_{\rm res} = 0.4 \alpha_{\rm res}^{1/2} G \Sigma_{\rm res} t \tag{2.62}$$

Fiducially, we take $\alpha_{\rm res} = 2.0$, corresponding to a marginally gravitationally bound reservoir. This parameterization assumes that the reservoir satisfies an internal linewidth-size relation of the form $\sigma_{\rm res}(r) \propto r^{1/2}$. The increase of the reservoir velocity dispersion with time reflects that material originates at increasingly larger radii.

The precise normalization of the mass accretion law is a major source of uncertainty in our modeling. Since the length scales over which material is swept up into the cloud through the reservoir approach galactic dynamical scales (Dobbs et al., 2011; Tasker, 2011), a more complete treatment would require tracking the gas dynamics from the scale of an entire galaxy down to the the scale of the reservoir. This would also allow us to self-consistently model the end of accretion onto the cloud instead of assuming that mass accretion cuts off abruptly. In a forthcoming paper, we plan to add our molecular cloud models to a simulation of gas dynamics in a galactic disk to model the gas reservoir for a population of GMCs.

Although the normalization of the accretion law is somewhat uncertain, we can make use of observations of the gas content of nearby galaxies to estimate $\Sigma_{\rm res}$, the surface density of gas in the reservoir feeding the cloud. The average H I surface density in the inner disk of the Milky Way is observed to be approximately constant, $\sim 8 M_\odot {\rm pc}^{-2}$ (Kalberla & Dedes, 2008). Beyond a galactocentric radius of $\sim 10-15$kpc, the H I surface density exponentially decreases with radius, however, few GMCs are observed in the outer Milky Way (Heyer et al., 2001) or beyond the optical radius of nearby galaxies (Engargiola et al., 2003; Bigiel et al., 2008b). Similar saturated mean H I surface densities are observed in nearby galaxies, except in the central regions of some galaxies where the ISM becomes fully molecular and the H I surface density goes to zero (Leroy et al., 2008b). For this reason, we adopt $\Sigma_{\rm res} = 8 M_\odot {\rm pc}^{-2}$ as a fiducial atomic reservoir surface density typical of the bulk ISM of local star forming galaxies.

Although the *mean* atomic surface density in nearby galaxies is as low as $8 M_\odot {\rm pc}^{-2}$, the atomic ISM is observed to be clumpy, with overdense regions reaching significantly higher surface densities. These regions may be associated with spiral arms, as in M 33 (Thilker et al., 2002), or driven by gravitational instability, as in the LMC (Yang et al., 2007). For this reason, we also explore the behavior of molecular clouds accreting from higher surface density gas, $\Sigma_{\rm res} = 16 M_\odot {\rm pc}^{-2}$. Since massive molecular clouds are universally observed to be associated with high surface density gas (Wong et al., 2009; Imara et al., 2011), we expect there to be marked differences between molecular clouds that accrete from high surface density gas and clouds that accrete from low surface density gas. Although the gas will be primarily atomic at a gas surface

density of $16 M_\odot pc^{-2}$, we expect that there should be some diffuse "dark" molecular gas (Krumholz et al., 2008; Wolfire et al., 2010). Thus the reservoir is not necessarily completely atomic, but instead primarily composed of atomic gas.

2.4.6 Numerical Scheme

Equation 2.38, Equation 2.41, and Equation 2.50 constitute a system of coupled, stochastic, nonlinear ordinary differential equations in M, σ, and R. We solve these equations by using a straightforward Euler integration with an adaptive step size. The precise order in which we update cloud properties is as follows. After calculating the instantaneous star formation rate, we calculate M' by summing the components due to ionized winds and mass accretion. Next, we calculate the rate of turbulent dissipation using Equation 2.54. We then calculate ζ, the ratio of the mass doubling time to the free-fall time, using Equation 2.13. We use ζ to calculate a', f, and ξ by interpolating on precomputed tables. Since σ' depends on R'', we first evaluate R'' using Equation 2.41 and then compute σ' using Equation 2.50. Next, we check if R, M, or σ will change by more that 0.1 % using the current value of the time step. If we detect a change larger than this, the time step is iteratively recalculated using a new time step half the size of the original until the fractional changes in R, M, and σ are smaller than 0.1 %. Next, we calculate R, M, and σ at the new time step, update the state of any H II regions created in previous time steps, and then create new H II regions using the procedure described in subsection 2.4.4. If the time step did not need to be reduced, we increase the size of the time step by 10%.

Cloud evolution can be terminated if one of three conditions is satisfied:

- The time step is less than 10^{-8} of the current evolution time (i.e. $\Delta\tau/\tau < 10^{-8}$).
- The mean visual extinction falls below $A_{V,\mathrm{min}} = 1.4$, corresponding to the CO dissociation threshold found by van Dishoeck & Black (1988).
- An H II region envelops and unbinds the cloud, i.e. if $r_{\mathrm{sh}} > R_{\mathrm{cl}}$ and $\dot{r}_{\mathrm{sh}} > v_{\mathrm{esc}}$.

We use the phrases collapse, dissociation, and disruption, respectively to describe these scenarios. The dissociation threshold depends on the ambient radiation field. However, Wolfire et al. (2010) found that the CO dissociation threshold varies by only a factor of two when the intensity of the ambient radiation field varies by an order of magnitude, so we neglect variations in the radiation field and for consistency with KMM06, adopt $A_{V,\mathrm{min}} = 1.4$. The surface density corresponding to the dissociation threshold depends on the assumed dust to gas ratio and thus on the metallicity. For solar metallicity, a surface density of $1\mathrm{gcm}^{-2}$ corresponds to $A_V = 214.3$. Since we use a dissociation threshold based on CO rather than H_2 to define the end of the cloud's life, we may miss the further evolution of a diffuse molecular cloud where most of the carbon is neutral or singly ionized but the hydrogen is still molecular.

These halting conditions probably oversimplify the true end of a cloud's evolution due to our assumption of spherical symmetry and homology. For the case of collapse, it is more likely that the cloud would undergo runaway fragmentation rather than monolithic collapse. In the case of dissociation, even if the mean surface density drops below the point where CO can no longer remain molecular, that does not preclude the possibility that overdense clumps might retain significant amounts of CO. Finally, for the case of disruption, even if an H II region delivered a large enough impulse to

unbind the cloud, it may simply be displaced as a whole, or be disrupted into multiple pieces which would then evolve independently. It is also likely that if the cloud is disrupted while still actively accreting, the cloud would inevitably recollapse since it is unlikely that an H II region would have enough kinetic energy to unbind the reservoir.

Since we must necessarily use simple criteria to halt the cloud evolution, our estimates of cloud lifetimes presented below are strictly lower limits to the true lifetime of a cloud. Both the disruption and dissociation criteria do not preclude the presence of overdense clumps that may survive the destruction events. However, our estimates of cloud lifetimes are appropriate for the lifetime of a single monolithic cloud. Any overdense clumps that do survive would represent entirely different clouds that would evolve independently of each other.

2.4.7 Input Parameters

Table 2.1: Fiducial Parameters

Parameter	Value	Reference
$\alpha_{\rm vir,0}$	2.0	Blitz et al. (2007)
$\Sigma_{\rm cl,0}$	$60 M_\odot {\rm pc}^{-2}$	Heyer et al. (2009)
c_s	$0.19 {\rm kms}^{-1}$	—
$c_{\rm II}$	$9.74 {\rm kms}^{-1}$	McKee & Williams (1997)
η_B	0.5	Krumholz & McKee (2005)
η_E	1.0	KMM06
η_v	1.2	KMM06

$\phi_{\rm in}$	1.0	Brunt et al. (2009)
φ	0.75	This work
$A_{\rm v,min}$	$1.4 {\rm M}_\odot {\rm pc}^{-2}$	van Dishoeck & Black (1988)
$\alpha_{\rm res}$	2.0	—
$P_{\rm amb}/k_{\rm B}$	$3 \times 10^4 {\rm Kcm}^{-3}$	McKee (1999)
$M_{\rm cl,0}$	$5 \times 10^4 {\rm M}_\odot$	—

To complete our model, we must choose a set of parameters and initial conditions to fully determine our cloud evolution equations. In Table 2.1 we have listed the various fiducial parameters we have chosen for our model as well as the references from which we derive our choices. Some of these parameters are motivated by observations, others by the results of simulations, and one parameter (φ, see section 2.5) is left free.

The cloud initial conditions can be computed given an initial cloud mass along with our assumed value for $\alpha_{\rm vir,0}$ and $\Sigma_{\rm cl,0}$. Matzner & McKee (2000) and Fall et al. (2010) found that protostellar outflows are energetically important when $M_{\rm cl} \lesssim 10^{4.5} {\rm M}_\odot$. Above this mass, they contribute negligibly. Thus, if we choose a low initial mass, we may be underestimating the amount of turbulent energy injection by star formation feedback at early times since we do not account for protostellar outflows. For this reason, we choose a relatively large initial mass, $M_{\rm cl,0} = 5 \times 10^4 {\rm M}_\odot$. For reference, given our choice of initial virial parameter and surface density, this corresponds to, $R_{\rm cl,0} = 11.5 {\rm pc}$, $\sigma_{\rm cl,0} = 2.7 {\rm kms}^{-1}$, and $t_{\rm cr,0} = 4.1 {\rm Myr}$. While this is larger than some local molecular clouds like Taurus or Perseus, it is still much smaller than the mass of the molecular clouds where most of the star-formation in local galaxies occurs. This

choice also ensures that we are accounting for the bulk of the energy available from star formation feedback due to photoionization, ionized gas pressure, and radiation pressure.

2.5 Models with Accretion Only

Before beginning full simulations using our method, we must first test the behavior of our model as we vary the free parameter φ introduced in the derivation of the energy evolution equation. For this purpose, we have run our model with star formation feedback disabled. The only physical mechanisms modeled in these tests are accretion and the decay of turbulence. Since there is no random drawing from the stellar or cluster IMF in these runs, the results are fully deterministic. These simplified models allow us to understand how the results depend on our choice for the tunable parameter φ and provide physical insight that will be useful in interpreting the results of the more complex and stochastic runs that include feedback.

The energetics and virial balance of our cloud models depend critically on the parameter φ. Broadly speaking, φ controls the amount of turbulent kinetic energy injected by the accretion flow. For the case $\varphi = 0$ the accretion flow contributes the minimum possible amount of turbulent kinetic energy. This means that accreted material cannot contribute significantly to turbulent pressure support, since the accreted material is maximally subvirial. With this choice, as the cloud accretes mass, its energy budget must become increasingly dominated by self-gravity. Once this happens, internal pressure support is negligible and the cloud must inevitably undergo gravitational collapse.

Alternatively, we could set $\varphi > 0$. If φ is small, the turbulent kinetic energy of a newly accreted parcel of gas would still be small compared to the gravitational potential energy of the gas parcel. Thus, once the cloud is primarily composed accreted gas, the cloud will undergo gravitational collapse, although on a slightly longer timescale than in the $\varphi = 0$ case. At some larger value of φ, accretion contributes a net positive amount of energy to the cloud, balancing out the negative gravitational potential energy of the newly accreted material. The could will still collapse with this choice since turbulent motions quickly decay away. As φ is increased further, we should eventually find that at some critical value, $\varphi = \varphi_{\rm crit}$, accretion drives turbulent motions with sufficient vigor to avoid the gravitational collapse of the cloud entirely.

The results of test runs with different choices of φ are presented in Figure 2.3. The time evolution of the cloud surface density, virial parameter, velocity dispersion, and cloud radius is plotted for a selection of clouds evolved with different choices for φ. Each line depicts the time evolution of a cloud property and is color coded by the value of φ chosen. It is obvious that the value of φ can strongly influence the resulting evolution.

If $\varphi = 0$, the cloud experiences global collapse in a free-fall time. Initially, the cloud velocity dispersion decreases, but inevitably the gravitational term in the velocity dispersion evolution equation, proportional to $-R'/R^2$, becomes dominant, and the velocity dispersion begins to diverge. The fact that $\sigma_{\rm cl}$ diverges as $R_{\rm cl}$ goes to zero is an artifact. In reality, the highest density regions would independently fragment and collapse and the cloud would never undergo a monolithic collapse.

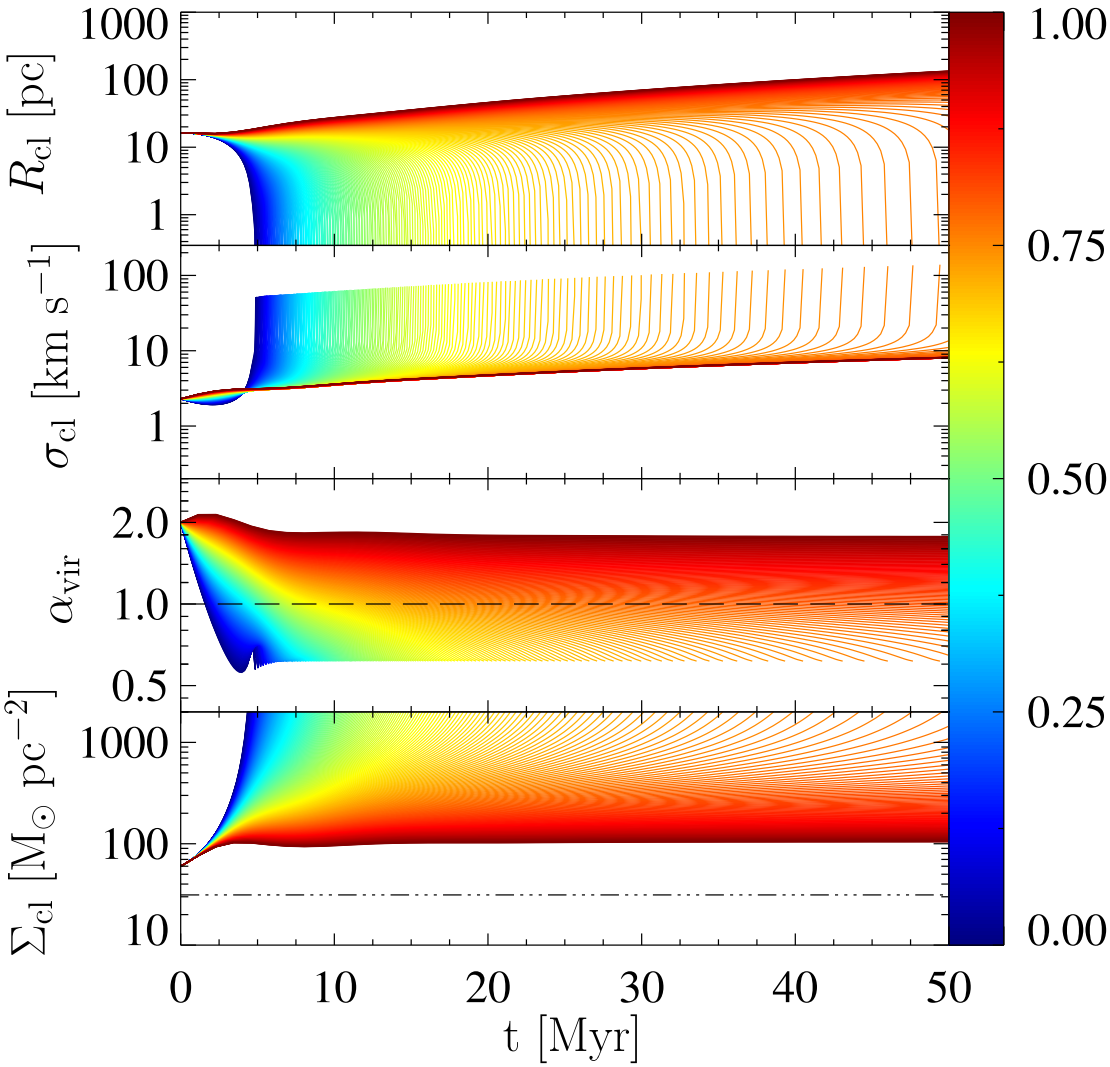

Figure 2.3: Cloud surface densities (*bottom row*), virial parameters (*second row*), velocity dispersions (*third row*), and radii (*top row*) for 400 different runs, each with a different choices for φ, as indicated in the color bar. Star formation was turned off for all runs.

As we increase φ, the cloud is able to support itself against collapse for longer periods. Near $\varphi = 0.5$, accretion brings in net positive energy but turbulent dissipation wins out, and the cloud still eventually collapses. At a critical value, $\varphi_{\rm crit} \simeq 0.8$, accretion driven turbulence alone is sufficient to hold up the cloud against collapse for as long as the reservoir continues to supply mass to the cloud. The mass, radius, and velocity dispersion of the cloud increase in such a way as to maintain a constant virial parameter and surface density.

Since we expect that gas motions driven by accreting dense clumps should be at least somewhat correlated with the motions of the infalling clumps, we do not expect a physically realistic choice of φ to be very close to zero. On the other hand, a model in which a cloud is entirely supported by accretion driven turbulence seems to preclude the possibility that a significant fraction of the kinetic energy of infalling gas is radiated away in an accretion shock. For this reason, we rule out as unphysical runs with $\varphi \approx 0$ and $\varphi \geq \varphi_{\rm crit}$. The precise value of φ we will use in our models that include star formation below depends on uncertain details of the accretion and mixing of infalling gas. In practice, we find that even with the energy provided by star formation feedback, clouds generally undergo free-fall collapse or reach unreasonably high mean surface densities once they are primarily composed of accreted material if we choose $\varphi \lesssim 0.7$. Since clouds are generally not observed to be in global free-fall collapse, we instead pick a value somewhat higher that this, $\varphi = 0.75$ for our fiducial models. This splits the difference between accretion contributing a negligible amount of energy to the cloud when $\varphi = 0.5$ and accretion contributing the maximum possible amount of energy

when $\varphi = 1$. We will see below that our fiducial choice broadly reproduces the observed properties of molecular clouds in the Milky Way and nearby galaxies.

2.6 Models with Accretion and Star Formation

Feedback by the action of ionizing radiation emitted by newborn stellar associations alters the evolution of a GMC after the birth of the first massive star cluster. The source of energy provided by massive star formation can be a significant component of the energy budget of the entire cloud. For the remainder of this paper, we consider models with the star formation prescription described in subsection 2.4.4 turned on.

2.6.1 Overview of Results

We have run two sets simulations with parameters chosen to model conditions in interarm ($\Sigma_{\rm res} = 8 {\rm M}_\odot {\rm pc}^{-2}$) and spiral arm ($\Sigma_{\rm res} = 16 {\rm M}_\odot {\rm pc}^{-2}$) regions. Besides the two different choices for the ambient surface density, all other parameters and initial conditions are identical. The time evolution of a subsample of runs are plotted in Figure 2.4.

The most striking result of our comparison is that the final mass of our model molecular clouds depends on the assumed mass accretion history. Clouds evolved with a low accretion rate, corresponding to conditions in interarm regions, grow larger than $10^5 {\rm M}_\odot$ less than 30% of the time and very rarely reach masses comparable to the most massive GMCs in the local group. The vast majority of clouds are instead disrupted by an energetic H II region within a few crossing times. The clouds attain a quasi-

equilibrium configuration in which mass accretion is roughly balanced by mass ejection. Clouds avoid global collapse by extracting energy from the expansion of H II regions.

The evolution of the clouds is characterized by discrete energy injection events due to the formation of a single massive star cluster. Once a cluster forms, it ejects a wind and launches an H II region. The recoil force of launching the wind leads to an overall confining ram pressure, causing the radius to decrease and the surface density to increase. Once the star cluster burns out, the H II region expansion decelerates and then stalls. When the expansion velocity of the H II region is comparable to the cloud velocity dispersion, the kinetic energy of the expanding H II region is converted into turbulent kinetic energy, causing a spike in the turbulent velocity dispersion. The turbulent kinetic energy exponentially decays away over a crossing time, but the temporarily elevated velocity dispersion increases the turbulent kinetic pressure, causing the cloud to expand. This leads to oscillations in the cloud radius and mean surface density. On the whole, clouds that are not quickly disrupted by H II regions, are able to survive as quasi-virialized objects for several crossing times before they are either disrupted or dissociated.

Clouds evolved with a higher ambient surface density, typical of spiral arm regions in the Milky Way, exhibit significantly different behavior. Since these clouds accrete mass much faster than in the low surface density runs, they are not able to attain steady state between accretion and ejection of mass. While some clouds are still destroyed by energetic H II regions early in their evolution, over 90% of these clouds were able to accrete their entire reservoir after 25Myr. At this point, the clouds are

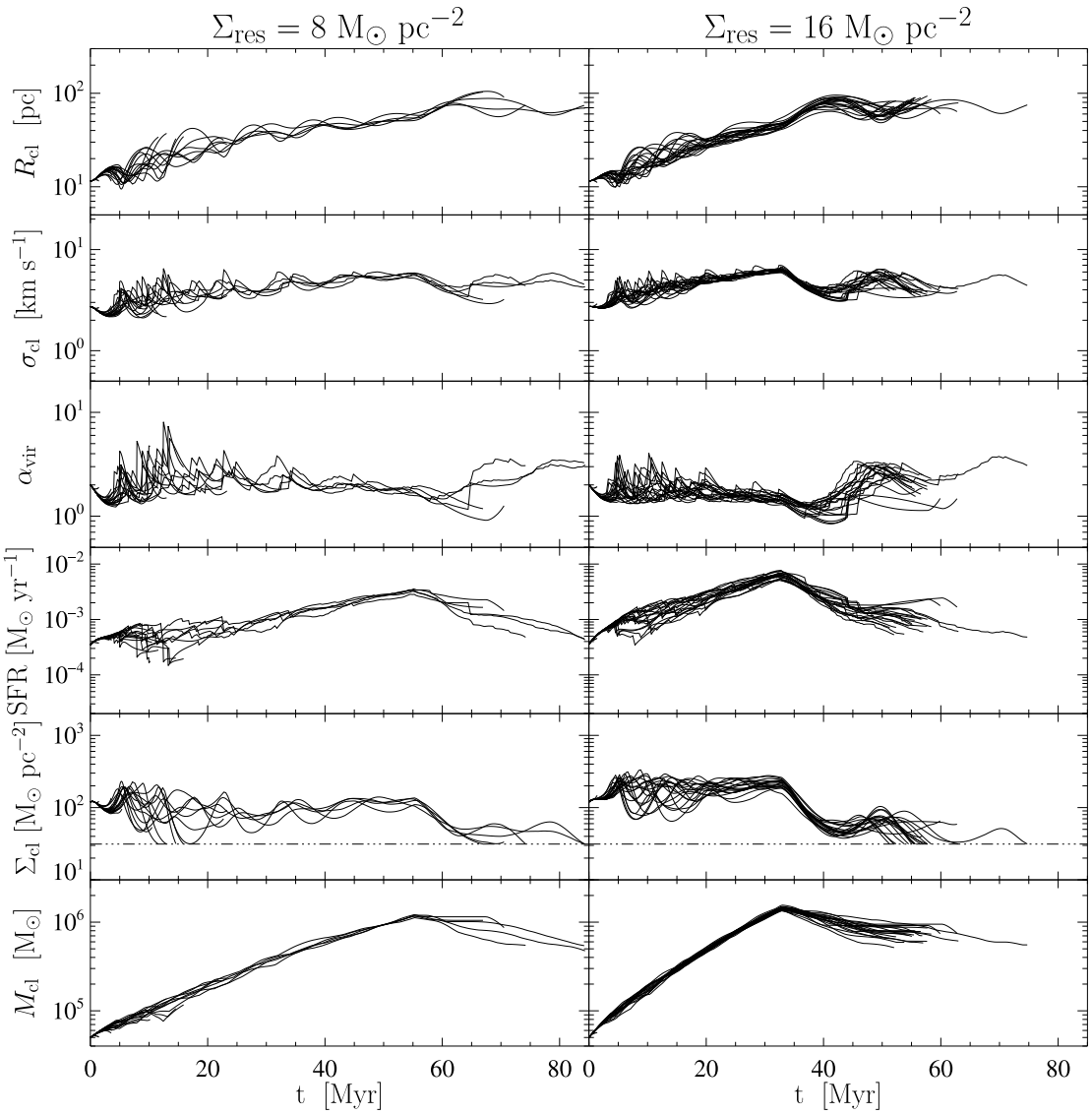

Figure 2.4: Cloud surface densities (*bottom row*), star formation rates (*second row*), virial parameters (*third row*), velocity dispersions (*fourth row*), and radii (*top row*) for a set of 40 clouds. Half of the clouds were evolved with a low surface density characteristic of the bulk of the atomic ISM and the other half were evolved with a high surface density, characteristic of overdense regions in the ISM. The two different choices of $\Sigma_{\rm res}$ are marked at top. Accretion was shut off once $10^6 {\rm M}_\odot$ of material had been processed through the accretion flow. The ambient surface density, and thus the accretion history, strongly affects the resulting cloud evolution.

generally quite massive, $\sim 1.5 \times 10^6 M_\odot$. Once accretion is shut off, the clouds are no longer confined by accretion ram pressure and lose a portion of the power that had been driving turbulence. For this reason, the velocity dispersion decreases in response to the loss of accretion driven turbulence, and the cloud radius expands in response to the loss of the confining pressure provided by accretion. Before the cloud can dissociate, it attains pressure balance with the ambient ISM at a lower velocity dispersion and larger radius. For the next 20 to 30 Myr, the clouds evolve in much the same way as the massive cloud models considered in KMM06. The clouds can be supported against self-gravity for many dynamical times by forming stars and launching H II regions. Particularly energetic H II regions can disrupt the clouds and excursions to low surface density can dissociate the clouds. The lifetime of these clouds is thus set by the amount of time they can accrete. This may imply that spiral arm passage times set GMC lifetimes, although further work is needed to clarify this tentative conclusion.

The star forming properties of the two sets of models are also somewhat different. In the interarm case, the star formation efficiency,

$$\epsilon = \frac{M_{*,\mathrm{tot}}}{\int_0^{t_{\mathrm{life}}} \dot{M}_{\mathrm{acc}} dt}, \tag{2.63}$$

is only 5% while in the high surface density case, ϵ is somewhat larger, approximately 8%. This can be entirely attributed to the difference in lifetimes between the two sets of models. In the low surface density case, most clouds are only able to survive one or two crossing times and thus can only convert a small fraction of their mass into stars before they are dissociated or disrupted. The clouds evolved with a high ambient surface

density are able to survive for many crossing times and convert a larger fraction of their gas into stars. An even larger fraction is ejected via photoionization. However, for both models, the star formation efficiency per free-fall time,

$$\epsilon_{\rm ff} = \frac{\dot{M}_*}{M_{\rm cl} t_{\rm ff}} \tag{2.64}$$

is low, around 2%. This is not surprising, as a low star formation efficiency per free-fall time is one of the basic assumptions of our model.

2.6.2 Energetics of Star Formation Feedback Versus Mass Accretion

GMCs exhibit highly supersonic turbulence. There is no agreement in the literature about what drives these motions, which numerical models of compressible MHD turbulence indicate should decay if left undriven. Some authors suggest that the primary energy injection mechanism is some sort of internal star formation feedback process, such as protostellar outflows (Li & Nakamura, 2006; Wang et al., 2010), expanding H II regions (Matzner, 2002), or supernovae (Mac Low & Klessen, 2004). Others suggest that turbulence is driven externally via mass inflows (Klessen & Hennebelle, 2010). Comparing the amount of energy injected by different forms of star formation feedback, Fall et al. (2010) found that at typical GMC column densities, the dominant stellar feedback mechanism is H II regions driven by the intense radiation fields emitted by massive star clusters. Using our models, we can compare the importance of accretion relative to H II regions in the energy budget of GMCs.

To find the total energy injected by accretion, we make use of our knowledge

of the total energy of the cloud as a function of time. At the end of time step j we use Equation 2.49 to calculate both the total cloud energy, $\mathcal{E}_{\mathrm{cl},j}$, as well as what the cloud energy would have been if we had set $\dot{M}_{\mathrm{acc}} = 0$ for that time step, $\mathcal{E}_{\mathrm{cl}}|_{\dot{M}_{\mathrm{acc}}=0}$. The difference,

$$\mathcal{E}_{\mathrm{acc,j}} = \mathcal{E}_{\mathrm{cl},j} - \mathcal{E}_{\mathrm{cl}}|_{\dot{M}_{\mathrm{acc}}=0} \tag{2.65}$$

is the total energy added by accretion during that time step. The total energy injected by accretion over the cloud's lifetime is just the sum of the contributions of each time step,

$$\mathcal{E}_{\mathrm{acc}} = \sum_j \mathcal{E}_{\mathrm{acc},j}. \tag{2.66}$$

The energy injected by H II region i, $\mathcal{E}_{\mathrm{H\,II},i}$, can be found by integrating the rate of energy injection by a single H II region with respect to time. This is,

$$\mathcal{E}_{\mathrm{H\,II},i} = 1.6\eta_E \mathcal{T}_{1,i} \left(\frac{r_{\mathrm{m},i}}{R_{\mathrm{cl},i}}\right)^{1/2} \tag{2.67}$$

where $r_{\mathrm{m},i}$ is the radius of H II region i when it merges with the parent cloud and $R_{\mathrm{cl},i}$ is the radius of the cloud as a whole when H II region i merged with the cloud. To find the total energy injected by H II regions over the cloud's lifetime, we simply sum up the contributions due to individual H II regions,

$$\mathcal{E}_{\mathrm{H\,II}} = \sum_i \mathcal{E}_{\mathrm{H\,II},i}. \tag{2.68}$$

The ratio $|\mathcal{E}_{\mathrm{H\ II}}/\mathcal{E}_{\mathrm{acc}}|$ indicates the relative importance of star formation feed-

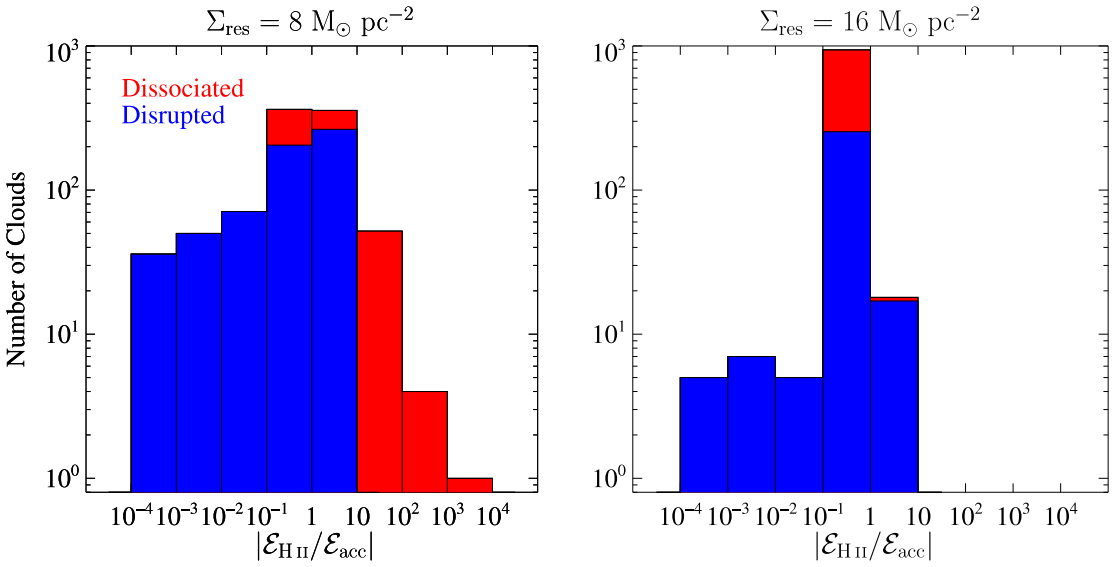

Figure 2.5: The number of clouds plotted as a function of $|\mathcal{E}_{\rm H\ II}/\mathcal{E}_{\rm acc}|$. In regions of low ambient surface density, accretion and star formation are in equipartition, while in regions of high ambient surface density, accretion dominates the energy budget.

back to accretion driven turbulence to the global energy budget of the cloud. If $|\mathcal{E}_{\rm H\ II}/\mathcal{E}_{\rm acc}| < 1$, accretion dominates the energy injection; similarly if $|\mathcal{E}_{\rm H\ II}/\mathcal{E}_{\rm acc}| > 1$, star formation feedback is the primary driver of turbulence.

The results of this comparison are plotted for both choices of the ambient surface density in Figure 2.5. We find that H II regions and accretion contribute approximately equal amounts of energy in the low surface density runs, while accretion dominates in the high surface density runs. In the low surface density runs, stochastic effects can be important, particularly for clouds that do not last much longer than a crossing time. Thus, in some runs, star formation feedback can contribute significantly more energy than accretion, while in others star formation feedback is negligible. In the runs evolved with a high ambient surface density, star formation feedback is subdominant, although not completely negligible, in the vast majority of runs.

It is worth pointing out that this result depends on the precise value of φ we choose to evolve the clouds with. If φ is lower, accretion contributes less energy, and star formation can dominate the energy budget. If φ is higher, star formation becomes completely negligible, and the amount of kinetic energy injection is controlled by the mass accretion rate. Since clouds collapse when we choose φ much lower than our fiducial value, and shocks in molecular gas tend to be strongly dissipative, we do not expect the 'true' value of φ to be much different than our fiducial value. We thus conclude that one of three cases must hold. Star formation may be dominant, but only marginally so. Accretion may also be dominant, but again, only marginally. It is also possible that star formation and accretion contribute roughly equal amounts of energy. In all three cases, neither star formation or accretion is truly negligible.

2.7 Observational Comparisons

2.7.1 Larson's Laws

Giant molecular clouds are observed to obey three scaling relations, known as Larson's laws (Larson, 1981; Solomon et al., 1987; Bolatto et al., 2008). In their simplest form, Larson's laws state:

- The velocity dispersion scales with a power of the size of the cloud. Subsequent observations have shown that this power is about 0.5 ($\sigma_{\rm cl} \propto R_{\rm cl}^{0.5}$).
- The mass of the cloud scales with the square of the radius (constant $\Sigma_{\rm cl}$).
- Clouds are in approximate virial equilibrium ($\alpha_{\rm vir}$ of order unity).

These laws are not independent; any two imply the other. At a minimum, an acceptable theoretical model for GMCs should agree with both the scaling and the normalization of the Larson scaling relations observed in real clouds. We have already seen that clouds maintain approximate virial equilibrium as well as roughly constant surface densities, but we have yet to see whether the normalization of the Larson scaling relations for our models agrees with the observed Larson scaling relations.

Equilibrium Surface Densities

GMCs, both in the Milky Way (Larson, 1981; Solomon et al., 1987), and in nearby external galaxies (Blitz et al., 2007; Bolatto et al., 2008) exhibit surprisingly little variation in surface density. For the Solomon et al. (1987) sample of Milky Way clouds, this was found to be $\langle \Sigma_{\rm cl} \rangle = 170 {\rm M}_\odot {\rm pc}^{-2}$. More recent and sensitive observations find lower values, closer to $\langle \Sigma_{\rm cl} \rangle = 50 {\rm M}_\odot {\rm pc}^{-2}$ in the Milky Way (Heyer et al., 2009) and in the Large Magellanic Cloud (Hughes et al., 2010), although these latter estimates depend on a highly uncertain correction for non-LTE line excitation and the CO to H_2 conversion factor, respectively. Using heterogenous data from several nearby galaxies, Bolatto et al. (2008) attempted to extract cloud properties in a uniform manner and found a typical surface density of $85 {\rm M}_\odot {\rm pc}^{-2}$ but with significant variation from galaxy to galaxy.

Variations in the mean GMC surface density are seen when comparing samples from different galaxies. However, within a single galaxy there is little variation (Blitz et al., 2007). These variations are usually attributed to differences in the CO-to-H_2 conversion factor from galaxy to galaxy (Bolatto et al., 2008), a quantity which may

depend on metallicity and the interstellar radiation field (Glover et al., 2010) as well as variations in turbulent pressure and radiation field in the ambient interstellar medium. In our runs, we also recover roughly constant surface densities (see the second row from the bottom of Figure 2.4).

In Figure 2.6, we have reproduced a figure from Blitz et al. (2007) that depicts observational results for CO luminosities and cloud radii for a sample of clouds in the outer Milky Way as well as from several samples of extragalactic GMCs. To compare against this compendium of results, we calculate CO luminosities for our model clouds by assuming a constant CO-to-H_2 conversion factor,

$$L_{\rm CO} = \frac{M_{\rm cl}}{8.8{\rm M}_\odot}{\rm Kkms^{-1}pc^2} \tag{2.69}$$

as in Rosolowsky & Leroy (2006). This formula accounts for the presence of helium and assumes a constant H_2 to CO conversion factor, $X_{\rm CO} = 4 \times 10^{20}{\rm cm^{-2}\,(Kkms^{-1})^{-1}}$, twice the value derived for molecular clouds within the Solar circle using observations of gamma-ray emission (Strong & Mattox, 1996; Abdo et al., 2010). We choose this value to be consistent with Blitz et al. (2007), who find, using this value of $X_{\rm CO}$, that all of the GMCs in their sample have virial masses comparable to the masses implied by their CO luminosity to within a factor of two.

With our fiducial initial conditions, model clouds in our sample begin their lives in the bottom left hand corner of Figure 2.6, at $R_{\rm cl} \approx 10$pc. As they accrete and expand, clouds move towards the upper right hand corner. Clouds end their evolution either through disruption by a single H II region or by passing below the molecular dissociation

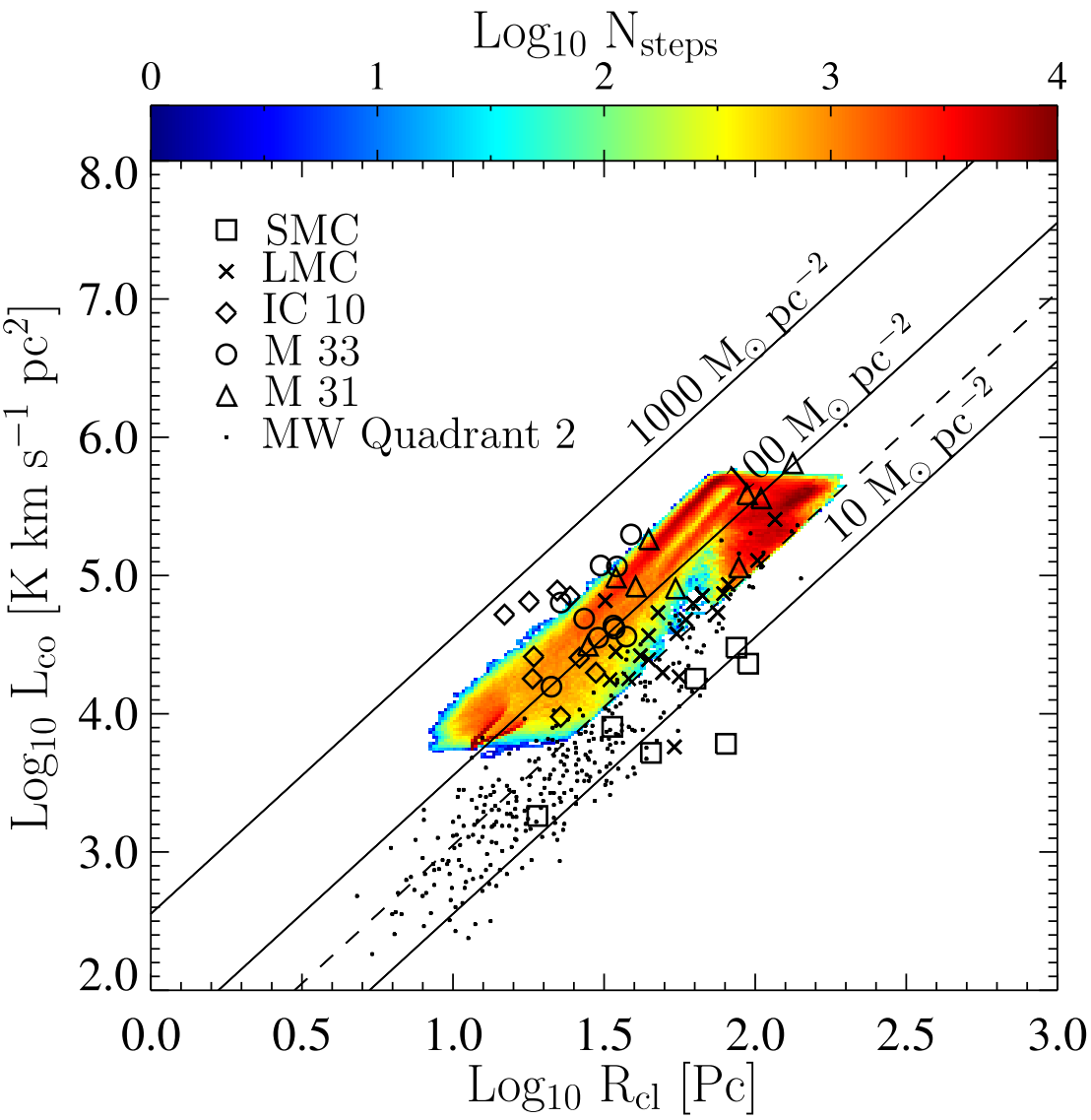

Figure 2.6: Cloud CO luminosity plotted as a function of cloud radius. CO luminosities are found by assuming $X_{\rm CO} = 4 \times 10^{20} {\rm cm}^{-2} ({\rm Kkms}^{-1})^{-1}$. Solid lines of constant surface density are plotted for 10, 100, and $1000 {\rm M}_\odot {\rm pc}^{-2}$ for reference. The dashed line of constant surface density corresponds to our assumed dissociation threshold. The outputs from a set of 2000 runs were used, with $\Sigma_{\rm res} = 8$ and $16 {\rm M}_\odot {\rm pc}^{-2}$ and $M_{\rm res} = 6 \times 10^6 {\rm M}_\odot$. Colors indicate the amount of time model clouds tend to occupy a position in $L_{\rm CO} - R_{\rm cl}$ parameter space. Symbols denote observed CO luminosities and cloud radii for galactic (*points*) and extragalactic (*open shapes*) GMCs. See Blitz et al. (2007) and references therein for details of the observations.

threshold, indicated by a dashed line in Figure 2.6. Offsets in the distribution of column densities from galaxy to galaxy and from the simulated clouds can be attributed to variations in $X_{\rm CO}$ and uncertainty in identifying a unique radius for observed clouds (Blitz et al., 2007) that have nonzero obliquity (Bertoldi & McKee, 1992). Accounting for variations in $X_{\rm CO}$, there is striking agreement between the observed distribution of molecular clouds and our sample of simulated clouds.

The models exhibit a kink in their evolution when the reservoir is exhausted and accretion is shut off. For this reason, there are no clouds with $L_{\rm CO} > 10^{5.6}{\rm Kkms^{-1}pc^2}$. Once accretion is shut off, the clouds decrease in mass for the remainder of their evolution. This kink is somewhat artificial since we have assumed a fixed reservoir mass and a smooth accretion history. A more sophisticated model for the reservoir including a range of reservoir masses would exhibit a continuous spectrum of kinks, broadening the region of parameter space explored by the models, particularly for $L_{\rm CO} < 10^{4.5}{\rm Kkms^{-1}pc^2}$.

The models also exhibit two distinct favored strips of parameter space along which they tend to evolve. This corresponds to the two different equilibrium column densities picked out by the two different choices of $\Sigma_{\rm res}$. This behavior is clearly seen in the second panel from the bottom of Figure 2.4. The fact that $\Sigma_{\rm cl}$ is sensitive to $\Sigma_{\rm res}$ follows from dimensional analysis.

Linewidth-Size Relation

We next compare our simulated clouds with the linewidth-size relation observed to hold among GMCs as a population (Bolatto et al., 2008). We are able to reproduce the power law, scatter, and the rough normalization in the observed linewidth-size

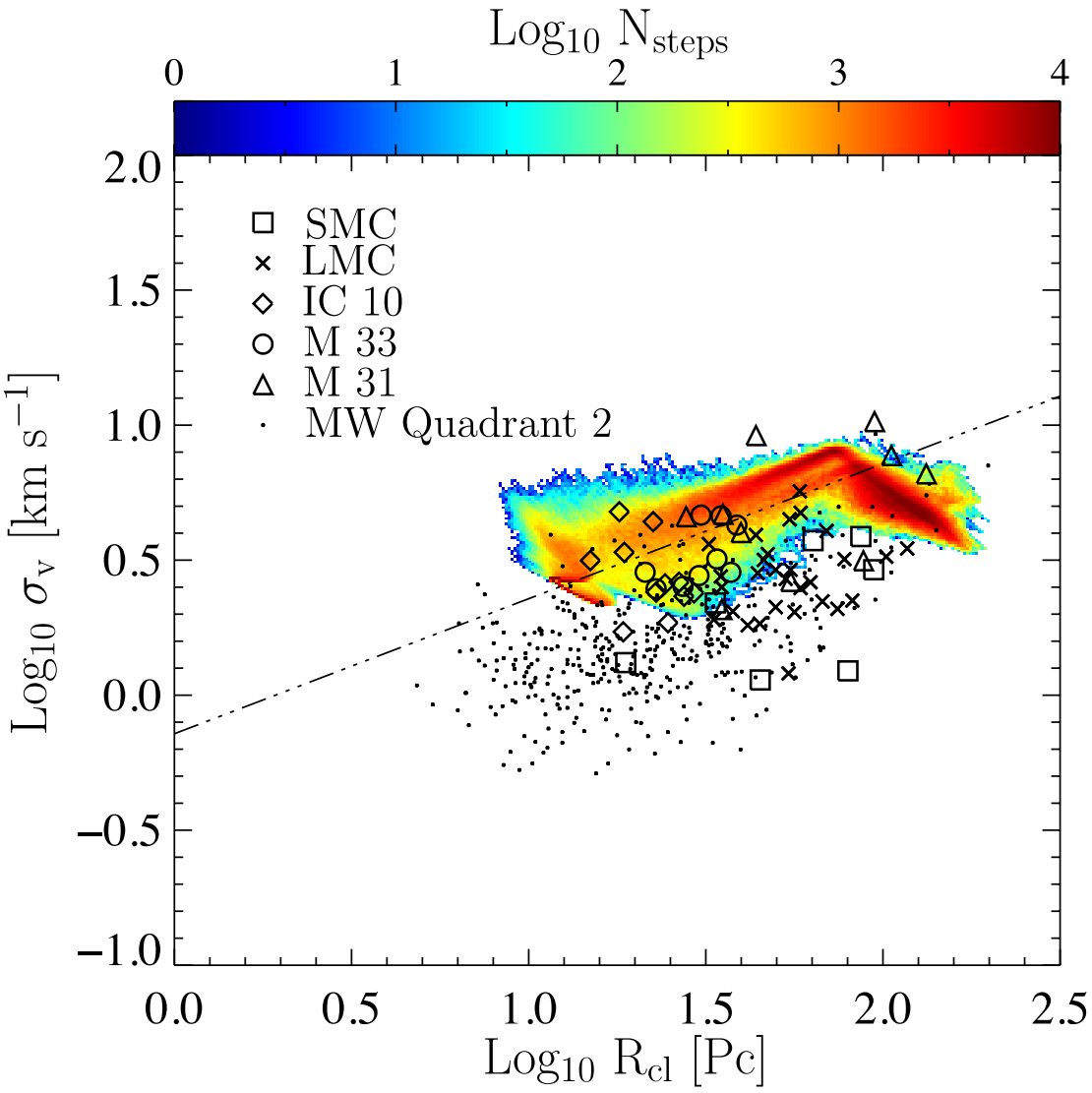

Figure 2.7: Cloud velocity dispersion plotted as a function of cloud radius. The dash-dotted line is the galactic linewidth-size relation found by Solomon et al. (1987), $\sigma_v = 0.72R^{0.5}$. Symbols and color coding are the same as in Figure 2.6.

relation. This conclusion is unsurprising, since we have already seen that our simulated clouds maintain roughly constant virial parameters and surface densities as they evolve. It is worth noting that for our simplified model for the environment of a GMC, that the linewidth-size relation corresponds to an age sequence. Clouds that live towards the left-hand side of the diagram are younger than clouds that live towards the right. It is possible that this conclusion is an artifact of choosing a single reservoir mass. Clouds accreting from a population of reservoirs with a continuous spectrum of masses may blur this effect somewhat. We plan to revisit this in future work in which we will model the global ISM of a galaxy simultaneously with the evolution of a population of GMCs.

There is a small offset when comparing the locus of extragalactic and outer Milky Way clouds with our models, although there is good agreement between our models and the scaling found by Solomon et al. (1987). For a subset of the observational sample, particularly the SMC clouds, it is possible that the metallicity of the gas in the clouds is so low that CO is no longer a good tracer of the bulk of the molecular gas (Leroy et al., 2007). Since our models assume perfect sphericity, and the observed radius of a prolate or oblate spheroid will always be smaller than the corresponding spherical radius (Bertoldi & McKee, 1992), it is also possible that the radii predicted by our models overpredict the corresponding observed cloud radius by 0.1 or 0.2 dex. Lastly, it could be the that we overpredict the various pressures due to photoionization and accretion by assuming spherical symmetry. In reality, the wind and accretion ram pressure may not necessarily be perfectly spherically symmetric, leading to a reduction in the overall confining pressure and an increase in the radius.

2.7.2 Evolutionary Classification

The Large Magellanic Cloud is home to one of the best-studied samples of GMCs in any galaxy. The LMC's disk-like geometry and face-on orientation offers little ambiguity in distance measurements, with the most accurate measurements giving $d_{\rm LMC} = 50.1$kpc (Alves, 2004). A large quantity of high-quality multiwavelength data has been obtained for the entire disk of the galaxy. In particular, the NANTEN ^{12}CO ($J = 1 \rightarrow 0$) surveys and high-resolution followup from the MAGMA ^{12}CO ($J = 1 \rightarrow 0$) survey (Hughes et al., 2010) have mapped the molecular content of the entire disk of the LMC and identified 272 clouds that together contain $5 \times 10^7 {\rm M}_\odot$ of molecular gas. When combined with multiwavelength archival observations of star formation indicators, these CO data constitute a snapshot in the evolution and star formation history of a population of GMCs.

Kawamura et al. (2009) used the NANTEN CO $J = (1 \rightarrow 0)$ data, along with complementary Hα photometry (Kennicutt & Hodge, 1986), radio continuum maps at 1.4, 4.8, and 8.6Ghz (Dickel et al., 2005; Hughes et al., 2007) and a map of young (< 10Myr) clusters extracted from UBV photometry (Bica et al., 1996) to investigate the ongoing star formation within GMCs in the LMC. These authors found a strong tendency for H II regions and young clusters to be spatially correlated with GMCs. Using this association, the GMCs in their sample were separated into three types. Type 1 GMCs are defined to be starless in the sense that they are not associated with detectable H II regions or young clusters, Type 2 GMCs are associated with H II regions, but not young clusters in the cluster catalog, and Type 3 GMCs are associated with both H II

regions and young clusters. 24% of the NANTEN sample were classified as Type 1, 50% as Type 2, and 26% as Type 3.

Assuming that GMCs and clusters are formed in steady state and assuming that young clusters not associated with GMCs are associated with GMCs that have dissipated, one can infer from the NANTEN population statistics that GMCs spend 6Myr in the Type 1 phase, 13Myr in the Type 2 phase, 7Myr in the Type 3 phase, and then dissipate within 3Myr. This accounting implies GMC lifetimes of approximately 20to30Myr. In support of the claim that the GMC classification scheme constitutes an evolutionary sequence, the authors note that among the resolved GMCs in the NANTEN survey, Type 3 GMCs are on average more massive, have larger turbulent line widths, and have larger radii. However, there is significant scatter in the Type 3 GMC sample and the mass and size evolution are well within their error bars.

In order to correct for extinction, which might obscure Hα emitting H II regions, radio continuum maps at three, well-separated frequencies were used to identify obscured H II regions via their flat spectral slopes. However, no H II regions were identified in the radio continuum data that were not present in the Hα maps, leading the authors to conclude that the Hα data was unaffected by obscuration. No similar analysis was performed to estimate obscuration of young star clusters. No attempt was made to correct for the varying sensitivities in the different radio maps, allowing for the possibility that some H II regions were detected at 1.4 Ghz but below the sensitivity limit at 4.8 and 8.6 Ghz.

There are several observational biases inherent in the GMC classification scheme

described above. The first is the probable existence of star clusters and H II regions located either behind or within giant molecular clouds from our viewpoint. High dust extinction along these sightlines would mask some young clusters from detection in the Bica et al. (1996) star cluster sample. This could lead to an overestimate of Type 2 GMCs relative to Type 3 GMCs. Another possible bias is the use of the Bica et al. (1996) star cluster catalog. Clusters in this catalog were targeted for UBV photometry based on brightness and association with emission nebulae. It is possible that some young clusters were missed in this catalog and no attempt is made by Kawamura et al. to correct for the completeness of the cluster catalog. This would also lead to an overestimate of Type 2 GMCs relative to Type 3 GMCs.

In order to make a quantitative comparison between our models and the evolutionary classification of Kawamura et al. (2009), we employ a few simple prescriptions to generate synthetic V band, Hα, and radio continuum photometry for the clusters and H II regions in our simulated clouds. First, we calculate the V-band luminosity of our simulated clusters using the synthetic photometry of Lejeune & Schaerer (2001). For $5\mathrm{M}_\odot \leq M_* \leq 15\mathrm{M}_\odot$, the photometry is based on the evolution tracks of Schaerer et al. (1993). For massive stars, $M_* \geq 15\mathrm{M}_\odot$, the synthetic photometry is based on the high mass-loss models of Meynet et al. (1994). For both sets of synthetic photometry, we assume $Z = 0.008$. Following Parravano et al. (2003), we approximate variations in L_V for these stars by only considering the main sequence evolution and taking $L_V = \langle L_V \rangle_{\mathrm{MS}}$, the mean luminosity on the main sequence. Since the stellar evolutionary tracks give the luminosity at a discrete set of masses, we interpolate by fitting a broken power law

between stellar masses with evolutionary tracks.

We calculate the Hα luminosity of our model H II regions via (McKee & Williams, 1997),

$$L_{\mathrm{H}\alpha} = 1.04 \times 10^{37} S_{49} \mathrm{ergs}^{-1}, \tag{2.70}$$

where S_{49} is the ionizing luminosity of the central star cluster in units of 10^{49}photons^{-1}. This is larger than the empirical relation by a factor of 1.37 to correct for the absorption of ionizing radiation by dust grains. Lastly, we find the radio continuum luminosity of our simulated H II regions via (Condon, 1992),

$$L_{\nu} = 1.6 \times 10^{23} S_{49} \left(\frac{1\mathrm{Ghz}}{\nu} \right) \mathrm{ergs}^{-1}\mathrm{Hz}^{-1} \tag{2.71}$$

We also account for the reduction in flux from GMCs that would be larger than the beam size used by Dickel et al. (2005) by performing a geometric correction and assuming that all H II regions are placed at the center of the model beam.

To assign our simulated GMCs an evolutionary classification, we extract the ionizing luminosity and V band luminosity of the brightest cluster in the GMC as a function of time. Using the ionizing flux, we calculate the expected Hα and radio continuum luminosity via Equation 2.70 and Equation 2.71 respectively. For the V band and $H\alpha$ luminosity, we correct for the foreground extinction, $A_V = 0.25$, towards the LMC (Schlegel et al., 1998), ignoring extinction internal to the LMC but external to the cloud under consideration. To identify the GMC as either Type 2 or Type 3, we use either an Hα luminosity cutoff or a radio continuum flux cutoff corresponding to

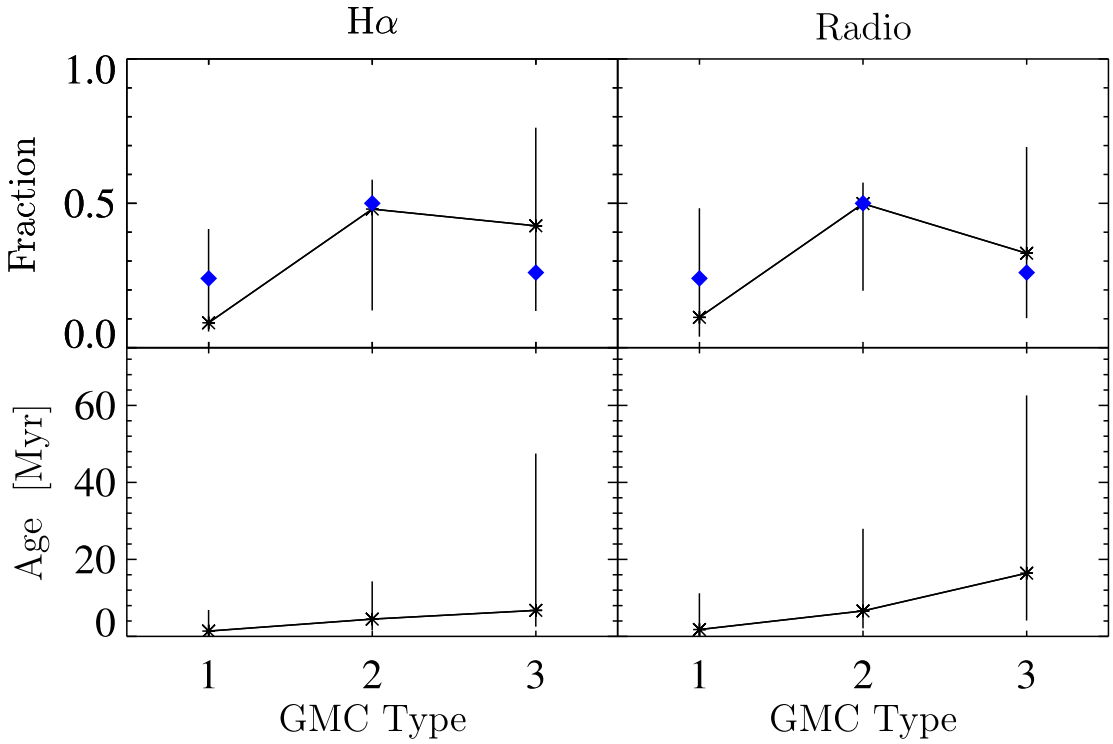

Figure 2.8: Fraction of GMC lifetime spent as a Type 1, 2, and 3 GMC as defined by Kawamura et al. (2009) (*diamonds, top row*), and average age of GMCs in each classification bin (*bottom row*). The asterisks indicate the median of the GMC type probability distribution functions generated using a Monte Carlo analysis described in the text. The error bars encompass the 10th to 90th percentile interval of the probability distribution functions.

the detection limits quoted by (Kawamura et al., 2009). For Hα, we say that an H II region is detected if $L_{H\alpha} \geq 10^{36}\mathrm{ergs}^{-1}$. For radio continuum, we say an H II region is detected if the radio flux at a distance of 50kpc would be greater than $0.7\mathrm{mJybeam}^{-1}$ for a beam size of $20''$ at 4.8GHz (Dickel et al., 2005). Finally, we say that a GMC is Type 3 if it meets the criteria just described for Hα or radio continuum as well as if $L_V \geq 1.66 \times 10^4 \mathrm{L}_\odot$, the completeness limit quoted by Bica et al. (1996) for the young cluster sample.

Since there are bound to be clusters that are located both behind and within clouds along our line of sight, we also correct the synthetic V-band and Hα photometry for extinction by the GMC. This is done by assuming that star clusters form at random locations within clouds. We calculate the optical depth to the star cluster via $\tau_\nu = \kappa_\nu \xi_\mu R_{\mathrm{cl}}$ where κ_ν is the mean dust opacity through the cloud, ξ_μ is the depth into the cloud in units of the cloud radius and μ is the angle between the normal to the surface of the cloud and the line of sight (Krumholz et al., 2008). For this purpose, we use a Milky Way extinction curve and assume an LMC dust-to-gas ratio whereby a column of $1\mathrm{gcm}^{-2}$ corresponds to $A_V = 107$. In the visual passbands we are concerned with here, the Milky Way and LMC extinction curves are nearly identical.

We have run a set of 2000 cloud models, 1000 each evolved using two different values of the ambient surface density, $\Sigma_{\mathrm{res}} = 8$ and $16\mathrm{M}_\odot\mathrm{pc}^{-2}$. All other parameters are as in Table 2.1. The resulting cloud models encompass the entire observed range in cloud masses reported by Fukui et al. (2008).

To directly compare to the observed distribution of GMC types we perform

simulated observations using a Monte Carlo scheme. Since the observations are inherently weighted by the GMC mass function, we first generate cloud masses by drawing from a powerlaw GMC mass spectrum with a slope of -1.6, a minimum mass of $5\times10^4 M_\odot$ and a maximum mass of $5 \times 10^6 M_\odot$ (Fukui & Kawamura, 2010). Once a mass is generated, we find all time steps where model clouds have masses within 0.1 dex of the randomly selected mass. Within this sample of time steps, we calculate f_1, f_2, and f_3, the fraction of Type 1, Type 2, and Type 3 GMCs, respectively. At the same time, we calculate t_1, t_2, and t_3 the average age of clouds in each GMC Type bin. We generate 10^4 Monte Carlo realizations, from which we construct probability distributions for f_1, f_2, f_3, t_1, t_2, and t_3.

The results of this comparison are presented in the top row of Figure 2.8. In the figure, the lines connect the median of the Monte Carlo probability distributions while the error bars encompass the 10th and 90th percentile. We are able to reproduce the observed distribution of Type 1, 2 and 3 GMCs as observed by Kawamura et al. (2009). In particular, using both detection limits, we find that the majority of clouds are detected as Type 2 GMCs, and relatively fewer clouds are detected as Type 1 and 3 GMCs. Interestingly, in the bottom panel of the figure, we find that, on average, the GMC classification scheme does constitute an age sequence in that Type 2 GMCs tend to be somewhat older than Type 1 clouds. Type 3 GMCs in turn tend to be older than Type 2 clouds. On the other hand, the spread in cloud ages within each bin is well within the error bars, indicating that the GMC type classification is not necessarily a strict evolutionary sequence: older clouds can be classified as Type 1 and younger

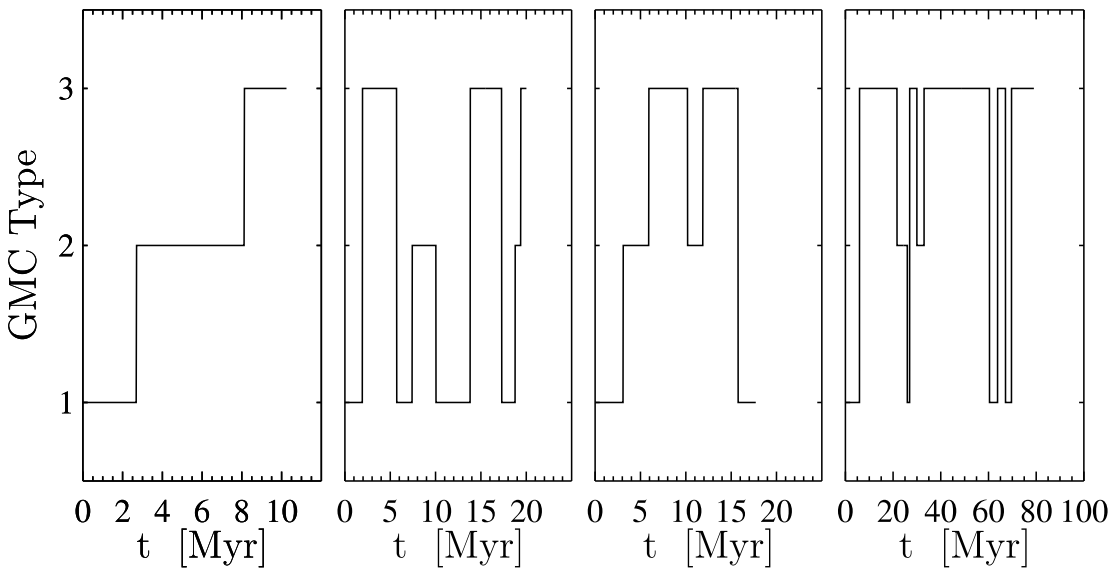

Figure 2.9: GMC classification as a function of time for a selection of model clouds.

clouds can be classified as Type 3.

This can be seen more clearly in Figure 2.9, where we plot the classification of a selection of GMCs as a function of time. We see that for some clouds, the classification scheme does represent an evolutionary sequence. In these runs, thw cloud starts as a Type 1 GMC, begins forming star clusters, evolves into a Type 2 GMC, and then forms massive OB association and becomes a Type 3 GMC. However, we also see that a cloud can quickly form a massive OB association and be classified as a Type 3 GMC early on and only later be classified as a Type 2 GMC. Alternatively, a cloud may happen to not form any massive clusters late in its evolution, causing a massive and old cloud to be identified as a Type 2 or 1 GMC late in its evolution. Finally, there are clouds which exhibit no discernible pattern in their histories, more or less randomly transitioning between GMC classifications throughout their lives. This may explain the presence of massive ($\sim 10^6 M_\odot$) Type 1 "young" GMCs in the samples of Kawamura et al. (2009)

and Hughes et al. (2010).

2.8 Caveats and Limitations

2.8.1 Implications of the Assumption of Homology

Assuming that clouds evolve homologously is the main limitation of our model. We make the assumption of homology to significantly simplify the equations governing the evolution of the cloud. Given the assumption of homology, our equations of motion follow rigorously from the local equation of momentum and energy conservation. A more complex cloud structure destroys the relative simplicity of the model and would require computationally expensive hydrodynamical simulations to model accretion in detail.

Homology constrains the cloud to always maintain the same shape and degree of central concentration. This is equivalent to setting time derivates of the structure constant, $a_{\rm I}$, to zero. This might be a problem if changes of the moment of inertia of clouds occur primarily by changing the shape of the cloud rather than through overall expansion or contraction. It might also be a problem if the accretion flow does not in reality differentially mix with the cloud. If the accretion flow is anisotropic or if it cannot fall to the central regions of the cloud before it mixes, the cloud may become less centrally condensed and we may overestimate the kinetic energy injection since material cannot fall to the bottom of the cloud potential well.

While we cannot resolve the dynamical effect of changes in the shape of the cloud, we can resolve changes in the size of the cloud. Given the observed Larson scaling

relations, we expect more massive clouds to be larger, implying that clouds must expand as they accrete mass. If clouds do form via gravitational instability, they must accrete significant mass. We do resolve this behavior in our models. We caution that our virial analysis most readily describes a relaxed system. We may be doing a poor job of resolving phenomena that occur on a timescale comparable to the crossing time.

2.8.2 Magnetic fields in the Atomic Envelope

One key assumption we made in deriving the global energy equation was that the atomic envelope contributes negligibly to the total magnetic energy associated with the cloud. That is, we did not include the magnetic field when calculating $\mathcal{E}_{\rm amb}$ in Equation 2.21. The motivation for this assumption is based on comparisons of observations of magnetic fields in dense molecular clumps, where it is possible to measure the magnetic field directly via the Zeeman effect in lines of OH and CN (Troland & Crutcher, 2008; Falgarone et al., 2008), to the magnetic fields in the atomic ISM, measured via the Zeeman effect in the 21 cm line of neutral Hydrogen (Heiles & Troland, 2005). These studies consistently find that the magnetic field strength is significantly elevated in the dense molecular gas. However, most of the volume of a GMC is occupied by diffuse molecular gas with low OH abundance — frustrating efforts to measure magnetic fields via observations of OH in emission. Thus, without direct observations of magnetic fields in the diffuse molecular gas, we cannot know whether the magnetic fields in the atomic envelope are weak or strong compared to the magnetic field strength in the bulk of a GMC. While preliminary observations by Troland et al. (2011, private communication) indicate that magnetic fields in the diffuse molecular component are somewhat stronger

than in the atomic envelope, this question has yet to be settled. It is possible that we underestimate the net magnetic energy due to the presence of the cloud.

Another possible problem with our treatment of magnetic fields is that we assume the mass-to-flux ratio remains constant throughout the evolution of the cloud. This is equivalent to assuming a fixed value for η_B. This assumption might be invalid if accreted material flows preferentially along magnetic field lines or if ambipolar diffusion can act act on timescales comparable to the cloud dynamical time. While measurements (Li et al., 2006a) and theoretical esimates (McKee & Ostriker, 2007) of the mass-to-flux ratio of molecular clouds find that clouds should be marginally supercritical, with mass-to-flux ratios of order unity, the time-evolution and cloud-to-cloud variation in mass-to-flux ratios are poorly constrained.

2.8.3 Validity of Larson's Laws

It has been suggested that the observed constancy of GMC surface densities is an artifact (see e.g. Kegel, 1989; Vázquez-Semadeni et al., 1997; Ballesteros-Paredes, 2006; Ballesteros-Paredes et al., 2011). Since the physical structure we assume for the clouds in our model implicitly assumes that the Larson relations are valid, this may imply that our models do not correspond well to real GMCs.

The argument that the Larson laws are a product of a selection effect usually proceeds as follows. If one looks for overdensities of a particular size in a simulation of the turbulent ISM, one will find that the selected clouds have a wide distribution of masses, implying a large spread in cloud-to-cloud surface density. Since observers detect clouds using CO as a tracer and at low surface density the CO abundance is not

high enough to be detectable in emission, observers will never find low surface density clouds. This implies that at a fixed radius, real clouds should have more variation in mass than a naive interpretation of the CO observations would suggest.

This argument misses two key aspects of the observed properties of GMCs. The first is that it cannot explain the lack of clouds at *high* gas surface densities. For the same reason that we should not be able to see diffuse clouds, we should very easily be able to see compact, high surface density CO clouds. The fact that these clouds don't exist implies something important about molecular cloud structure. The second argument is that the lack of low surface density clouds does not imply that molecular clouds can exist at all surface densities but merely that the molecular clouds dissociate once they become optically thin to the ambient ultraviolet radiation field. While diffuse atomic clouds certainly exist, these clouds do not form stars (Krumholz et al., 2011).

Since high surface density GMCs are not observed in the local universe and low surface density clouds are not molecular and thus not GMCs by definition, the observed lack of variation in GMC surface densities must be a real property of the clouds. This has been confirmed with very detailed dust extinction measurements of nearby star forming clouds, where an exquisitely tight mass-radius relation is observed (Lombardi et al., 2010) and in extragalactic studies where little variation is seen when comparing the mass-radius relation from galaxy to galaxy (Bolatto et al., 2008). Taken together, the evidence seems to imply that the Larson relations are a property of the structure of GMCs and are not due to a selection effect.

2.9 Conclusions

In this chapter, we have presented semianalytic dynamical models for the evolution of giant molecular clouds undergoing both mass accretion and star formation. These models are able to capture the evolution of individual GMCs from their growth and the onset of massive star formation, until their dispersal via an energetic H II region or through the combined action of accretion and star formation. We are able for the first time to synthesize galactic populations of GMCs whose properties correspond closely to the observed properties of GMCs in the Milky Way and nearby external galaxies. We have shown that clouds in low surface density environments generally disperse within a few crossing times, before they can accrete all of the gas in their reservoir. At the same time, clouds in high surface density environments do accrete all of the gas in their reservoirs and tend to be larger and more massive. We have also shown that mass accretion can contribute a significant fraction of the total energy available for turbulent driving. Lastly, we generate synthetic cluster observations and compare against the evolutionary classification scheme of Kawamura et al. (2009), finding good agreement when we correct for selection effects and systematic biases inherent in the observations. We conclude that, on average, the evolutionary classification scheme corresponds to an age sequence but is not a good predictor for the evolutionary state of isolated clouds.

Part II

Mass transport and Turbulence in Gravitationally Unstable Disk Galaxies

Chapter 3

The Case of No Star Formation Feedback

3.1 Introduction

In this chapter we make use of simulations of the gas, stars, and dark matter in idealized isolated models of star forming disk galaxies. We focus on the spatial and mass scale similar to the Milky Way and study three different disks with varying gas fractions. We expand on previous work in a number of ways,

- Using our high numerical resolution — $\Delta x \sim 20$ pc at the maximum refinement level, corresponding to a threshold density for star formation $n_{\rm thresh} \sim 50$ cm^{-3} — we are able to comfortably resolve the global properties of star forming regions in our disk models (although we do not resolve the internal properties of star forming clouds), allowing us to resolve an ISM with multiply distinct phases.

- Our simulations are run for several galactic dynamical times. This long time baseline allows the models to reach statistical equilibrium. As we will show, the onset of violent gravitational instability in our disk models is accompanied by substantial transient ringing behavior characteristic of the smooth unstructured initial conditions.

- We perform a detailed modeling of the Toomre Q parameter, taking into account contributions of the gas and stars, including both the thermal and kinetic gas pressure, and accounting for the nonzero thickness of the gas and stellar disks.

- We measure the radial variation in the radial mass flux using grid of test cylindrical surfaces, nested every 40 pc in radius for each of our simulation outputs. This allows us to clearly resolve in space and time the variation in the radial mass flux, allowing us to track the flow of matter in the disk and measure a mean flow of matter through the disk.

- The initial conditions data, full simulation code, and analysis code are publicly available.

Our simulations are quite similar to those of Agertz et al. (2015). There simulations are based on nearly identical initial conditions but were run with a factor of two higher spatial resolution than we use. On the other hand, we simulate galaxies over much longer baselines (600 Myr vs. 140 Myr), which is essential to allow the gravitational instability to settle into steady state and thereby to allow an accurate measurement of the rates of the typical mass transport rate due to gravitational instability. Agertz et al.

(2015) do not consider the issue of transport in their study.

The plan for the remainder of this chapter is as follows. In section 3.2 we describe the code, subgrid physics models, and initial conditions. In section 3.4, we describe in general terms the time evolution of our simulations, particularly with respect to the dynamical evolution of the gravitational instability process. In section 3.5 we quantitatively measure the effect of the gravitational instability via the time evolution of the Q parameter, as the radial mass flux, measure the mean mass flux rate through our simulated disks, and discuss the velocity structure of the gaseous disk. Finally in section 3.6 we review our findings and discuss implications for future work.

3.2 Simulations

This work makes use of three simulations of isolated disk galaxies. All simulations were performed using the Enzo AMR hydrodynamics code (The Enzo Collaboration et al., 2014). These simulations include self-gravity, cooling, PPM hydrodynamics, and N-body dynamics. The properties of the simulations are summarized in Table 3.1.

3.2.1 Initial Conditions

The initial conditions were generated for the AGORA project (Kim et al., 2014) using the `makegalaxy` code (Springel et al., 2005). Briefly, `makegalaxy` transforms an input halo mass (M_{200}), disk mass (M_D), gas fraction (f_g), halo spin parameter (λ), and halo concentration parameter (f_c) into particle initial conditions. These input parameters uniquely set the rotation curve, $V_C(R)$, and radial scale length, h_R via the

analytic theory of Mo et al. (1998).

M_{200}	$1.1 \times 10^{12}\ M_\odot$	V_{200}	150 km s^{-1}
R_{200}	206 kpc	f_c	10
λ	0.04	M_D	$4.3 \times 10^{10}\ M_\odot$
h_R	3.4 kpc	h_z	0.34 kpc
M_B	$4.3 \times 10^{10}\ M_\odot$	Δx	20 pc
$n_{\rm thresh}$	50 cm^{-3}	N_H	10^7
N_D	10^7	N_B	1.25×10^6
m_H	$1.3 \times 10^5\ M_\odot$	m_D	$3.4 \times 10^3\ M_\odot$
m_B	$3.4 \times 10^3\ M_\odot$		

Table 3.1: Resolution and structural parameters for the isolated disk galaxy models. All three simulations are initialized with the same halo, disk, bulge, and resolution parameters.

The dark matter and stars are represented in the galaxy model using N-body particles and are initialized by stochastically drawing from analytic distribution functions. The dark matter positions are initialized to follow a Hernquist (1990) distribution, which closely matches the more commonly used Navarro, Frenk, & White (1996) fitting formula, but is more analytically tractable. The star particle positions are initialized following

$$\rho_*(R,z) = \frac{M_*}{4\pi h_z h_R^2} \mathrm{sech}^2\left(\frac{z}{2h_z}\right) \exp\left(-\frac{R}{h}\right) \tag{3.1}$$

where $M_* = (1 - f_g)M_D$ is the mass of the stellar disk, h_z is the vertical scale height,

z is the vertical coordinate, and $R = \sqrt{x^2 + y^2}$ is the cylindrical radial coordinate. We consider gas fractions $f_g = 0.1$, 0.2, and 0.4, which we refer to as the low gas fraction (LGF), fiducial, and high gas fraction (HGF) runs, respectively (Table 3.1). Once the particle positions are computed, the velocities are populated using a distribution function that depends only on the local orbital energy E and vertical component of the angular momentum L_z. The velocity distribution function is assumed to be axissymetric, making it strraightforward to locally solve the Jeans equation making use of the known density distribution from above (see Springel et al. (2005) for more details).

In addition to the stellar disk component, we also include a bulge of mass M_B. The bulge is initialized following a Hernquist profile:

$$\rho_B(r) = \frac{M_B}{2\pi} \frac{b}{r(r + h_B)^3} \tag{3.2}$$

where h_b is a free parameter. The bulge-to-total mass ratio, B/T, is 0.1 in all three runs.

Since `makegalaxy` produces initial conditions formatted for the `gadget` smoothed particle hydroynamics (SPH) code, special care must be taken to initialize the gas onto Enzo's AMR grid structure. Rather than interpolating from the initial conditions for the SPH particles, we instead initialize the gas density following an analytic density profile:

$$\rho(R, z) = \frac{M_G}{4\pi h_R^2 h_z} \exp\left(\frac{-r}{h_R}\right) \exp\left(\frac{|z|}{h_z}\right) \tag{3.3}$$

where $M_G = f_g M_D$ is the mass of the gaseous disk. The gas velocities are initially

axisymmetric, with the radial profile set according to the circular velocity curve written out by `makegalaxy`.

This departs somewhat from the procedure used by `makegalaxy` to generate SPH initial conditions, where the gas density distribution is assumed to be exponential in the radial direction but the vertical extent is determined via an interative relaxation process to ensure the gas disk is initially in equilibrium. This relaxation process assumes that the gas pressure is moderated by a subgrid effective equation of state model, which we do not employ in this study. In practice, the gas in our simulations initially experiences a phase of violent collapse and relaxes into a quasi-equilbrium state after the gravitational instability has fully developed. This means the precise state of the gas in the initial conditions is not terribly important — the simulation "forgets" the gas initial conditions. Furthermore, this choice also allows us to make an apples-to-apples comparison with future isolated galaxy simulations that make use of the public AGORA isolated galaxy initial conditions.

3.2.2 N-body dynamics, Hydrodynamics

Rather than making use of an analytic dark matter and stellar potential (see, e.g., Dobbs et al., 2006; Tasker & Tan, 2009), we employ a live dark matter halo and stellar disk. This allows us to follow the active response of the stars and dark matter to the collapse of the gaseous disk. The particle dynamics are implemented in Enzo using a standard particle-mesh scheme (Hockney & Eastwood, 1988). Particle positions and velocities are updated according to the local gravitational acceleration using a drift-kick-drift scheme.

Hydrodynamics are captured using the piecewise parabolic method (PPM) (Colella & Woodward, 1984). PPM hydrodynamics allows us to accurately capture the strong shock in a few computational zones while also maintaining second-order spatial accuracy. While the PPM method is formally second-order accurate in space and time, Enzo's adaptive timestepping scheme is only first-order accurate, so these calcualations are only first order accurate in time. In addition, after experiencing intermittent instability using second-order interpolation, we opted to degrade to first-order interpolation at AMR level boundaries. This means that we are formally first-order accurate in space, although these inaccuracies should only show up at level boundaries.

Since the $\sim$200 km s^{-1} circular velocity of the galaxy necessitates strongly supersonic flows in the galactic disk, we make use of the dual energy formalism implemented in the Enzo code (Bryan et al., 1995). In standard PPM hydrodynamics, the internal energy is not tracked — instead it is derived from the total energy and velocity. When the kinetic energy is much larger than the internal energy, this can lead to spurious temperature fluctuations due to floating point round-off error. To avoid this, Enzo tracks a separate internal energy field that in effect provides extended precision to the total energy field. This allows us to safely resolve the thermal physics of the gas in a global simulation of a disk galaxy without worrying about spurious temperature fluctuations due to advection errors.

3.2.3 Initial Grid Structure and Refinement Criteria

Our simulations make full use of the AMR capabilities of the Enzo code. Our refinement strategy is primarily to focus computational effort on the highest refine-

ment level, while still adequately resolving the dark matter halo so our estimate of the gravitational potential in the neighborhood of the galactic disk is accurate. Since the dark matter halo is spatially extended compared to the disk, with the furthest dark matter particles living 500 kpc away from the center of the galaxy, this necessitates a hierarchically nested AMR structure.

To fully encompass the dark matter halo, we employ a cubic simulation box with a width of 1.3 Mpc, and resolve the root grid with 64^3 cells. In addition to the static root grid, we impose 5 additional levels of statically refined regions, enclosing volumes that are successively smaller by a factor of 8.

In addition to the static refinement, we allow for an additional five levels of adaptive refinement. To keep the particles properly resolved at all times, we refine a cell if the total mass in particles within the cell exceeds 1.7×10^6 $M_\odot$, or approximately 10 halo particles. This choice produces nested grid hierarchies in the region of the simulation dominated by the dark matter halo where the grid hierarchy is determined adaptively.

To keep the gaseous disk resolved at all times, we refine a cell if the total mass in gas within the cell exceeds 2.2×10^4 $M_\odot$. Lastly, to avoid artificial fragmentation, we ensure the Jeans length, $\lambda_J = \sqrt{(\pi c_s^2)/(G\rho)}$ is locally resolved at all times by at least 32 cells, comfortably satisfying the Truelove et al. (1998) criterion. To keep the Jeans length resolved after collapse has reached the maximum refinement level, we employ a pressure floor such that the Jeans length is resolved by at least 4 cells on the maximum refinement level. To avoid contaminating the hydrodynamics in situations where we

can use more resolution, the pressure floor is only employed for cells on the maximum refinement level. We have modified Enzo to include a pressure floor implemented as a source of "extra" pressure above the thermal pressure.

While the particle refinement criteria we use are not particularly stringent for the star particles, in practice the stellar disk is resolved to the same level as the gaseous disk. Except for an initial period when the gas disk collapses, we find that the stellar disk is resolved at the maximum grid resolution at all times due to the refinement criteria chosen for the gas. As noted in The Enzo Collaboration et al. (2014), this implies an effective gravitational softening length of two cell spacings, or 40 pc for the stars.

3.2.4 Star Formation

Since the gaseous disks in our simulations are unstable to fragmentation and collapse, it is necessary to include a subgrid model that coverts dense, collapsing gas into newly formed star particles. Rather than using the built-in "standard" star formation prescription in the Enzo code (The Enzo Collaboration et al., 2014; Cen & Ostriker, 1992), which is tuned for lower-resolution cosmological simulations, we make use of an new star formation prescription. To ease comparison with future papers using the AGORA initial conditions, the prescription is based on the suggested star formation model for the AGORA project (Kim et al., 2014).

Briefly, the model assumes that the star formation rate density in any cell is a

function only of the gas density in that cell, according to the following formula:

$$\frac{d\rho_*}{dt} = \begin{cases} f_* \frac{\rho}{t_{\rm ff}} & : \rho > \rho_{\rm thresh} \\ 0 & : \rho \leq \rho_{\rm thresh} \end{cases} \tag{3.4}$$

where f_* is the star formation efficiency, $t_{\rm ff} = \sqrt{3\pi/32G\rho}$ is the local dynamical time, and $\rho_{\rm thresh}$ is the threshold density for star formation. In all of our simulations, we use $f_* = 1\%$, in accordance with the observed low star formation efficiency universally observed in star forming regions at a range of density and size scales (Krumholz & Tan, 2007b; Krumholz et al., 2012).

The star formation threshold is chosen such that the local Jeans length needs to be resolved by fewer than 4 cells on the maximum refinement level, assuming a temperature floor of 100 K, approximately the minimum temperature we see in our simulations. Since we only barely resolve the typical densities for the formation of molecular gas, we do not employ a subgrid model to track the molecular gas fraction, instead assuming that gas above the threshold density is fully molecular. This follows Guedes et al. (2011), who found that the precise value chosen for $\rho_{\rm thresh}$ was not important, so long as it is high enough to correctly resolve that star formation occurs in dense clumps of gas rather than in the bulk of the ISM.

Practically speaking, Equation 3.4 cannot be solved by spawning star particles at each timestep. Given a typical timestep of 1000 yr, and assuming a cell containing gas at the threshold density, we expect to be spawning star particles with masses of only .01 $M_\odot$. Worse, since this will happen in every star forming cell, on every timestep, the

cost of the simulation will very quickly become dominated by bookkeeping for millions of these tiny star particles.

Rather than spawning star particles in every cell that exceeds the density threshold, we instead impose a minimum star particle mass, and form stars stochastically. In our scheme, a cell will form a star particle of mass $m_{\rm sf}$ with probability

$$P_* = \begin{cases} f_* \frac{\rho \Delta x^3}{m_{\rm sf}} \frac{dt}{t_{\rm ff}} & : \rho > \rho_{\rm thresh} \\ 0 & : \rho \leq \rho_{\rm thresh} \end{cases} \tag{3.5}$$

where dt is the simulation timestep on the maximum refinement level.

In Figure 3.1, we compare the star formation rate implied by the ages of star particles present at the end of each simulation with the with the expected star formation rate, calculated using Equation 3.4 measured at 25 Myr intervals. We see that there is good agreement between the measured and predicted star formation rate, with a maximum deviation of $\sim$7 %. The implementation of this star formation algorithm has been made publicly available and will included in the upcoming Enzo 2.5 release.

3.2.5 Heating and Cooling

To model the thermal physics of the gas in our simulations, we make use of the `Grackle` cooling library[1] (The Enzo Collaboration et al., 2014; Kim et al., 2014). The `Grackle` cooling and heating routines were adapted from the chemical and thermal physics implementation included in the `Enzo` code. Relative to Enzo's implementation of thermal physics, `Grackle` adds novel capabilities that we make use of this study. In

[1] https://grackle.readthedocs.org

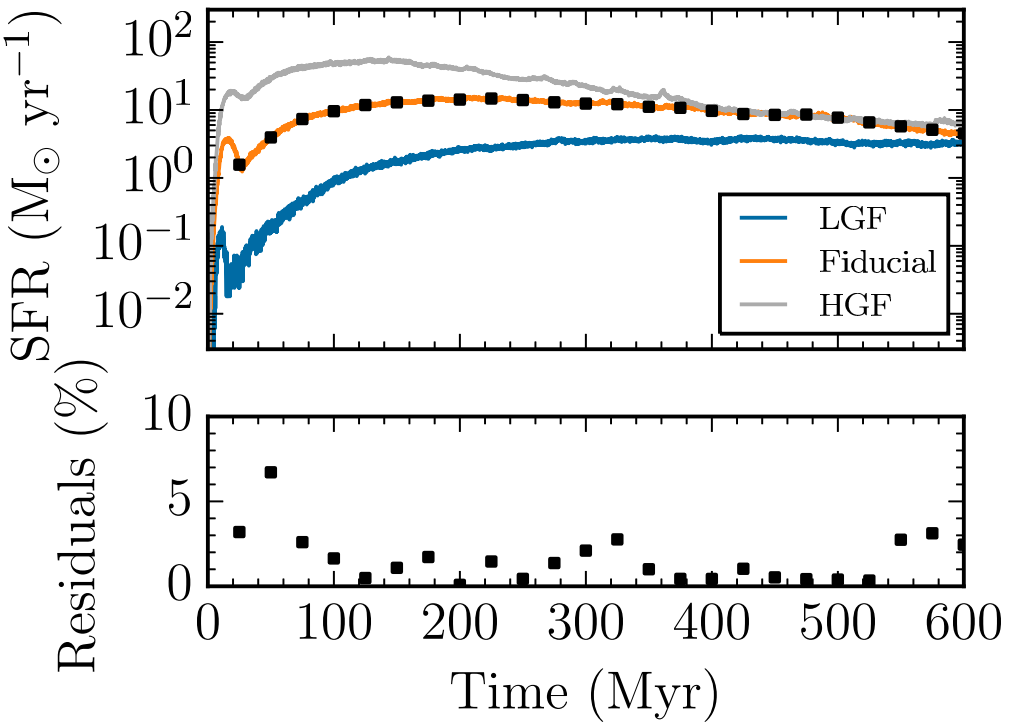

Figure 3.1: The observed (solid lines) star formation rate as a function of time for all three simulations. The black squares were calculated by directly measuring the expected star formation rate in the fiducial simulation according to Equation 3.4. The blue line was calculated by binning the star particles that are dynamically formed in the simulation by their formation times. The bottom panel is the residual between the black points and orange line in the top panel. We find good agreement between the predicted and measured star formation rate.

addition, this choice eases comparison with future simulations performed in other codes as well as simulations performed for the AGORA comparison.

`Grackle` includes a primordial cooling routine based on tabulated cooling rates as a function of density and temperature, avoiding the need to evolve separate fields for each hydrogen and helium ionization state. In addition to cooling by primordial species, we also include cooling due to metal line emission. These cooling rates are inferred from tabulated rates output by the `CLOUDY` code.

To properly model the thermal physics in a Milky Way-like ISM, we include a prescription for heating due to electrons released from dust grains by the photoelectric effect. This is implemented as a constant heating rate of 8.5×10^{-26} erg cm^{-3} s^{-1} applied uniformly throughout the simulation box (Tasker, 2011). This rate is chosen to match the expected heating rate assuming a UV background consistent with the solar neighborhood value (Draine, 2011).

3.3 Analysis

In order to analyze our simulations, we construct an extensive post-processing pipeline using a combination of the `yt` toolkit (Turk et al., 2011) and a set of custom python analysis scripts that we have made publicly available on Bitbucket[2]. Details of the analysis pipeline, and how we reconstruct various quantities of interest from the raw simulation outputs, are described below.

[2] https://bitbucket.org/ngoldbaum/galaxy_analysis

3.3.1 Grid Slabs

Rather than analyzing the AMR data structures directly, we instead perform the bulk of our analysis using data interpolated onto 20 pc resolution grids encompassing the galactic disk out to a radius of 20 kpc and to a height of 1.25 kpc above and below the disk. This choice significantly eases the implementation of the various analysis tasks we want to perform on the data without introducing a significant amount of error. Since the disk is very thin, a vertical extent of only 1.25 kpc comfortably encloses the gas and stellar disk at all times.

To interpolate the gas data onto a uniform resolution grid, we make use of the smoothed covering grid object in `yt`. This operation uses cascading trilinear interpolation to represent an AMR dataset at a uniform resolution. The fields representing gas density, the velocity vector components, and the gas thermal energy were extracted from the raw simulation outputs. Since the gravitational potential is not normally written to disk, we made use of the `-g` command-line option of the `Enzo` code to solve the Poisson equation during post-processing.

So that we can apply the same analysis tasks we use for gas fields defined on Enzo's AMR mesh to N-body star particles in our datasets, we opt to analyze stellar fields by depositing the star particle data onto the uniform resolution grids slabs. In all cases, we use cloud-in-cell interpolation onto grids with the same shape and resolution as those used for the gas data. Our choice of uniform resolution slabs leads to issues with data sparseness in the outskirts of our simulated galaxies but is a good match for the density of particle data within a radius of 10 kpc.

3.3.2 Rotation Curve and Epicyclic Frequency

Because our simulations use a live stellar and dark matter halo, the rotation curve of our galaxy is not fixed, and must instead be computed self-consistently from the simulation outputs. Following Binney & Tremaine (2008) and Shu (1992), we note that for an axisymmetric system with gravitational potential field $\Phi(R, z)$, we can define the circular frequency

$$\Omega^2(R) = \frac{1}{R}\left(\frac{\partial \Phi}{\partial R}\right)_{(R,0)}, \tag{3.6}$$

and epicyclic frequency

$$\kappa^2(R) = \frac{2\Omega}{R}\left(2R\Omega + R^2\frac{d\Omega}{dR}\right). \tag{3.7}$$

This implicitly assumes the disk is thin so we can infer the circular velocity curve by only considering the gravitational potential in the midplane; this is a good assumption for all of our simulations, since our disk is very thin.

To measure the rotation frequency, we extract the gravitational potential in a slice at the midplane of the galaxy, and evaluate the partial derivative of the potential with respect to x and y coordinates using a centered finite difference of the gravitational potential data. We then form a 2D array of the gradient with respect to the cylindrical R coordinate out of the images of the x and y gradients. This results in a local estimate of the rotation frequency based on the local radial gradient in the gravitational potential. To average over local departures from axis-symmetry, we create our final estimate of the rotation frequency by fitting a spline interpolator to a binned version of our local estimate of the circular frequency as a function of radius. This produces a binned 20 pc

resolution estimate of the rotation frequency as a function of cylindrical radius. Finally, we form the circular velocity via

$$v_c = R\Omega. \tag{3.8}$$

Here Ω refers to the binned azimuthally averaged estimate.

3.3.3 Surface Density

Several different quantities we are concerned with are defined in terms of the projection of our simulation data. For a 3D density field $\rho(x, y, z)$ we can define the surface density of the fluid

$$\Sigma(x, y) = \int_{-\infty}^{\infty} \rho \, dz. \tag{3.9}$$

Here ρ might represent the mass density of gas or stars, which we denote as $\rho_{\rm gas}$ and ρ_* below.

Discretizing ρ into a uniform resolution 3D array, which we denote as ρ_{ijk}, the continuous definition of the surface density reduces to

$$\Sigma_{ij} = \sum_{k=0}^{N_z} \rho_{ijk} \Delta z \tag{3.10}$$

where Δz is the cell spacing the vertical direction. Since our grid slabs only include data within 1.25 kpc of the disk midplane, we are implicitly assuming that gas well of the midplane does not contribute significantly to the surface density.

We introduce the notation, $\langle q \rangle_z$, to represent the discrete mass-weighted projection operator. The result is a uniform resolution 2D array, where the i, j resolution

element can be found by computing,

$$\langle q \rangle_{z,ij} = \frac{1}{\Sigma} \sum_{k=0}^{N_z} \rho_{ijk} q_{ijk} \Delta z. \tag{3.11}$$

This notation allows us to write several of the definitions below in a compact form.

3.3.4 Velocity Dispersion

Since turbulent motions are a significant component of the energy budget in the ISM, we would like to directly measure the turbulent kinetic energy in our simulations. Since our simulations are a discretized representation of a continuous underlying system, we can only estimate the velocity dispersion by comparing velocity values in cells contained within a moving window several cells across. So that variations in the rotation curve over the extent of the window do not tend to inflate the measured velocity dispersions, we define the velocity of streaming motions

$$\delta \mathbf{v} = \mathbf{v} - v_c(R)\hat{\phi}. \tag{3.12}$$

To simplify notation in our definition of the velocity dispersion, we define the discrete operator

$$C_{ijk}(x) = \sum_{k'=k-2}^{k+2} \sum_{j'=j-2}^{j+2} \sum_{i'=i-2}^{i+2} x_{i'j'k'}, \tag{3.13}$$

where x is a field defined on the uniform resolution mesh. This is equivalent to a discrete convolution of x using a cubical top-hat kernel function. Using this notation, our estimate of the velocity dispersion due to motions in the x coordinate, δv_x, can be

written

$$\sigma_{x,ijk} = \frac{\sqrt{C(\rho)C(\rho\,\delta {v_x}^2) - C(\rho\,\delta v_x)^2}}{C(\rho)}, \tag{3.14}$$

where δv_x is the x component of the streaming velocity vector $\delta\mathbf{v}$. The expressions for the y and z velocity dispersions are analogous.

We use the same definition for stellar velocity dispersions, but rather than calculating the dispersion on a cell-by-cell basis, we instead iterate over particles, performing a running dispersion calculation by depositing particle densities and velocities into accumulating arrays. This uses more memory, but is substantially faster for the particle counts in our simulations.

Finally, we calculate the projected velocity dispersions by performing a weighted projection of the turbulent kinetic energy density:

$$\sigma_v = \sqrt{\langle \sigma_x^2 + \sigma_y^2 + \sigma_z^2 \rangle_z}. \tag{3.15}$$

In addition, to estimate the relative contribution of in-plane and out-of-plane turbulent motions, we separately define the in-plane velocity dispersion

$$\sigma_{v,d} = \sqrt{\langle \sigma_x^2 + \sigma_y^2 \rangle_z}, \tag{3.16}$$

and the out-of-plane velocity dispersion

$$\sigma_{v,z} = \sqrt{\langle \sigma_z^2 \rangle_z}. \tag{3.17}$$

3.3.5 Effective Sound Speed

We can define an effective sound speed that takes into account both gas pressure and turbulent pressure,

$$c_{\rm eff} = \sqrt{\sigma_v^2 + c_s^2} \tag{3.18}$$

For collisionless fluids, $c_{\rm eff} = \sigma_v$, but for the gaseous component we must calculate the sound speed. In practice, we do this in terms of the weighted projection of the thermal energy density e,

$$c_s = \sqrt{\gamma(\gamma - 1)\langle e \rangle_z} \tag{3.19}$$

where $\gamma = 5/3$ is the adiabatic index.

3.3.6 Toomre Q

Using the derived data we introduced above, we can compute the Toomre Q parameter for both the gas,

$$Q_{\rm gas} = \frac{c_{\rm eff}\kappa}{\pi G \Sigma} \tag{3.20}$$

and stars,

$$Q_* = \frac{\sigma_v \kappa}{3.36 G \Sigma}. \tag{3.21}$$

We also attempt to estimate the degree of gravitational instability due to both the gas and stars. We make use of the formula derived by Romeo & Wiegert (2011) that takes into account the separate contribution of the gas and stars as well as their

finite thickness. In this formalism,

$$\frac{1}{Q_{\rm total}} = \begin{cases} \frac{W}{T_* Q_*} + \frac{1}{T_{\rm gas} Q_{\rm gas}} & : T_* Q_* \geq T_{\rm gas} Q_{\rm gas} \\ \frac{1}{T_* Q_*} + \frac{W}{T_{\rm gas} Q_{\rm gas}} & : T_* Q_* < T_{\rm gas} Q_{\rm gas} \end{cases} \tag{3.22}$$

where $T = 0.8 + 0.7\sigma_z/\sigma_d$, and $W = 2\sigma_* \sigma_{\rm gas}/(\sigma_*^2 + \sigma_{\rm gas}^2)$.

3.3.7 Scale Height

For a fluid with local mass density ρ, we define the scale height h such that

$$\int_0^h \rho \, dz = \left(1.0 - e^{-1}\right) \int_0^\infty \rho \, dz \tag{3.23}$$

Here the z coordinate is perpendicular to the disk and centered on the disk midplane. Since the fluid distribution is not necessarily symmetric in z, the z coordinate of the midplane is therefore not constant, and the scale height above and below the midplane might not necessarily be equal. In practice, we take the true scale height h to be the arithmetic mean of the scale heights measured above and below the midplane.

In practice, we generate maps of of the scale height be individually processing z-aligned pencil stacks of cells. Gas mass is summed up along the z direction until the cells that contain the location along the stack of cells where the running surface density along the column of cells to the surface density equals one of $(2e)^{-1}$, $1/2$, or $1.0-(2e)^{-1}$. For each location, we linearly interpolate in z to estimate the coordinate within each cell where the running sum exceeds the critical value. Finally, we calculate a single scale height estimate by averaging the "top" and "bottom" estimates.

3.3.8 Radial Mass Flux

To quantitatively analyze the radial transport of mass in our simulation galaxies, we focus on the flux of mass through cylindrical test volumes. For a cylindrical test volume V of radius R, the flux of mass across the surface of the cylinder is

$$\dot{M} = R \int_0^{2\pi} \int_{-\infty}^{\infty} \rho v_r \, dz \, d\theta. \tag{3.24}$$

In practice, we calculate this quantity using a discrete approximation based on our interpolated data defined on uniform resolution grid slabs. Here we can take advantage of the cylindrical symmetry of the problem to substantially reduce the computational cost of this calculation. If we consider a single x-y slice through our grid slab, it is a straightforward geometric problem to find the set of cells in this slice that the cylindrical test volume intersects with.

If we define a one dimensional index that $l \in [0, N]$ where N is the total number of cells in the x-y plane that intersect with the circular test region, we can approximate

$$\dot{M} = \sum_{k=0}^{k_{\max}} \sum_{l=0}^{N} \rho_{lk} v_{r,lk} \Delta\theta_l \Delta z. \tag{3.25}$$

Here l maps to a set of unique coordinates in the 2D slice of the 3D grid slab and k indexes along the z direction in the grid slab. One can think of l as a map to a single pair of i, j indices for the x and y rows in our grid slice. The problem of calculating the radial mass flux reduces to calculating the angles $\Delta\theta_l$. Since we ignore gas well off the midplane, this implicitly assumes that the mass transport at large heights above and

below the midplane is small.

Doing this at many different radii allows up to map how the radial mass flux varies with galactocentric radius. In practice, we choose a set of 1000 nested test cylinders, binned evenly in radius with a spacing of 40 pc.

3.3.9 Time Averaging

We are interested in the time-average behavior of azimuthally averaged quantities, both to compare to 1D models of galaxy formation and also to capture the large-scale behavior of our simulations over long periods of time. As we show in the main text, the internal structure of our simulated galaxies is initially dominated by transient disturbances. After several galactic rotation periods, the disk models settle down, reach a quasi-equilibrium state in which the global structure is more or less static. Since the galactic rotation period is an increasing function of radius, the places where we expect the disk to be settled corresponds to a wedge shaped region of radius-time phase space.

We define the time-averaging operator,

$$\langle x(r,t)\rangle_t = \frac{1}{t_{\max} - (t_0 + ar)} \int_0^{t_{\max}} y(r,t)dt \tag{3.26}$$

where,

$$y(r,t) = \begin{cases} x(r,t) & : t - t_0 \geq ar \\ 0 & : t - t_0 < ar \end{cases} \tag{3.27}$$

where $x(r,t)$ is a measurement of the time evolution of a mass flux or an azimuthally averaged quantity, $t_{\max}$ is the simulation time at the end of the simulation (600 Myr for

all three simulations presented here) and a and t_0 are constants that define the shape of the "averaging wedge". In practice we determine these constants "by eye" based on inspection of the simulation results.

3.4 Qualitative Outcome

We present snapshots of the fiducial simulation at four times in Figure 3.2 and snapshots of all three simulations at a fixed time in Figure 3.3. Each figure displays the gas and stellar surface density and effective sound speed as well as the combined Toomre Q parameter.

The dynamics of all three simulations are similar. The initially smooth gaseous disk quickly cools from the initial temperature of 10^4 K to 200–300 K. The initially thermally supported disk proceeds to collapse in a radially expanding manner over the course of the next 20–50 Myr. Denser regions in the center of the disk collapse first, followed by less dense regions further out in the disk, with the precise collapse time determined by the initial gas surface density at any given radius. Once the gas has collapsed in the vertical direction, the disk remains very thin, with the bulk of the gas only one or two cells (20–40 pc) away from the midplane. For this reason, our disks are not resolved in the vertical direction.

Once the gas has collapsed vertically, a combination of shear and self-gravity lead the gas to collect into filaments which in turn collapse into isolated gravitationally bound clouds. Since these simulations do not include feedback, these clouds survive more or less permanently, only disappearing if they exhaust their gas supply by converting gas

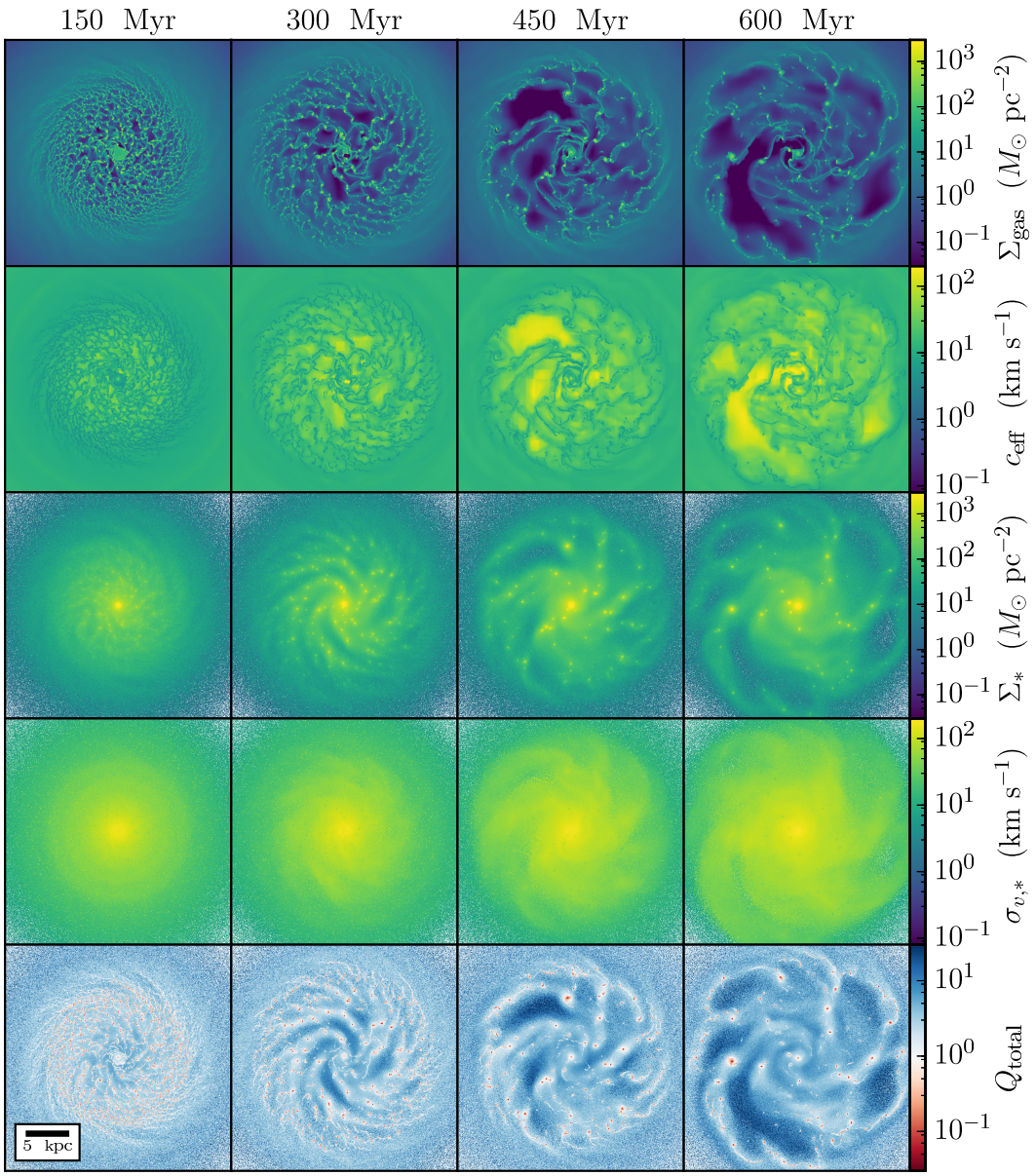

Figure 3.2: The time evolution of the gas and stars in the fiducial simulation. The quantities shown are, from top to bottom, gas surface density, effective sound speed of the gas (including thermal and turbulent contributions), stellar surface density, stellar velocity dispersion, and total (gas plus stars) Toomre Q; formal definitions for all quantities are given in section 3.3. The simulation time for each column is indicated at top and the spatial scale is indicated relative to the scale bar at the bottom right. Each panel displays a 25 kpc region centered on the galaxy.

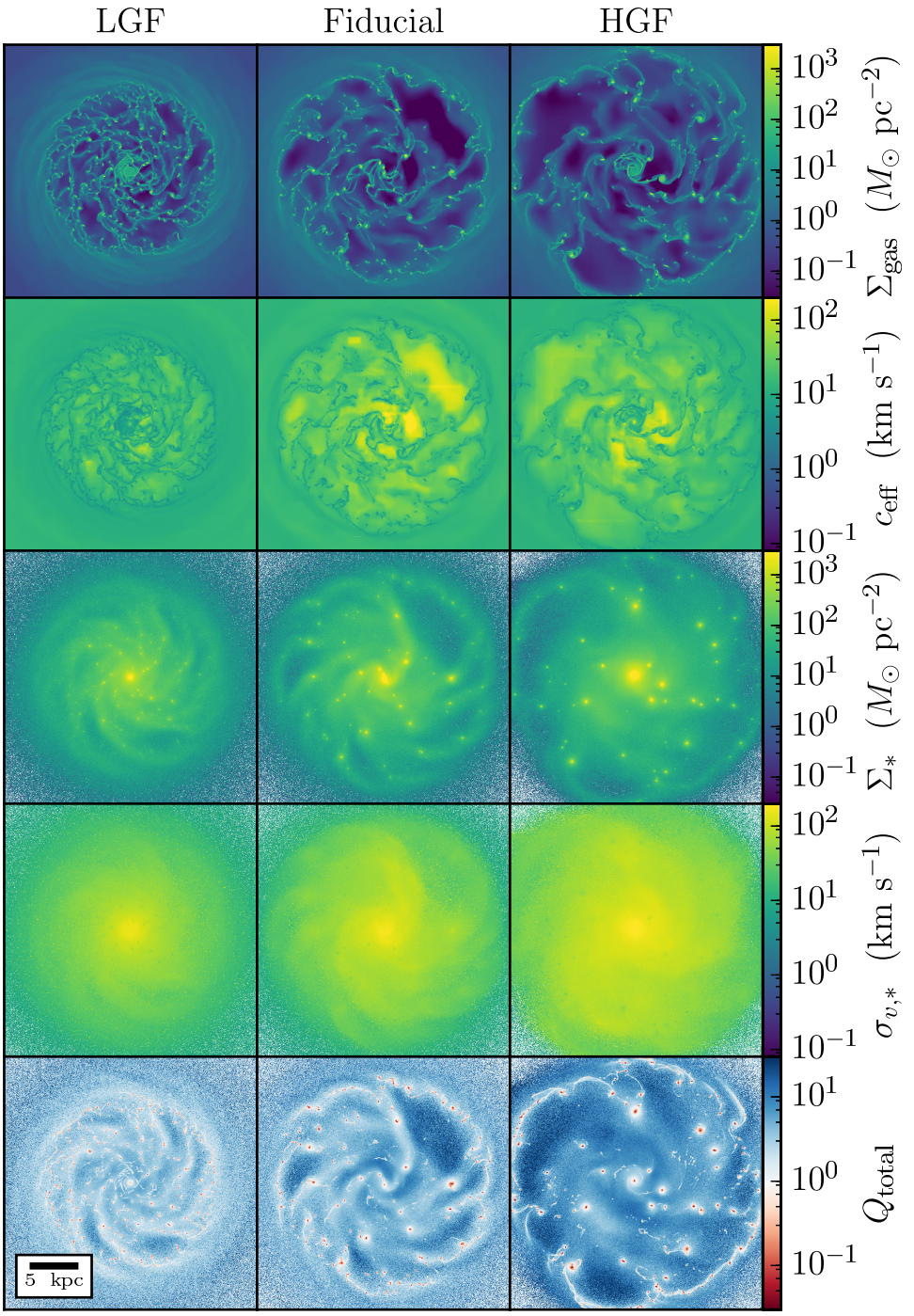

Figure 3.3: Same as Figure 3.2 but for each of the three different simulations at $T = 500$ Myr.

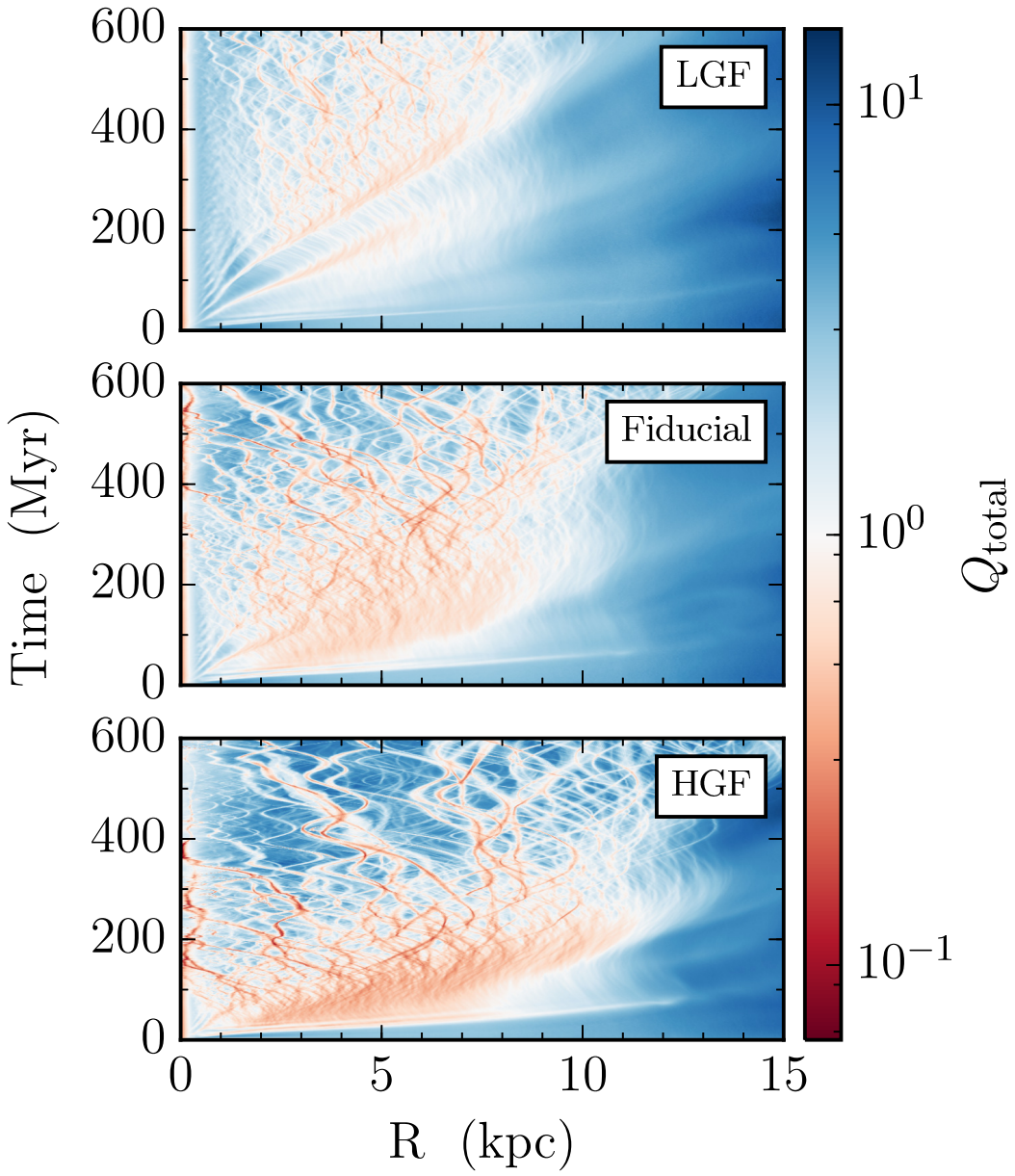

Figure 3.4: The time evolution of the azimuthally averaged Toomre Q parameter in each of our simulations (see Equation 3.22). This estimate includes the combined contribution of both the gas and stars. The color scale is chosen such that regions that are gravitationally unstable are colored red, regions that are marginally stable are colored white, and regions that are stable are colored blue.

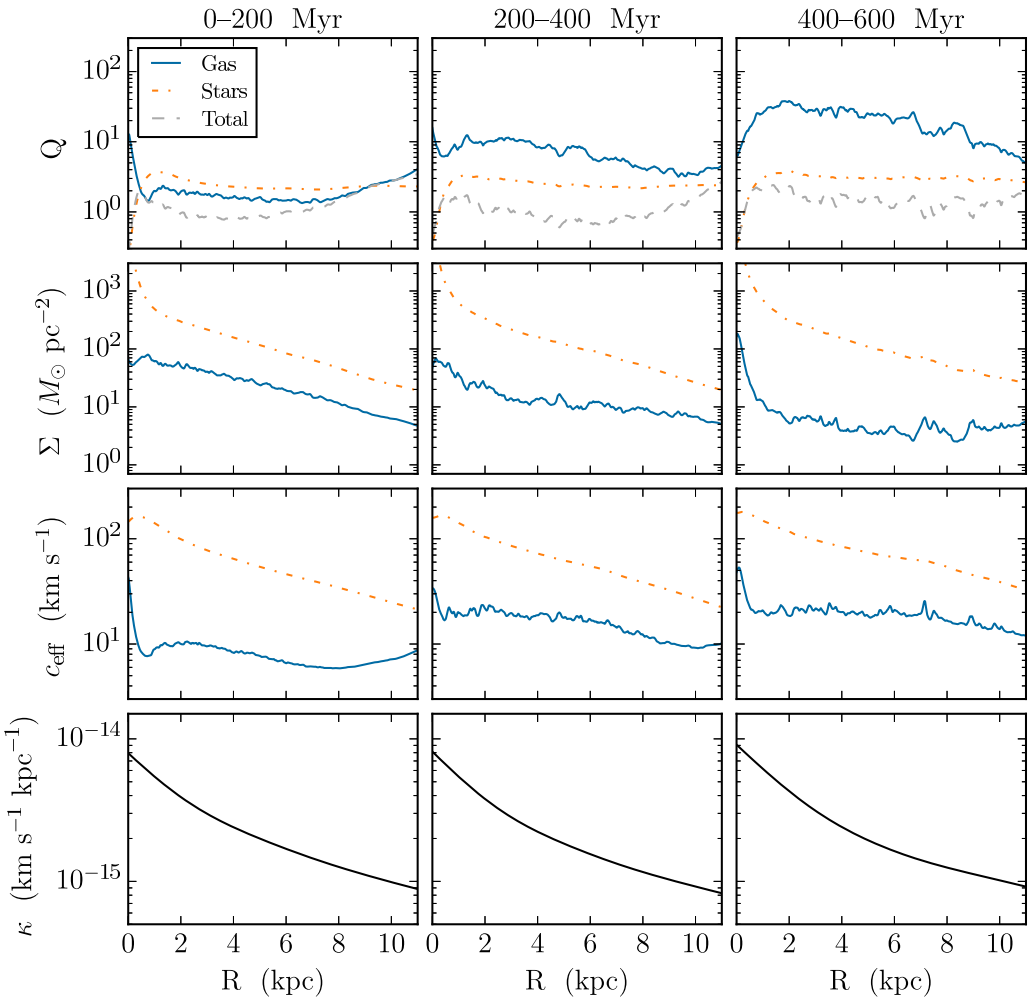

Figure 3.5: Time averages of the Toomre Q parameter (top row), the surface density (second row), and effective sound speed (third row) for the gas and stars averaged over three different periods (indicated at top) in the fiducial simulation. The bottom row shows the local epicyclic frequency κ, which is nearly time-invariant. The evolution in $Q_{\rm total}$ is primarily driven the evolution in $Q_{\rm gas}$, which in turn is driven by depletion in the gas supply and and increase in the gas velocity dispersion.

into stars, or merge with one another. As the gas in the gravitationally bound clouds is converted into stars, massive star clusters form inside the clouds. Once the initial period of collapse and fragmentation has passed, both the gas and stars spontaneously align into clear spiral arms. Later, as an increasing fraction of both the gas and stars collects inside the gravitationally bound clumps, the spiral structure becomes less clearly defined. These long-lived dense clouds are very similar to those seen by Hopkins et al. (2012) in their simulations with no feedback.

Gas in the innermost regions is stabilized by the presence of the bulge. In the bulge, the gas quickly stabilizes in a thin disk. Since the disk is above our density threshold for star formation, the central disk disappears as it converts itself into newly formed stars.

The combination of gravitational collapse and shear induces significant turbulent motion in the gas, with typical velocity dispersions of 10–20 km s^{-1} in the dense gas. The hot, low density gas in the interarm regions develops comparatively weak turbulence, although the effective sound speed is still quite large due to the relatively high gas temperatures in the interarm regions. The stellar orbits do not experience significant heating or dissipation, retaining the $\sim$40 km s^{-1} velocity dispersion present in the initial conditions.

The Toomre Q parameter tends to increase in time. In our initial conditions, for all three simulations $Q \sim 1$ throughout the disk. As soon as the gas is able to cool and begin collapse, $Q \ll 1$. As collapse proceeds, the typical surface density decreases and the degree of turbulence increases, leading to Q steadily increasing in time. Regions

in which gravitationally bound clumps develop consistently exhibit $Q \ll 1$, even at late stages, but, as we show below, azimuthal averages of Q are > 1. The locally-low values of Q within the bound clumps can mostly be attributed to very high gas and stellar surface densities in these regions. We do not see any significant increase in the stellar velocity dispersion in these regions, and we see only a modest increase in the gas effective sound speed. See subsection 3.5.1 below for more discussion of how the parameter Q evolves.

The stellar and gas dynamics in all three simulations are very similar. Increasing the gas fraction leads to quicker collapse. Decreasing the gas fraction produces a slower collapse in which the gas spends a longer amount of time in filaments rather than dense clumps. Spiral arms are more prominent in the simulation with low gas fraction, presumably because they do not have enough time to be disrupted by the formation of gravitationally bound clouds and accompanying star clusters. The star forming portion of the disk is also more compact, since regions at the outskirts of the disk are no longer dense enough to cool and collapse.

The degree of gravitational instability displays a weak dependence on the gas fraction. Since the high gas fraction run is able to process a much larger fraction of the gas present in the initial conditions, it reaches a higher typical $Q_{\rm total}$ value due the lower typical gas surface densities in the depleted gas disk. The low gas fraction run exhibits less variation, with $Q_{\rm total} \sim$ 1–3 throughout the disk. In all three cases, the disks are formally stable according to classical Toomre analysis, with $Q_{\rm total} \gtrsim 1$.

A robust feature of all of our simulations is that gravitationally bound clouds

form and then are unable to be destroyed by any mechanism besides gas exhaustion. This leads to the formation of large star clusters composed of stars that formed dynamically in the simulations. These star clusters in turn become a significant contribution to the mass distribution in the midplane, creating substantial streaming motions and departures from a smooth axisymmetric rotation curve. In the companion paper (Goldbaum et al., 2015, in preparation) we show that feedback capable of disrupting these complexes is necessary to form realistic smooth disks and prevent the formation of overly massive star clusters.

3.5 Results

3.5.1 Gravitational Instability

Since our simulated galaxies do not include a prescription for star formation feedback, the primary driver for the dynamical evolution of our model galaxies is gravitational instability. While the initial conditions for our simulations are formally stable, cooling allows the gas to quickly lose hydrostatic support, leading to catastrophic collapse in the vertical direction. In addition, our shearing self-gravitating disks are susceptible to the classic Toomre (1964) instability.

This story can be inferred by inspecting Figure 3.4, where we plot the time evolution of the azimuthal average of $Q_{\rm total}$. The initially stable disk quickly becomes unstable (e.g., the regions that show up in red in the bottom half of each subplot). The instability leads to a radially expanding wave of collapsing gas. Soon after, the gas collects in gravitationally bound clumps, which proceed to migrate through the disk,

both radially inward and outward. The regions inside the gravitationally bound clouds are formally unstable according to a local Toomre analysis due to their very high surface densities. The interclump regions reach relatively high values of $Q_{\rm total}$ so these regions are formally stable to collapse.

This process plays out in all three simulations, albeit with varying collapse speeds and degrees of violence. The high gas fraction case exhibits a clear transition from gravitational instability to a disk dominated by clumps. The low gas fraction case is able to reach an equilibrium state, with the bulk of the gas near $Q_{\rm total} \sim 1$. The fiducial case is intermediate, exhibiting a equilibrium state for a few hundred Myr before evolving into a giant clump dominated phase.

We can see what is driving the evolution of $Q_{\rm total}$ by inspecting Figure 3.5. We show the evolution in $Q_{\rm total}$ (top row) along with the variable quantities that determine $Q_{\rm total}$: the gas and stellar surface density and effective sound speed, as well as the epicyclic frequency. We see that both the epicyclic frequency and the stellar surface density and velocity dispersion show little variation over the course of the simulations.

On the other hand, the gas surface density and effective sound speed show significant variation. This drives a secular increase in $Q_{\rm gas}$ over the course of the simulation. In turn, this increase in $Q_{\rm gas}$ leads to the secular increase in $Q_{\rm total}$ Eventually, once the gas supply is exhausted, $Q_{\rm gas} \gg 1$, so $Q_{\rm total}$ approaches Q_*.

3.5.2 Mass Transport

Here we examine the radial flow of material in the disks of our simulated galaxy models. We measure if there is any net flow of material either from the galactic center

outward or from the outskirts inward. In addition, we examine the detailed radial and time dependence in the gas mass flux.

If Figure 3.6 we present our measurements of the gas mass flux as a function of radius and time. All three simulations exhibit similar overall behavior. Initially, the models exhibit significant ringing as the disks initially collapse and settle down. In this stage the mass flux is dominated by rings of material experiencing alternating bands of inward and outward flow. After the initial collapse phase, the gas collects in gravitationally bound clouds. For the rest of the simulation, the mass flux rate is primarily determined by the inward and outward flow of the gravitationally bound clumps. As spiral arms develop, the gravitational potential in the disk begins to develop non-axisymmetric components that tend to drive the gas clumps both radially inward and outward.

Along with the detailed variation in the mass flux, we would also like to know if there is any net mass flux once the disk has settled down into a quasi-equilibrium state. To answer this question we make use of the time averaging algorithm described in subsection 3.3.9. In this way we only consider the mass fluxes measured above the blue lines in Figure 3.6, which delineate the approximate time at which the disk has settled into a steady state.

This averaging procedure results in the time-averaged mass-flux measurements in the top panel of Figure 3.7. For each simulation, we plot the time-averaged mass flux as a function of radius. We find that there is a net inward flux of gas at most radii for all three model galaxies. The flux scales very roughly with the gas fraction, with a

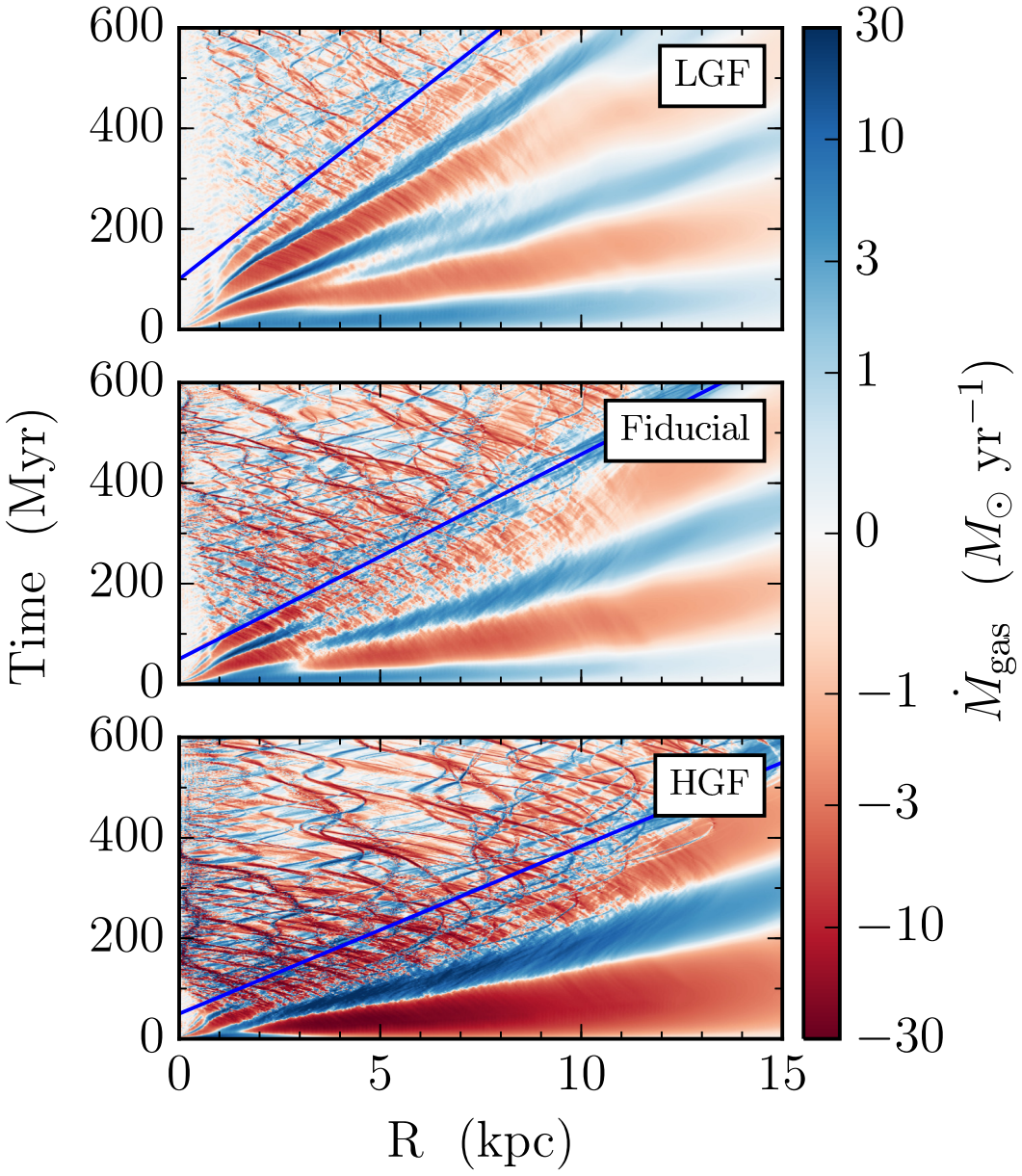

Figure 3.6: The gas mass flux as a function of radius and time for each of our simulations. The blue line indicates where we expect the disk has fully transitioned to an equilibrium condition, "forgetting" about the initial transients. Data below the blue line is excluded from time averages. For all three simulations the mass flux is initially dominated by coherent expanding rings as the gas disk collapses and reaches equilibrium. Later, the mass flux is dominated by a few gravitationally bound clouds.

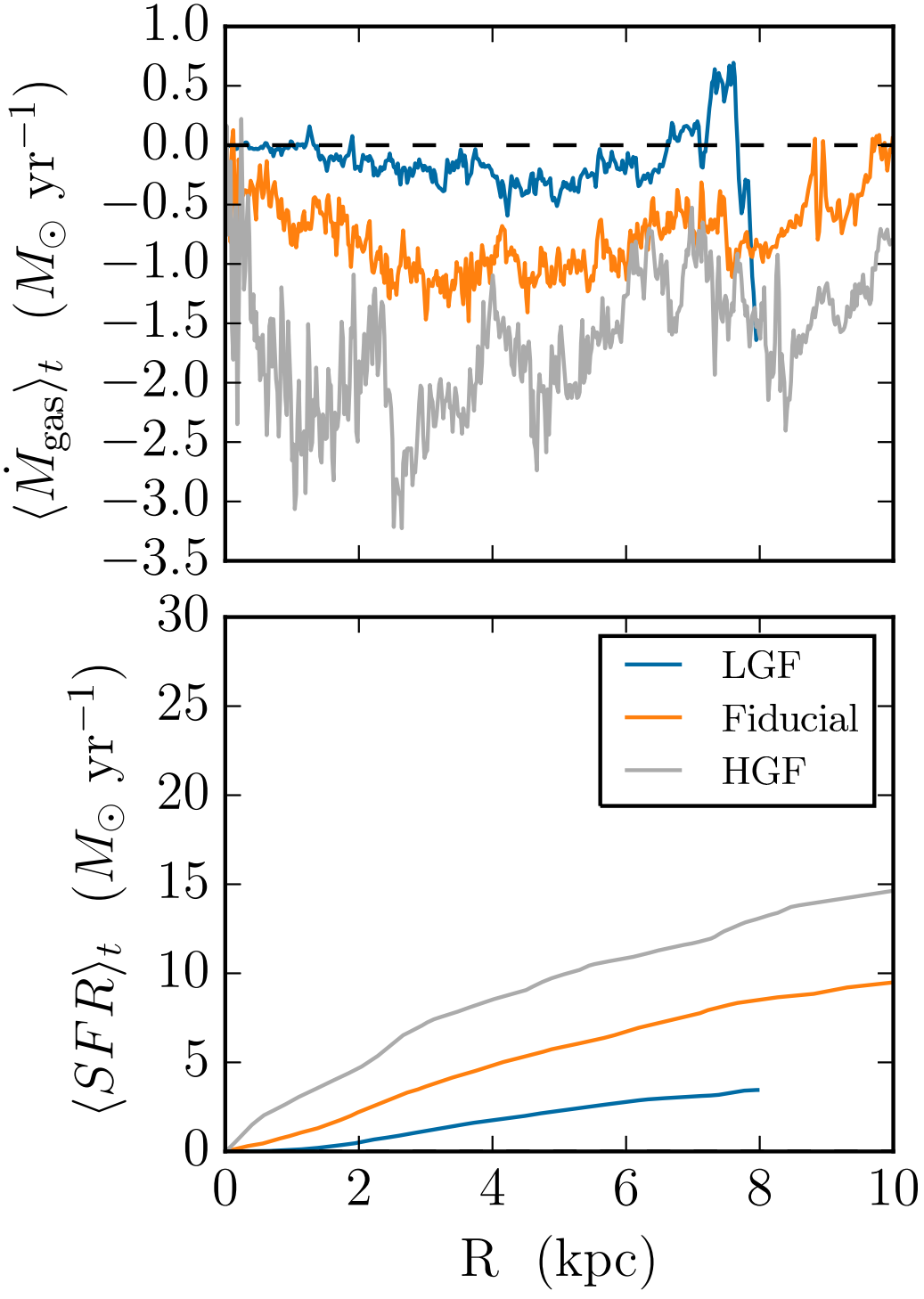

Figure 3.7: The time averaged mass flux (top panel) and radially cumulative star formation rate (bottom panel) as a function of galactocentric radius for all three simulations. In all cases there is a significant net inward flow of material toward the galactic center. In these simulations with no feedback, the inward mass flux is insufficient to supply star formation, leading to gas starvation in the center of the disk. However, if the star formation rate were reduced to the observed one, the mass inflow would be sufficient to fuel it.

typical mass flux of -0.3, -1.0, and -2.0 $M_\odot$ yr^{-1} mass flux in the low gas fraction, fiducial, and high gas fraction cases, respectively.

We might expect that the inward flow of gas is sufficient to supply the star formation in the inner regions of our model galaxies. To see if this is the case, we plot the time-average of the radially-accumulated star formation rate in in the bottom panel of Figure 3.7. The mass flux in the top panel is sufficient to supply the star formation in the bottom panel only if the mass flux is greater than the cumulative star formation rate at any given radius. Due to the very high star formation rates in these simulations with no feedback (c.f. Figure 3.1), we find that the inward flow of gas is insufficient to fuel the star formation rate in these simulations.

However, we note that this is a result of the unphysically-high star formation rates that our no-feedback simulations produce. If we instead consider the star formation rate that would be expected given the gas surface density distribution combined with observed star formation rates (e.g., Leroy et al., 2013), we reach the opposite conclusion: our inflow rates are sufficient to fuel star formation at observed levels. Indeed, our fiducial, Milky Way-like simulation produces mass transport at a rate of ~ 1 $M_\odot$ yr^{-1}, which is roughly the observed star formation rate in the Milky Way (e.g., Chomiuk & Povich, 2011). The question of whether inflows and star formation can be matched simultaneously in a simulation including feedback we defer to the companion paper.

3.5.3 Gas Velocity Structure

Here we examine the detailed gas velocity structure in our simulated galaxies. We are particularly interested in the radial dependence in the effective sound speed, the

anisotropy in the velocity dispersion, and the relative contribution of turbulent motions and thermal sound speed to the effective sound speed. To measure these, we perform the same sort of time averages described in subsection 3.3.9, this time focusing on the velocity fields in the fiducial simulation.

We present the results of this time averaging in Figure 3.8. In the top panel, we plot the average effective sound speed as a function of radius, along with the 1-σ variance in the effective sound speed at any given radius. The effective speed is typically of order $\sim$20 km s^{-1}, with a slow radial decline comparable to what is observed in H I maps of nearby galactic disks (section 1.1). This is perhaps surprising given that feedback processes are often invoked as an energy source for turbulence. Instead, we find generically that gravitational instability alone is sufficient to drive substantial turbulent velocity dispersions, more than enough to match observed gas velocity dispersions in resolved observations of galactic gas kinematics.

On the other hand, our galaxy models look quite different from real galaxies when we look at the anisotropy in the velocity dispersion components. To investigate this, in the middle panel of Figure 3.8 we present the time-averaged, azimuthally averaged ratio of the vertical velocity dispersion to the in-plane velocity dispersion in the fiducial galaxy model, $\sqrt{2}\sigma_{v,z}/\sigma_{v,d}$. We include the factor of $\sqrt{2}$ in the numerator so that a value of unity would correspond to a flow field with isotropic turbulence, in which the dispersion in the two in-plane components of the velocity field account for exactly twice as much kinetic energy as the one out-of-plane component. In our model galaxies, the we find that this ratio is approximately 0.5 over the bulk of the disk, indicating that

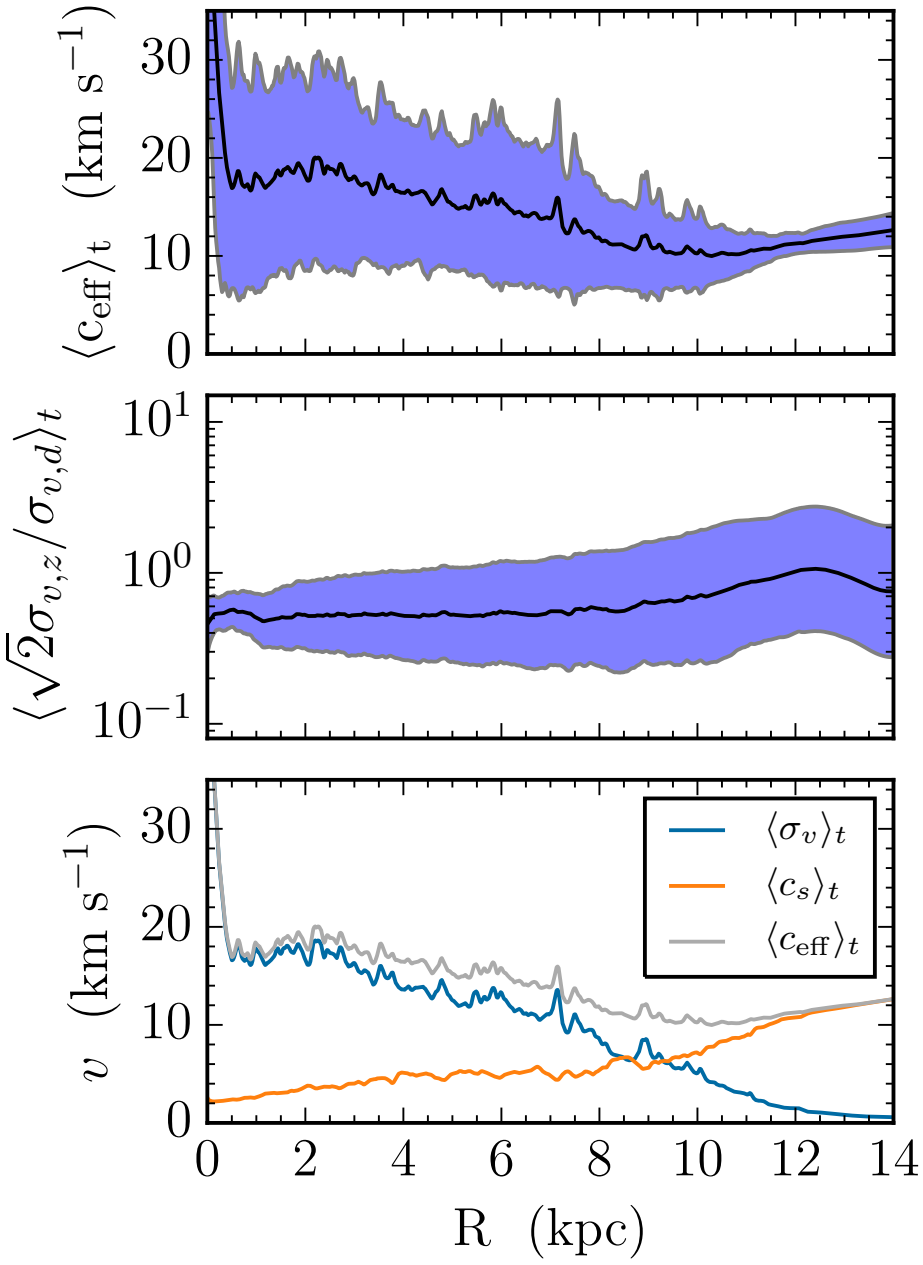

Figure 3.8: The time-averaged gas effective sound speed (top and bottom panel) and velocity dispersion anisotropy (middle panel) for our fiducial simulation. Shaded blue regions indicate the 1-σ scatter at a fixed radius. In the bottom panel, we show the contribution to the effective sound speed due to the velocity dispersion and sound speed. In the inner disk, bulk velocity dispersion dominates the effective sound speed, while at large radii the thermal component dominates.

in-plane motions contribute substantially more to the turbulent kinetic energy. This can also be seen in the thickness of our disks, where we typically find that the scale height is of order one or two cell spacings on the maximum refinement level. The extreme 2D disks we form are likely an artifact of the lack of feedback in our simulations. Momentum from supernova explosions should be able to destroy gravitationally bound clumps and accelerate material in the vertical direction. This should make the velocity field more isotropic on average and increase the typical scale height.

Finally, we show in the bottom panel of Figure 3.8 how the effective sound speed we measure in the gasses disk is primarily due to bulk turbulent motions. The small sound speed we measure is typical of the dense gas in our simulation, which is typically cools to temperatures of ∼200–300 K due to metal line cooling. The large velocity dispersions we measure indicates that the dense gas participates in large-scale turbulent motions.

3.6 Discussion and Conclusions

3.6.1 Turbulence in a Gravity-Dominated ISM

Our simulations show, in agreement with previous numerical studies by Agertz et al. (2009, 2015) and Bournaud et al. (2010), that gravitational instability is capable of driving turbulence and stabilizing a disk galaxy at $Q \gtrsim 1$ even in the absence of any additional energy input from star formation. This state is characterized by a total thermal plus non-thermal velocity dispersion the decreases slightly with radius from ~ 20 km s^{-1} near galactic centers to ~ 10 km s^{-1} at large radii, in good agreement with

observations. Indeed, the only possible-significant disagreement between the kinematic behavior found in our simulations and that observed in nature is that our galaxies' velocity dispersions are anisotropic by a factor of ~ 2, leading to a scale height that is too small. Nonetheless, our results suggest that, even if stellar feedback is required to explain the vertical velocity distribution of the ISM, it need not be the dominant energy source for all turbulent motions. Gravity alone can generate the required in-plane motion.

It is interesting to consider our simulations in light of the arguments commonly made that star formation feedback is the dominant driver of turbulence in galaxies. The primary observational argument for feedback driving turbulence is that there is a correlation between star formation rate and velocity dispersion, both within galaxies (Tamburro et al., 2009) and from galaxy to galaxy (Green et al., 2010). However, our simulations would also display precisely such a correlation: the regions of our galaxy that have the highest velocity dispersion are also the most strongly-star forming, and our models with the highest gas fractions show both the highest star formation rates and the highest velocity dispersions. The point is not that feedback cannot drive turbulence, simply that a correlation between star formation and turbulence does not necessarily imply a causal relationship between the two. A correlation of this sort can be produced even when there is no feedback.

The fact that galaxies can maintain $Q \gtrsim 1$ and strong turbulence without star formation feedback calls into question analytic models in which galaxies' star formation rates are set by the need to maintain $Q = 1$ (e.g., Thompson et al., 2005; Faucher-

Giguère et al., 2013). We find that galaxies can maintain $Q = 1$ regardless of the level of star formation feedback. Feedback is still needed to produce star formation rates in agreement with observation, but the condition that determines the level of feedback and star formation appears to be completely decoupled from the need to maintain $Q \gtrsim 1$.

3.6.2 Fueling Star Formation, From $z \sim 2$ to Today

The primary result of our simulations is that gravitational instability-driven turbulence is capable of inducing significant bulk mass flows in galaxies, leading to a migration of mass inward from the passive outer regions of disks to toward their actively star-forming centers. Inward mass transport rates are comparable to star formation rates for typical L_* galaxies. While there has been a great deal of work done on such inward migration in the context of the observed giant clumps in $z \sim 2$ galaxies (e.g., Genzel et al., 2008; Cresci et al., 2009; Dekel et al., 2009a; Bournaud & Elmegreen, 2009), our simulations show that a completely analogous phenomenon can operate for Milky Way-like galaxies at $z = 0$, and that the difference between clumpy galaxies at $z \sim 2$ and galaxies today is quantitative, not qualitative.

An important implication of galaxies' ability to transport gas inward at rates comparable to their star formation rates is that their available fuel for star formation is their full gas reservoir, not simply the material in the actively star-forming inner disk. This is significant because, while gas depletion times are much less than the Hubble time only considering inner disk gas, the same is not true for many galaxies at $z = 0$ if we consider the full gas reservoir. For a volume-limited sample of local star-forming galaxies with stellar masses in the range $\log(M_*/M_\odot) = 10 - 11.5$, Saintonge et al.

(2011) find typical H I depletion times of ~ 3 Gyr, with no strong dependence on stellar mass, and H_2 depletion times that range from $\sim 0.5 - 3$ Gyr from the lowest to the highest stellar masses in the sample. If galaxies have access to their full extended H I reservoirs to fuel star formation, then their total depletion times are simply the sum of these, implying that galaxies with stellar masses above $\sim 10^{11}$ $M_\odot$ have depletion times of ~ 6 Gyr. This is still less than the Hubble time, but not by much. Galaxies in this mass range could receive no new gas supply after $z \sim 1$ and still fuel all their present star formation, particularly once the contribution from stellar recycling is included.

Combined with the observation that gas depletion times are also comparable to or longer than the Hubble time in dwarf galaxies (e.g., Bigiel et al., 2010), we are forced to conclude that strong equilibrium between gas inflow and star formation may, by $z = 0$, exist only for galaxies in the relatively limited range of stellar masses from $M_* \approx 10^{9.5} - 10^{10.5}$ $M_\odot$, which corresponds to the mass range where galaxies are most efficient at converting baryons to stars (Behroozi et al., 2013). Galaxies outside this mass range may be far from equilibrium, contradicting one of the central assumptions of "bathtub" models of galaxy formation (e.g., Bouché et al., 2010; Lilly et al., 2013; Forbes et al., 2014b; Mitra et al., 2014).

Chapter 4

The Case of Strong Star Formation Feedback

4.1 Introduction

In this chapter we expand on the simulations of isolated disk galaxies presented in the previous chapter by including a novel prescription for star formation feedback. This subgrid model uses a prescription based on momentum-driven feedback from supernova explosions in an attempt to properly model the impact of supernovae on the ISM of our model galaxies.

- Supernova blastwaves are able to efficiently destroy dense concentrations of gas. These explosions tend to redistribute gas away from the dense star-forming phase of the ISM suppressing the star formation rate compared to the no feedback models by a factor of $\sim$ 5.

- Feedback dramatically alters the structure of the ISM in our model galaxies. We will show how, after decomposing the gas into various components ISM components, the model galaxies quickly attain an equilibrium state, in which the mass fraction of any given ISM component is constant in time. Typically, we find approximately third of the mass of the ISM is in the warm neutral medium (WNM), another third is in the cold neutral medium (CNM), and the rest is in the dense star-forming phase. A small fraction of the mass is contained in the thermally unstable atomic phase, and an even smaller fraction is transiently heated by H II regions and supernova explosions.

- The gravitational instability proceeds to an equilibrium state where $Q_{\rm total} \sim 2$ throughout the disk. Since a small fraction of the gas is converted into stars over the course of the simulation, the surface density and effective sound speed profiles remain approximately constant over the course of the simulation for both the gas and stars.

- Compared to the no-feedback case, the effective sound speed equilibrates to a lower value, $c_{\rm eff} \sim 10$ km/s. The effective sound speed is still dominated by the turbulent velocity dispersion in the inner disk and the thermal sound speed in the other disk.

- Radial mass inflows driven by gravitational instability are capable of supplying a substantial fraction of the mass necessary for star formation in the inner disk. Compared to the no feedback case, the mass transport rate is lower, we see a net mean mass flux of ~ 0.5 $M_\odot$/yr in the simulation we have run to completion.

Below, we briefly discuss the initial conditions for our simulations (subsection 4.2.1) and describe the theoretical basis and implementation for our supernova feedback model (subsection 4.2.2). This is followed by a discussion of our simulation results, beginning with an overview of the qualitative outcome of our simulations (subsection 4.3.1). Next, we discuss the impact of feedback on the star formation rates and star formation histories (subsection 4.3.2) and ISM structure (subsection 4.3.3) of our model galaxies. Finally, we investigate the evolution of the gravitational instability in our model disks, focusing on the gas velocity structure (section 4.3.4), Toomre Q parameter (section 4.3.4), and rate of radial mass transport (section 4.3.4). Finally, we review our results and discuss them in context of observations of radial mass transport and metal mixing in resolved observations of nearby disk galaxies (section 4.4).

4.2 Methods

4.2.1 Initial Conditions

To ease comparison with the models run without star formation feedback, in this chapter we will be discussing simulations initialized identically to the simulations described in chapter 3. This means that the initial collapse of the disk is identical, up to the formation of the first star particle. Briefly, the model galaxies are initialized using the `makegalaxy` code (Springel et al., 2005). The code makes use of the analytic framework of Mo et al. (1998) to predict the properties of a disk formed in a ΛCDM cosmology given a halo mass, disk mass, and halo spin parameter.

The initial conditions include dark matter and stars, which are modeled as

N-body particles, and gas defined on an AMR mesh. The dark matter particles are distributed according to a Hernquist profile, while the stars are distributed in a thin exponential disk and centrally concentrated bulge population. Particle initial conditions are generated by randomly sampling from an analytic distribution function, while the gas is initialized on the Enzo AMR mesh again following an analytic azimuthally symmetric exponential density profile.

The parameters of our model galaxies are chosen to loosely match the Milky Way, with a halo mass of $\sim 10^{12}$ $M_\odot$, a stellar disk mass of $\sim 10^{10}$ $M_\odot$, and a gas mass of $\sim 10^{9}$ $M_\odot$. We initialize three different galaxy models with identical parameters besides the initial gas fraction. The low gas fraction (LGF) model begins with a gas fraction of 10% (relative to the mass of the stellar disk), the fiducial model has a gas fraction of 20%, and the high gas fraction (HGF) model has an initial gas fraction of 40%.

4.2.2 Star Formation Feedback Model

Here we describe a novel subgrid model for star formation feedback that includes the effects of ionizing radiation from young stars, winds from evolved massive stars, and the energy and momentum released by individual supernova explosions.

Supernova explosions are a commonly used source of feedback in simulations of structure formation, in simulations on cosmological scales (Cen & Ostriker, 1992; Springel & Hernquist, 2003; Scannapieco et al., 2006) down to parsec scales (Joung & Mac Low, 2006; Kim et al., 2011a; Kim & Ostriker, 2015). It has been known for many years (Katz, 1992) that simply depositing $E_{\rm SN} = 10^{51}$ erg per supernova as thermal

energy in the location of the SNe explosions does not produce strong feedback in low resolution simulations. Instead, the energy, which must be shared by a large quantity of gas in a low resolution (typically at 10 – 1000 pc scales) volume element is quickly radiated away since the energy from a single supernova is not enough to heat the gas above $\sim 10^6$ K. Since the cooling rate is much higher at low temperatures, the gas instantly radiates away the thermal energy before the Supernova is able to transform the thermal energy into PdV work on the surrounding gas. Instead, low resolution simulations typically deposit the supernova energy continously over many timesteps instead of as discrete energy-injection events. The combined heating of many supernova over millions of years is sufficient to heat the gas in low resolution simulations, at the loss of resolving the fine-grained structure of the supernova feedback. On the other hand, high resolution simulations are able to either directly resolve the Sedov-Taylor radius or use a model for momentum feedback from individual supernova explosions (see, e.g. Stinson et al., 2006; Kim et al., 2011a). We adopt the latter approach, although at much coarser resolution than in Kim et al. (2011a), allowing us to model momentum feedback from supernovae without directly resolving the Sedov blastwaves.

The parameters for the model are carefully chosen to match a STARBURST99 (Leitherer et al., 1999; Vázquez & Leitherer, 2005; Leitherer et al., 2014) model of a young stellar population that fully samples the stellar initial mass function (IMF). As discussed above, our feedback models are identical to the runs without feedback up until the first star particle is formed. Once the first star particle forms, it immediately begins altering the properties of the AMR cell it occupies continuously in time over the

course of several million years while there is still a significant population of massive stars. This stage corresponds to ionization feedback from H II regions, and winds from massive stars. As each massive star reaches the end of its evolution, we include a prescription for momentum feedback from individual supernova explosions. This form of feedback alters the state of the cell the particle occupies as well as the surrounding cells, launching a spherically symmetric explosion in the region around the star particle. Below, we explain in detail how these various forms of feedback operate.

All star particles form with a uniform initial mass of 300 $M_{\odot}$. Within each of these particles we expect there to be a few stars massive enough to produce supernova explosions. We model this based on a scaled down version of a STARBURST99 model of a 10^6 $M_{\odot}$ stellar population. For such a massive cluster, we should expect $\sim 10^4$ Type II supernovae over the lifetime of the population. Scaling down to our star particles, we have an expectation value of $\lambda = 3.2$ SNe per star particle. The true number of SNe for each particle is chosen randomly at runtime, by drawing from a Poisson distribution function proportional to $\lambda^k e^{-\lambda}/k!$, where k is the number of SNe per particle.

Once we know the number of expected Supernovae per star particle, we predict the masses and time of each supernova event by drawing from the supernova delay time distribution predicted by STARBURST99. There is a one-to-one mapping between supernova delay time and progenitor initial mass, which we make use of here to predict the mass of each supernova progenitor. For each SN progenitor, we also record the expected main sequence ionizing luminosity (Parravano et al., 2003) for each SN progenitor (implicitly assuming that the ionizing radiation from less massive stars is

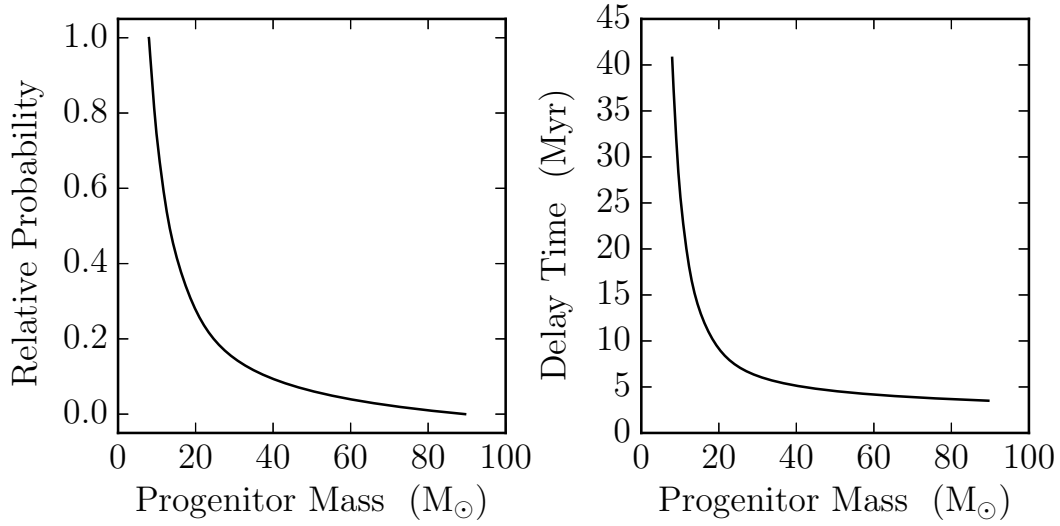

Figure 4.1: The distributions of supernova progenitor mass (left panel) and delay time (right panel) we use in our feedback model.

negligible) which we in turn use for our H II region feedback model. In practice, all of this data is regenerated at each timestep using unique random number streams seeded by the unique particle ID. This adds extra CPU cost in each timestep while avoiding the memory and communication costs of saving this data for all dynamically created star particles. This also allows us to use the simpler Fortran star particle machinery in Enzo rather than the more expensive and complicated star object machinery.

Once the massive stars in each star particle have been identified, we loop over all particles in the simulation, applying various forms of feedback to the hydrodynamic quantities defined on the Enzo AMR mesh.

H II Region Feedback

Massive stars emit copious amounts of ionizing radiation, capable of creating bubbles of warn, ionized gas in the densest regions of the ISM. These H II regions

can be dynamically important when considering the effect of Supernova explosions in a hydrodynamic simulation, since preheating the region around the star particle can ease the resolution requirements needed to properly resolve the energy-conserving phase of the Sedov-Taylor blastwave. In addition, H II regions are a substantial portion of the ISM of star forming galaxies, so including them at some level, even crudely as we do here, is a step towards producing a realistic global simulation of a galactic ISM.

In practice, we add H II region feedback to our simulations using the following algorithm. If a grid cell contains a dynamically created star particle containing unexploded massive stars, we increase the gas temperature to crudely emulate photoionization heating. The amount of heating is determined by comparing the volume of the Strömgren sphere $V_s = 4/3\pi R_s^3$ with the volume of the cell that the star particle resides in, $V_c = \delta x^3$, where δx is the local cell spacing. Here,

$$R_s = \left(\frac{3S}{4\pi \alpha_B n^3} \right)^{1/3} \tag{4.1}$$

is the Strömgren radius, determined by equilibrium between photoionization and recombination at a given density, S is the ionizing luminosity emitted by the star particle, n is the number density of gas in the host cell, and $\alpha_B = 2.6 \times 10^{-13}$ cm^3/s is the case-B recombination coefficient, assuming a temperature of 10^4 K. If $V_s > V_c$, the cell is heated to a temperature of 10^4 K. If the cell is already hotter than that, no heating is applied. If $V_s < V_c$, we heat the cell to $T = 10^4$ KV_s/V_c, effectively applying a volume filling factor correction. If more than one particles containing supernova progenitors are present in any given cell, they each contribute separately, increasing the cell temperature up to

a maximum of 10^4 K.

One major downside of this approach is that it is fully local. In principle, H II regions may grow to be larger than a single cell, suppressing H II region feedback and making it more difficult for heated cells to dynamically affect the state of the simulation. In practice this is not a big concern for the simulations we discuss here, since only the most massive rare stars will produce H II regions with radii bigger than 20 pc. In the future we plan to modify this feedback routine to apply feedback in a distributed fashion, in anticipation of high resolution simulations.

Winds from Massive Stars

In addition to heating by H II regions, very massive stars eject a substantial fraction of their envelopes, recycling gas back into the ISM. We include this effect in our feedback algorithm by alterind the density and internal energy of gas in cells that contain star particles associated with very young stellar populations. This serves to suppress star formation somewhat, since soon after a star particle forms, the gas in the cell where the particle spawned will heat up. In addition, this captures a significant fraction of the gas recycling from a young stellar population. We do not include the effect of AGB winds, although that is not a significant concern given that we run our simulations for less than one Gyr.

The winds are taken to be the result of the combined action of a stellar population. This simplifying assumption allows us to use the results of a STARBURST99 calculation for the wind properties. In practice, the mass ejection rate and the specific internal energy of the wind are given by the fitting formulas plotted in Figure 4.2.

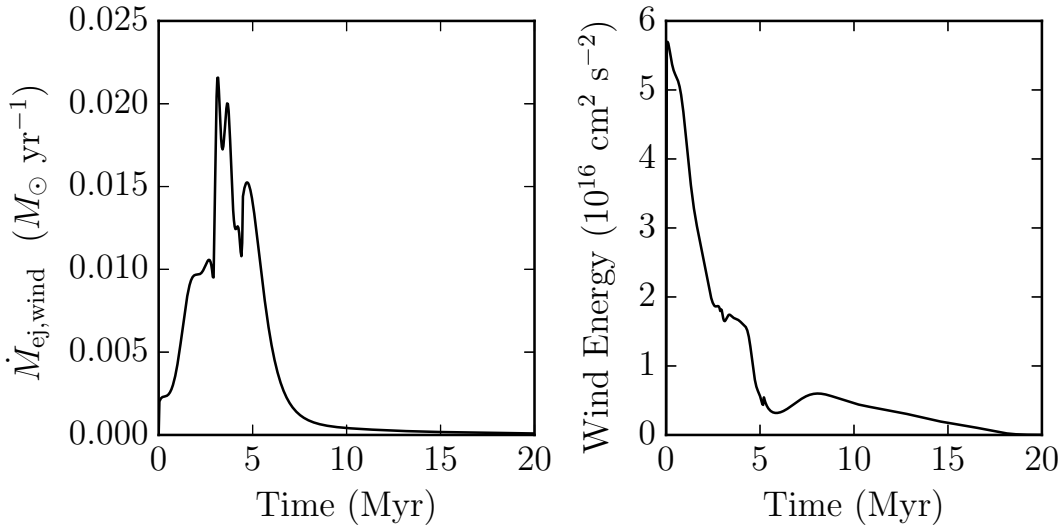

Figure 4.2: The mass ejection rate (left panel) and specific wind energy (right panel) used in our feedback algorithm. Star particles older than 2 Myr do eject mass due to winds.

These are implemented internally using a broken power-law fit to the outputs from STARBURST99. The metal fraction of the wind is assumed to be equal to the metal fraction of the star particle, which is determined by the metal fraction of the gas that initially formed the star particle.

Note that assuming the wind properties to be the same for all of our 300 $M_\odot$ star particles is not accurate. While this simplifies matters, we are ignoring the effects of stochasticity in the sampling of the stellar IMF. In the future we plan to calculate the wind properties based on the combined wind ejection rates for each massive star in the stellar population.

Supernova Explosions

Finally, here we describe the supernova feedback algorithm. Supernova feedback happens via two stages: energy feedback, followed by momentum feedback. The energy feedback prescription is designed to be accurate when the simulation is able to accurately resolve the Sedov-Taylor radius. In our simulations this hardly ever the case, nonetheless we include this effect in the hopes of producing a hot phase of the ISM, even if we are not able to directly resolve the expanding supernova bubbles. In practice this does not occur, as we will discuss in subsection 4.3.3 below.

The thermal feedback adjusts the temperature, mass, and metallicity of the cell enclosing the particle that spawns the supernova explosion. The energy increment is taken to be a constant, 10^{51} erg. This energy is deposited into a single cell, so it is shared by all of the gas within a single cell, leading to substantially more dilution than in a higher resolution simulation where the Sedov-Taylor scale is properly resolved (e.g. in Joung & Mac Low, 2006).

We also adjust the mass and metallicity in the host cell to account for mass injection due to the supernova ejecta. The mass and metallicity of supernova ejecta are determined by power-law fits to outputs from STARBURST99 as a function of delay time. The fitting formulas used in our feedback prescriptions are plotted in Figure 4.3

We experimented with pure thermal feedback in our 20 pc resolution simulations and found the feedback to be ineffective. While it does lead to the production of some hot gas, any decrease in the star formation rate was negligible, and the global morphology of the simulated galactic disks were identical to the no feedback case. In an

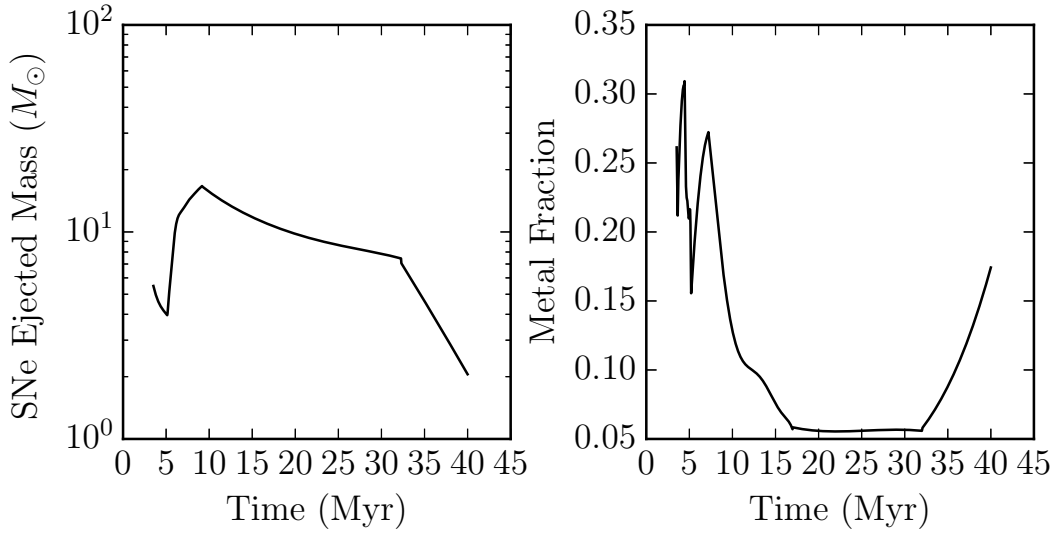

Figure 4.3: The ejected mass from a supernova event (left panel) and metal fraction (right panel) as a function of delay time.

effort to create more realistic disks, we have added a prescription for non-local blastwave feedback by directly depositing momentum into the simulation, launching an expanding shell of gas around the star particle.

The momentum feedback prescription used here proceeds as follows. First, we identify the grid cell where the star particle that will produce a supernova explosion resides. We approximate that the explosion happens in the center of the grid cell. This choice substantially simplifies the implementation since we can exploit symmetry to naturally produce a spherically symmetric explosion that conserves momentum by construction. In the future, we plan to use the prescription described in Simpson et al. (2014), which properly handles this problem. In practice this leads to a small loss of resolution at scales below our grid spacing. We do not expect a proper treatment of the sub-resolution position of the exploding supernova to substantially alter the results discussed below.

Once the cell at the center of the supernova bubble has been identified, we identify the 26 nearest neighbor cells. We then loop over each cell, depositing momentum

$$\Delta p_{\rm SN} = \frac{3 \times 10^5 \ {\rm M}_\odot \ {\rm km/s}}{26} \, \hat{r}, \tag{4.2}$$

where $\hat{r}$ is the unit vector connecting the center of the supernova host cell to the neighbor cell under consideration. This value was chosen based on detailed simulations of supernova explosions in a turbulent ISM where the net momentum injection into the ISM can be directly measured (Cioffi et al., 1988; Kim et al., 2011a; Kim & Ostriker, 2015). If the supernova explodes at the edge of a grid, the portion of the explosion that would happen in cells living on a different grid is not included, effectively "cutting off" the supernova explosion and abandoning spherical symmetry. This happens relatively rarely, but is a deficiency of our feedback algorithm, albeit one that is commonly used in distributed feedback calculations in the Enzo code (Kim et al., 2011b; Simpson et al., 2014). To avoid producing spuriously fast-moving gas when a supernova happens to go off near a relatively low-density cell, we limit the maximum change in velocity for the gas in any given cell to 1000 km/s.

To conserve energy, we record the change in kinetic energy for each cell that we deposit momentum into. The total net increase in kinetic energy in the cells surrounding the supernova host cell are then deducted from the thermal energy to be deposited into the host cell. In practice, at 20 pc resolution, most of the thermal energy is used to launch the momentum feedback we put in by hand. We discuss this effect in subsection 4.3.3 when we note how the hot phase of the ISM is suppressed compared to

observed hot phases in nearby star forming galaxies.

4.3 Results

Here we describe the results of our simulations. First, in subsection 4.3.1, we focus on the qualitative evolution of our simulated disks, focusing on the morphology of our simulated galaxies. Next, in subsection 4.3.2 we describe the impact of our feedback algorithm on the star formation rates and star formation histories. Finally, in subsection 4.3.3 we go into some detail describing the structure of the ISM in our simulated galaxies, showing how feedback moderates the amount of gas available for star formation.

4.3.1 Qualitative Outcome

We present snapshots of the low gas fraction simulation at four times in Figure 4.5 and snapshots of the low gas fraction and fiducial simulation with and without feedback in Figure 4.5. Each figure displays the gas and stellar surface density and effective sound speed, as well as $Q_{\rm total}$, which includes contributions from both gas and stars. We exclude the high gas fraction run from this portion of the analysis since we have only been able to run it for ~ 150 Myr of simulation time. The outcome of all three simulations are similar to the evolution depicted in Figure 4.3.1, so we will describe the similarities between the three simulations there and explain how the results vary as a function of gas fraction below.

Early in the simulation, the morphology is dominated by circular, expanding

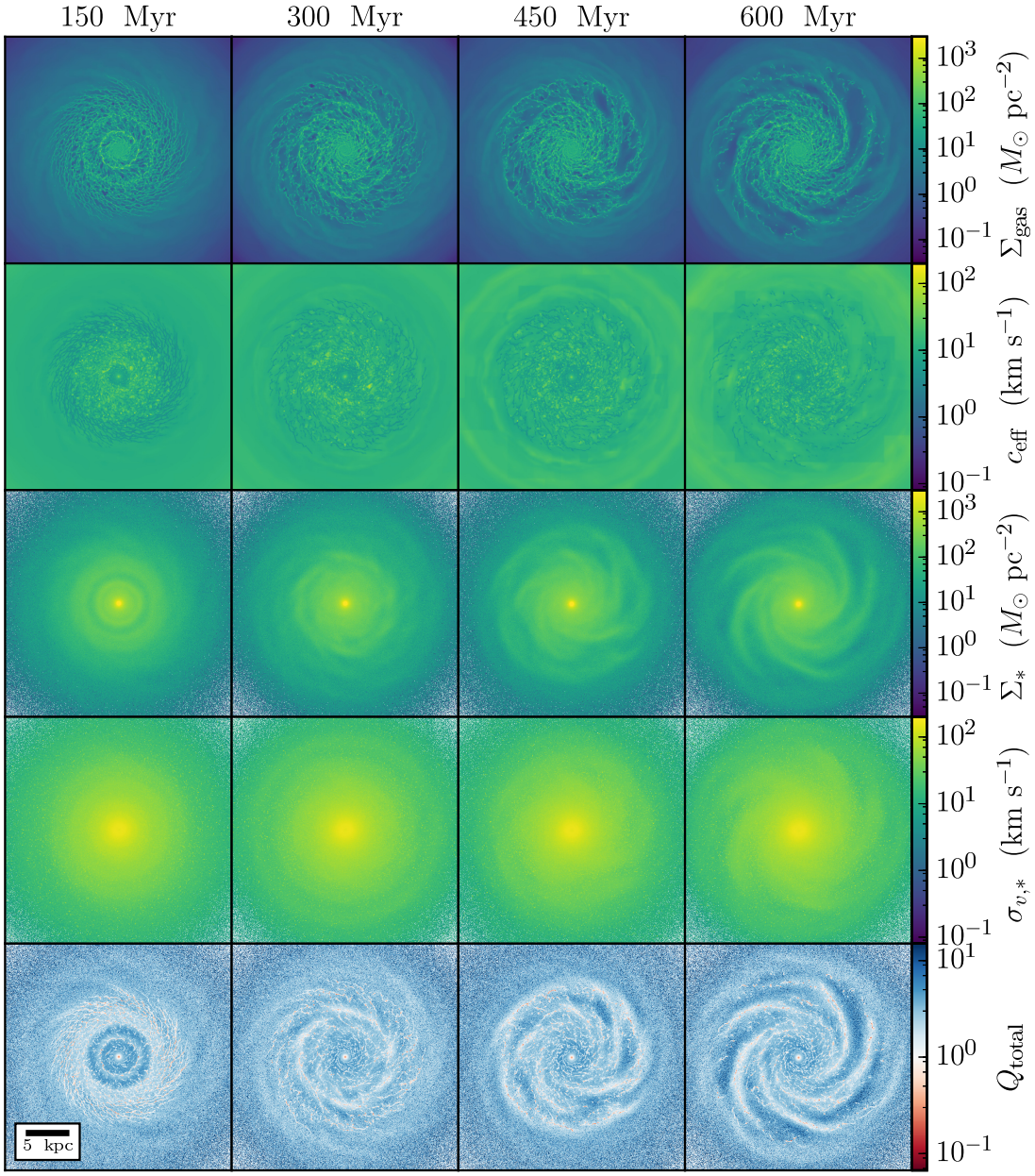

Figure 4.4: The surface density and vertically-averaged effective sound speed for both the gas and stars, as well as the combined Toomre Q parameter at T = 150, 300, 450, and 600 Myr.

rings of gas and stars, which we interpret as a manifestation of unphysical transient behavior as the disk settles down into statistical equilibrium. Later, the rings dissipate, giving way to prominent spiral arms. The arms form spontaneously, and are clearly visible in both the gas and stellar surface density maps.

The gas in the inner disk is concentrated in thin filaments that are continuously sheared, leading to a tightly wound spiral pattern. At intermediate radii, the filaments break up into individual isolated clouds. This morphology develops as a smooth transition along the prominent spiral arms at the edge of the star forming disk. Gas in the outer disk is smoother, only collapsing into more or less isolated clouds towards the end of the simulation. Individual supernova explosions may also temporarily evacuate the area around the blastwave. This is visible in the gas density, in upper right quadrant of the disk in the snapshot at $T = 300$ Myr in Figure 4.3.1.

The gas effective sound speed is roughly constant with radius, in an azimuthally averaged sense, although with significant variation at any given radius. Individual supernova explosions produce a substantial amount of hot gas in the inner disk, with $c_{\rm eff}$ as high as $\sim$ 50–100 km/s in interarm regions. Dense gas collects in filaments, where $c_{\rm eff}$ is suppressed compared to the interarm regions, with $c_{\rm eff} \sim$ 1–10 km/s. We will show below that the effective sound speed in the dense gas is dominated by the turbulent velocity dispersion. In the outskirts of the galaxy, supernova heated regions become rarer. Here the interarm gas is still heated to 10–20 km/s, and appears similar to the interarm gas seen in the simulations without feedback.

The stellar component is substantially smoother, albeit morphologically similar

to the gas on kpc scales. One the disk has settles, the stars show a prominent $m = 5$ spiral pattern. The stellar velocity dispersion does not vary much over the course of the simulation, showing neither appreciable heating or dissipation.

Compared to the simulations with no feedback, the Toomre Q parameter has substantially different structure. In these simulations $Q_{\rm total}$ is much smoother. Early in the simulation, as the disk comes into equilibrium, $Q_{\rm total} \simeq 1$–2, with $Q_{\rm total} \lesssim 1$ in the highest gas density regions and $Q_{\rm total} \simeq 1$ in the interarm regions. Later in the simulation, $Q_{\rm total}$ increases in the interarm regions, reaching as high as ~ 5.

We can see the remarkable effect of feedback on the structure of our simulated galaxies by comparing directly with the runs with no feedback, as in Figure 4.5. Rather than collapsing into gravitationally bound clouds, the gas is distributed relatively smoothly, although it is modulated by the spiral pattern. We can also that this tends to decrease the typical effective sound speed in the interarm regions. Since gravitationally bound clouds are efficiently destroyed by supernova feedback, the stellar distribution is also substantially more smooth, showing no clear concentrations of stars besides the bulge population present in the initial conditions.

When comparing the low gas fraction and fiducial simulations with feedback, we see the disks look very similar. The star forming region is smaller in the low gas fraction case since the outskirts of the disk have not had time to collapse, but the inner disks are practically indistinguishable. We do see some differences in the effective sound speed, which is somewhat higher in the inner portion of the fiducial simulation. This is due to gas being heated by both photoionization and supernova thermal feedback.

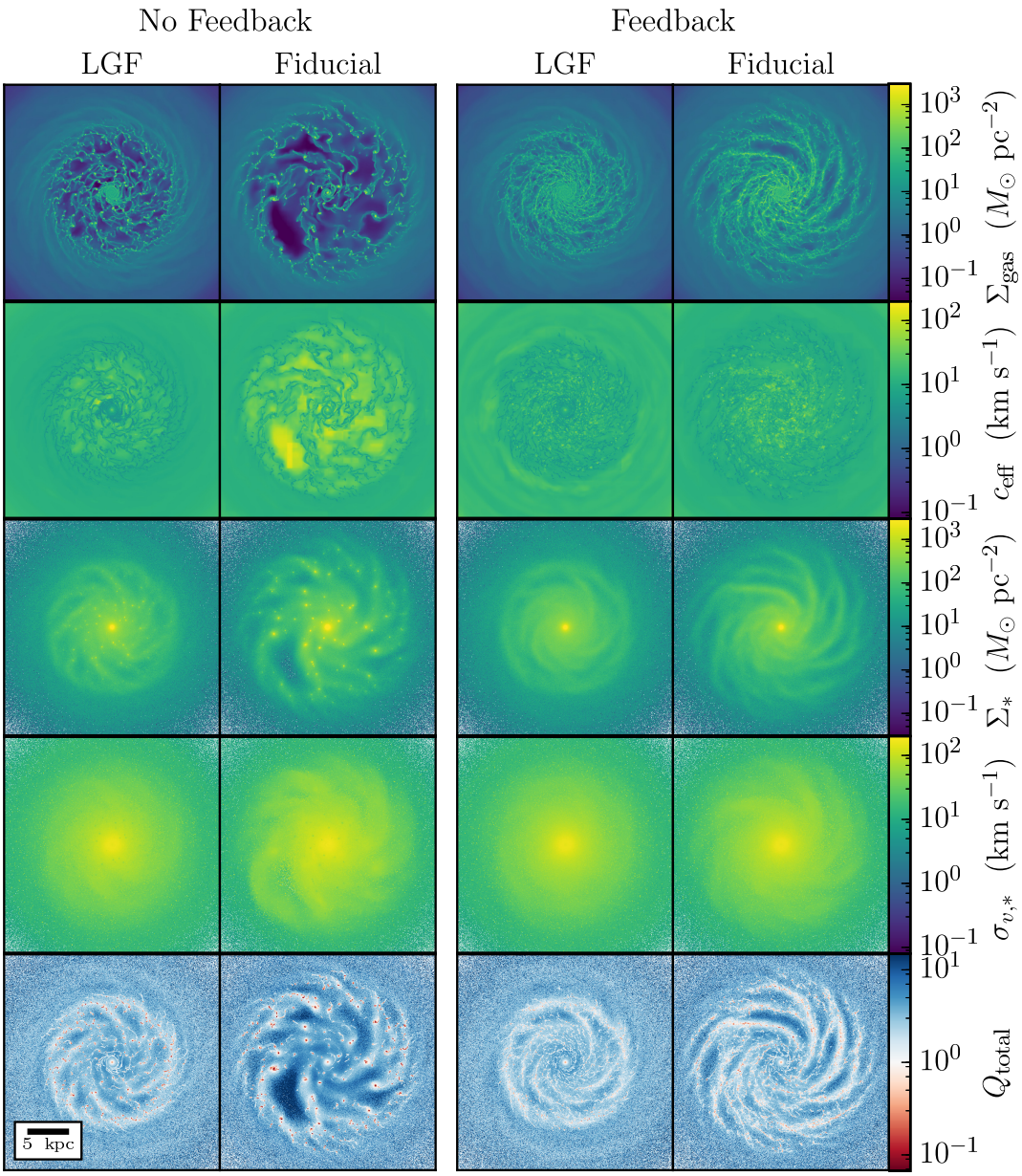

Figure 4.5: Same as Figure 4.3.1, but showing a fixed simulation time ($T = 400$ Myr) for four simulations. We show both the low gas fraction (first and third columns) and fiducial (second and fourth column) cases with (left two columns) and without feedback (right two columns).

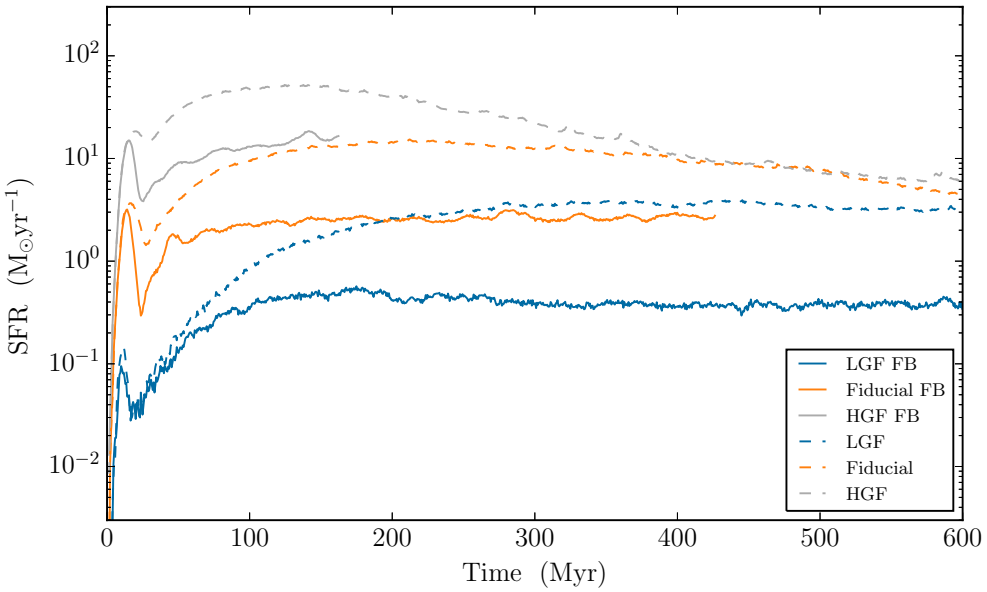

Figure 4.6: The star formation rate history for our simulated galaxy models. We show the low gas fraction (blue), fiducial (orange), and high gas fraction (gray) cases, both with (solid lines) and without (dashed lines) star formation feedback.

We will show below that the star formation rate is substantially higher in the fiducial model and that the typical star formation rate is not linear in the gas surface density.

4.3.2 Star Formation

Star formation feedback has a profound effect on the star formation rates in our model galaxies. In Figure 4.6, we show the star formation history of our galaxy simulations as measured by histogram-binning by creation time the dynamically created star particles present at the end of each simulation. We show both the models run with and without feedback for all three choices of initial gas fraction.

Initially, the models are identical, the star formation rate shows a peak followed by a decline. This pattern is driven by the dynamical nature of the collapsing disk.

However, in both the fiducial and high gas fraction cases, the initial peak is somewhat depressed and the following trough in the star formation history are deeper. In the low gas fraction case the star formation histories agree for a somewhat longer period, diverging only as the star formation rate begins to increase again.

Eventually, for the low gas fraction and fiducial cases the star formation rates in the simulations with feedback converge to a quasi-equilibrium value. The high gas fraction case also appears to be converging to an equilibrium value, although it has not run long enough to fully converge. For the low gas fraction, fiducial, and high gas fraction cases respectively, the star formation rates appear to converge to $\sim$ 0.3–0.5 $M_\odot$ yr^{-1}, $\sim$ 2 $M_\odot$ yr^{-1}, and $\sim$ 10–20 $M_\odot$ yr^{-1}. For the runs with feedback, we do not see the long-term decrease in the star formation rate seen in the runs with no feedback. Those decreases are primarily driven by gas depletion, and since the star formation rate is substantially depressed in the simulations with feedback, there is not sufficient time over the course of our simulations to substantially deplete the gas.

This can also be seen in Figure 4.7, where we plot the time evolution of the azimuthally averaged gas depletion time. Here

$$t_{\rm dep} = \frac{\Sigma_{\rm gas}}{\Sigma_{\rm sfr}} \tag{4.3}$$

is the time it would take to consume all of the gas at a given position in a galaxy. Resolved observations of nearby star forming galaxies indicate typical depletion times in the molecular phase of $\sim$ 2 Gyr, with approximately third of a decade of scatter (Bigiel et al., 2008a, 2011; Leroy et al., 2013). We see that in our model galaxies we

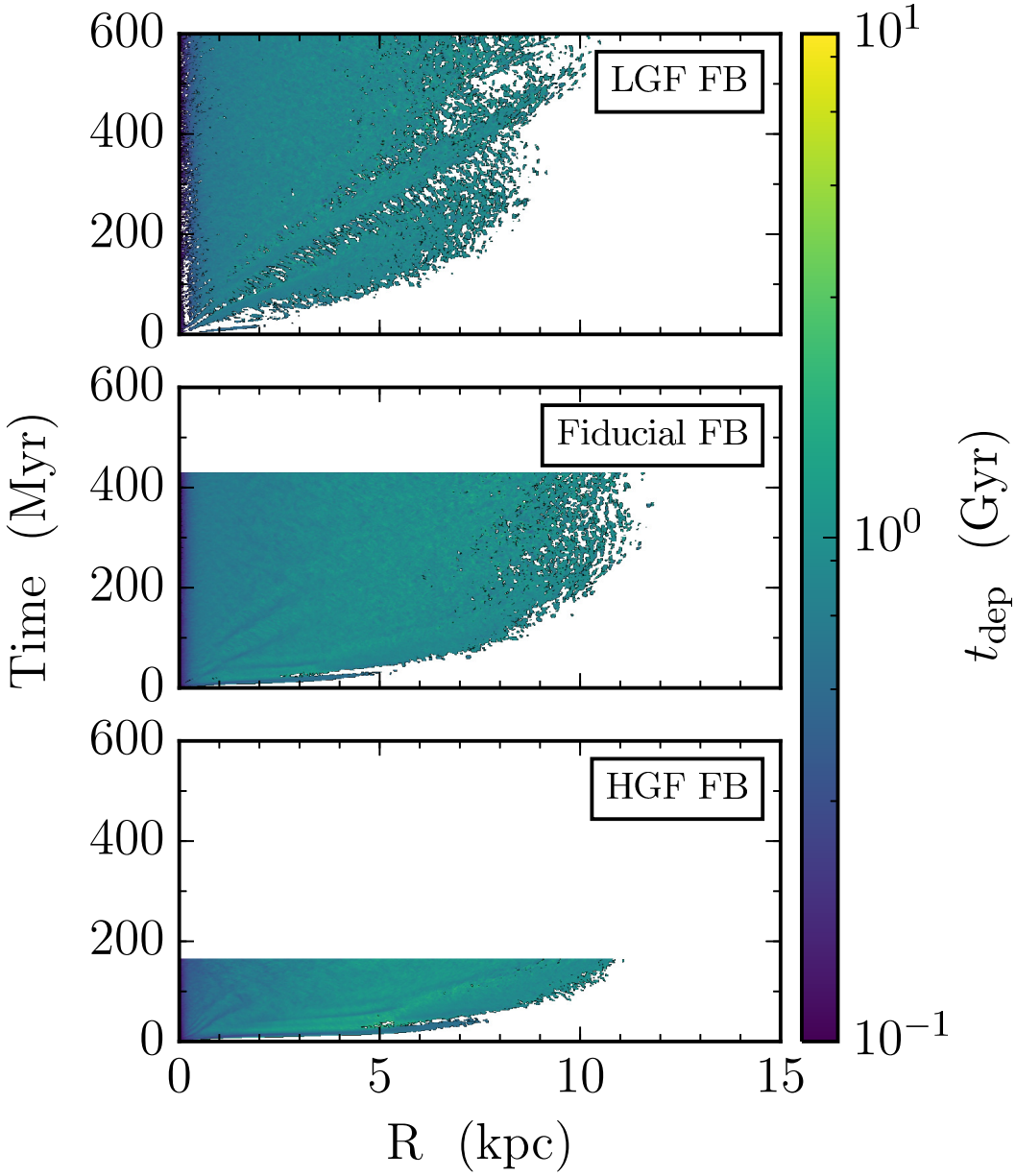

Figure 4.7: The azimuthally averaged gas depletion time ($t_{\rm dep} = \Sigma_{\rm gas}/\Sigma_{SFR}$) as a function of radius and time for all three models that were run with feedback.

have a broadly similar result with $t_{\rm dep} = 1$–2 Gyr throughout most of the star forming disk over the full course of all three simulations. In the core of the galaxy, $t_{\rm dep}$ is lower, ~ 200 Myr. We also note that the time evolution of the azimuthally averaged depletion time shows relatively little structure, particularly in the low gas fraction case. In the fiducial and high gas fraction cases we also see that the depletion time is suppressed somewhat in spiral arms, particularly at early times.

To guide our intuition, we can also directly compare to observations of resolved star formation in nearby galaxies. This is shown in Figure 4.8, which can be directly compared to Figure 4 of Bigiel et al. (2008a). To generate this plot, we first generate maps of the H_2 and H I surface densities by making use of the analytic approximations of Krumholz et al. (2008, 2009); McKee & Krumholz (2010). These approximations are based on detailed calculations of self-shielding in idealized cloud complexes and can predict the molecular gas fraction $f_{H_2} = \Sigma_{H_2}/\Sigma_{\rm gas}$ as a function of $\Sigma_{\rm gas}$ and metallicity. In practice, we use the formula given in Equation 93 of McKee & Krumholz (2010),

$$f_{H_2} = 1 - \frac{0.75s}{1 + 0.25s} \tag{4.4}$$

where

$$s = \frac{\ln 1 + 0.6\chi + 0.01\chi^2}{0.6\tau}, \tag{4.5}$$

$\chi = 0.77(1 + 3.1Z^{0.365})$, $\tau = 0.66Z\Sigma_{\rm gas}/(M_\odot\ {\rm pc}^{-2})$, and Z is the metallicity relative to the solar value. In addition, we generate maps of $\Sigma_{\rm SFR}$ by projecting the expected star formation rate along the z-axis, given our star formation law.

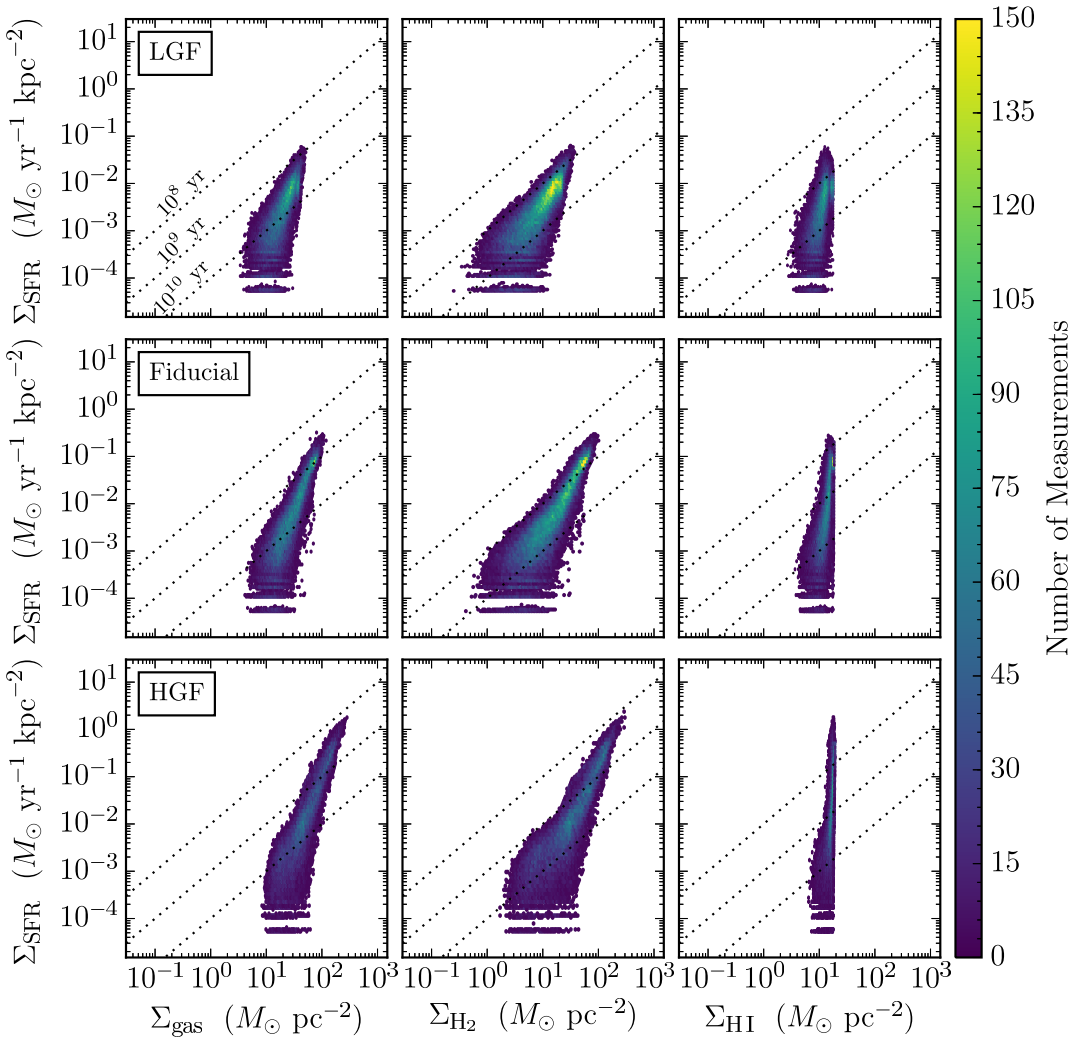

Figure 4.8: The star formation rate surface density as a function of gas (left column) H I (middle column) and H II (right column) surface density. We show data from the low gas fraction (top row), fiducial (middle row) and, high gas fraction (bottom row) models. To guide the eye, we also mark lines of constant depletion time (10^8, 10^9, and 10^{10} years) as a dotted line. Compare with Figure 4 of Bigiel et al. (2008a).

We see that in this formalism f_{H_2} is a function only of the gas surface density, allowing us to immediately calculate

$$\Sigma_{H_2} = f_{H_2}\Sigma_{\rm gas} \tag{4.6}$$

and,

$$\Sigma_{\rm H\ I} = \Sigma_{\rm gas} - \Sigma_{H_2}. \tag{4.7}$$

The latter expression ignores the contribution to the gas surface density of ionized gas, which we will show is a good approximation in subsection 4.3.3.

To directly compare with observations, which are typically done with $\sim$ kpc scale resolution elements (although see Schruba et al., 2010), we degrade the resolution of our surface density maps to 750 pc, matching the resolution of the THINGS survey (Leroy et al., 2008a; Bigiel et al., 2008a). Next, we take each pixel at each simulation time in our degraded resolution surface density maps to be an independent measurement of the surface density of gas, atomic and molecular hydrogen, and the star formation rate. We combine the set of all measurements we infer from all of our simulation snapshots, and create a histogram, which we plot in Figure 4.8.

We see that our simulations fall into a similar region of parameter space for each component as real galaxies. In all three cases, the class Kennicutt-Schmidt law (Kennicutt, 1998; Kennicutt & Evans, 2012), where the total gas surface density is on the x-axis, shows a super-linear scaling, as observed in nearby star forming galaxies. The molecular gas Kennicutt-Schmidt law is shallower, showing a roughly linear scaling

(although perhaps moving to a superlinear scaling at the high gas surface density end), with substantial scatter about $t_{\rm dep} = 2$ Gyr. Lastly, as observed in nearby star forming galaxies, the H I surface density shows no correlation with the surface density of star formation.

In both the fiducial and high gas fraction simulations, we see a transition to a low depletion time mode of star formation at the high gas surface density side of the phase space. This may correspond to a "starburst" mode of star formation (cf. Daddi et al., 2010), or may simply indicate that our feedback prescription is inefficient at destroying high surface density clouds, allowing star formation to proceed there for longer than in lower surface density conditions.

4.3.3 ISM Structure

As we showed in subsection 4.3.1, particularly in Figure 4.5, our feedback model has a dramatic effect on the equilibrium structure of the ISM in our model galaxies. Rather than ending up in a state where the bulk of the gas ends up collecting into massive gravitationally bound clouds, the gas is instead more smoothly distributed throughout the disk, only collecting in large-scale spiral arm patterns.

We can make this statement quantitative by segmenting the gas in our simulated galaxies according to ISM phase. In Figure 4.9, we show an example Temperature-Density phase diagram, with variously ISM phases marged as cross-hatched regions. The regions we identify can primarily be separated into two components: equilibrium and non-equlibrium phases. The former, which include the warm neutral medium (WNM), thermally unstable phase (Unstable), cold neutral medium (CNM), and star forming gas

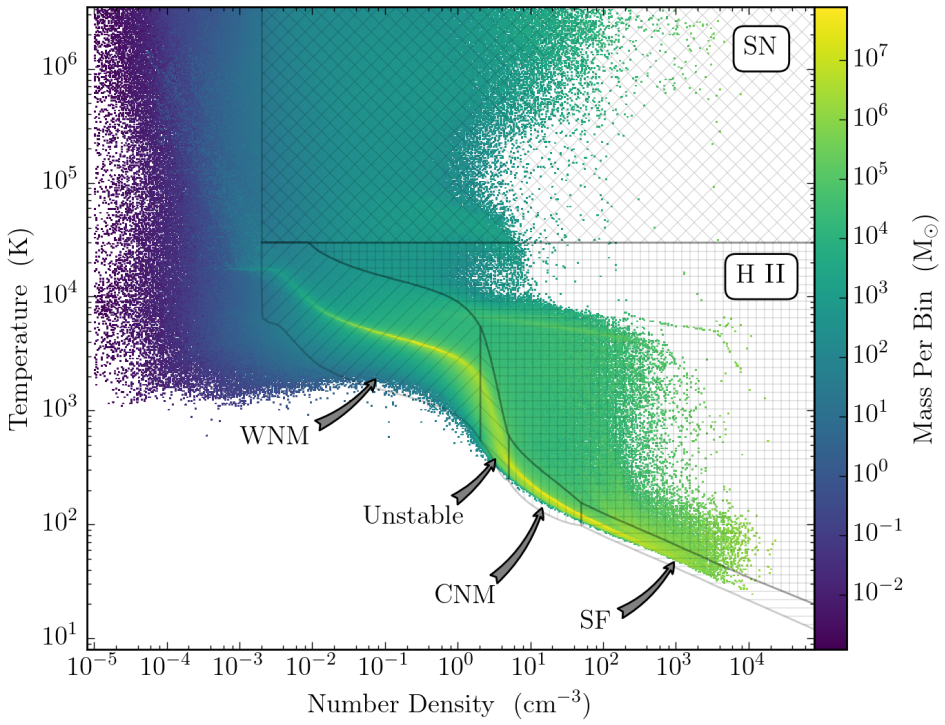

Figure 4.9: A 2D histogram of the gas mass in temperature-density phase space. We indicate the regions of phase space we use to define various components of the ISM.

(SF), all fall along the equilibrium cooling curve, i.e. the region of phase space where at a fixed density cooling (primarily due to metal line emission) and heating (primarily due to thermalization of photoelectrons ejected off of dust grains) exactly balance (Field et al., 1969; Wolfire et al., 2003). In practice, these equilibrium regions have a finite width due to small-scale density and temperature fluctuations, so we also include in a narrow vertical range above and below the equilibrium curve. Non-equilibrium phases, including gas heated by H II region feedback and supernova thermal feedback fall above the equilibrium cooling curve. Note that while we do not explicitly include a prescription for the formation of molecular hydrogen, our star formation threshold corresponds approximately to the transition to the molecular phase, and so our star forming phase can be thought of as corresponding to the molecular gas phase in a real galaxy.

We can quantitatively compare the impact of star formation on the structure of the ISM by finding the gas mass in each ISM component as a function of time for each of our simulated galaxies. The results of this comparison are shown in Figure 4.10. We show simulations with (right column) and without (left column) feedback, for each choice of initial gas fraction. In all three simulations without feedback, the bulk of the gas mass is locked up in dense star forming gas. Over the course of the simulation, this gas is converted into star particles, until eventually the gas supply is exhausted. While there is still substantial gas left at the end of the simulation in the low gas fraction run, the bulk of the gas in fiducial and high gas fraction is converted into stars over the course of the simulation.

The story is markedly different in the simulations with feedback. Rather than

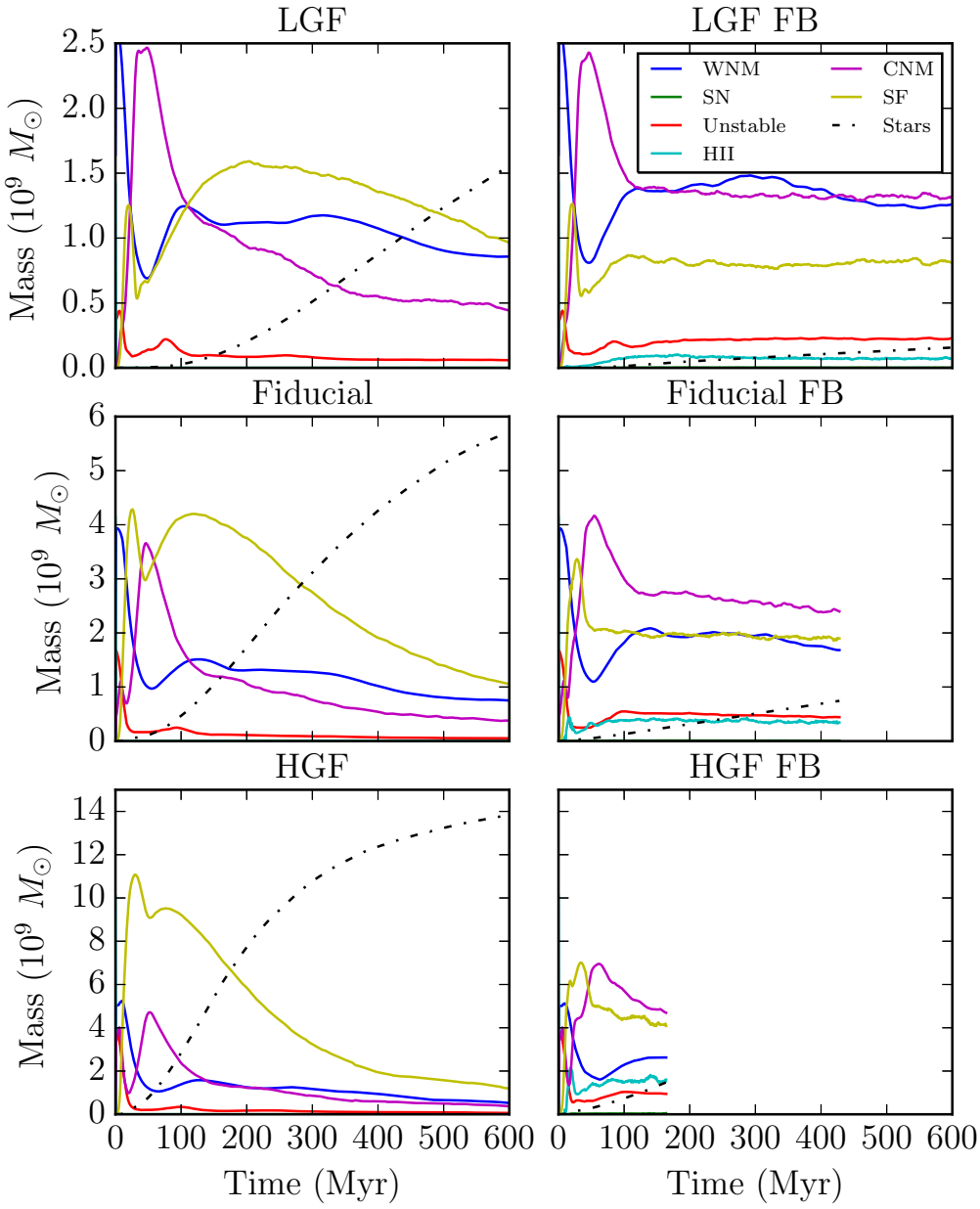

Figure 4.10: The time evolution of the masses of the ISM components depicted in Figure 4.9 (solid lines) along with the mass of dynamically formed stars (dot-dashed line).

being locked up in star forming gas, the bulk of the ISM is is in the WNM or CNM. In the low gas fraction case, the gas is approximately evenly split between WNM and CNM, with a smaller fraction ending up as star forming gas. In the fiducial and high gas fraction cases, the bulk of the gas ends up in the CNM. In both the fiducial and low gas fraction cases, the ISM develops an equilibrium configuration, where the mass of each component is approximately constant over timescales of several hundred Myr. While the mass of gas heated in the H II heated phase is non-negligible in the runs with feedback, this gas is small fraction of the overall mass of the ISM. In all cases the mass of SNe heated gas is negligible. We can also see how the star formation is substantially slower in the runs with feedback, with the stellar mass rising substantially slower than in the runs without feedback.

4.3.4 Gravitational Instability

Here we focus on the gravitational instability that develops in our simulated galaxies. In section 4.3.4, we focus on the velocity structure in the gas. This is followed in section 4.3.4 by a discussion of the evolution of the Toomre Q parameter in our simulated disks, showing how an equilibrium with $Q_{\rm total}$ naturally develops. Lastly, in section 4.3.4, we measure the mean radial mass transport rate, and compare it with the star radially cumulative mean star formation rate.

Velocity Structure

As we showed above, when we include feedback the gas in our simulated galaxies undergoes a cycle of collapse into gravitationally bound clouds, rarefaction due to

supernova feedback, followed by re-collapse. Both supernova explosions and local departures from a purely axisymmetric gravitational potential generate substantial turbulent velocity dispersions. In addition, supernova explosions, winds from massive stars, and H II regions can heat the gas, providing support for the gaseous disk in the form of thermal pressure.

We can see the typical velocity structure in the gaseous disk by inspecting Figure 4.11, where we plot the time average of the gas effective sound speed, sound speed, turbulent velocity dispersion, and the anisotropy in the turbulent velocity dispersion as a function of galactocentric radius. At all radii, $c_{\rm eff} \gtrsim 5$ km/s, reaching as high as 10 km/s at $R = 3$ kpc. In the inner, star forming potion of the disk, the effective sound speed is mostly due to turbulent motions, while the sound speed dominates in the outer disk. In the outskirts, the gas in the outer disk is either in hydrostatic equilibrium and stable to collapse, or does not have sufficient time to go thermally unstable, cool, and collapse. Compared to the simulations without feedback, the effective sound speed is somewhat *lower*, perhaps surprisingly as the turbulent velocity dispersions of disk galaxies are often thought to be *due* to feedback.

On the other hand, a major effect of feedback is to make the turbulent velocity field isotropic across the bulk of our simulated galaxies. The turbulent motions are isotropic, with $\sqrt{2}\sigma_{v,z}/\sigma_{v,d} \simeq 1$ at all radii. We can also see this as a function of time in Figure 4.12. The isotropic turbulent velocity dispersions seen in the runs with feedback leads to substantially larger gas scale heights in these simulations. Rather than all of the gas collapsing into an extreme 2D disk, instead gas extends both above and below

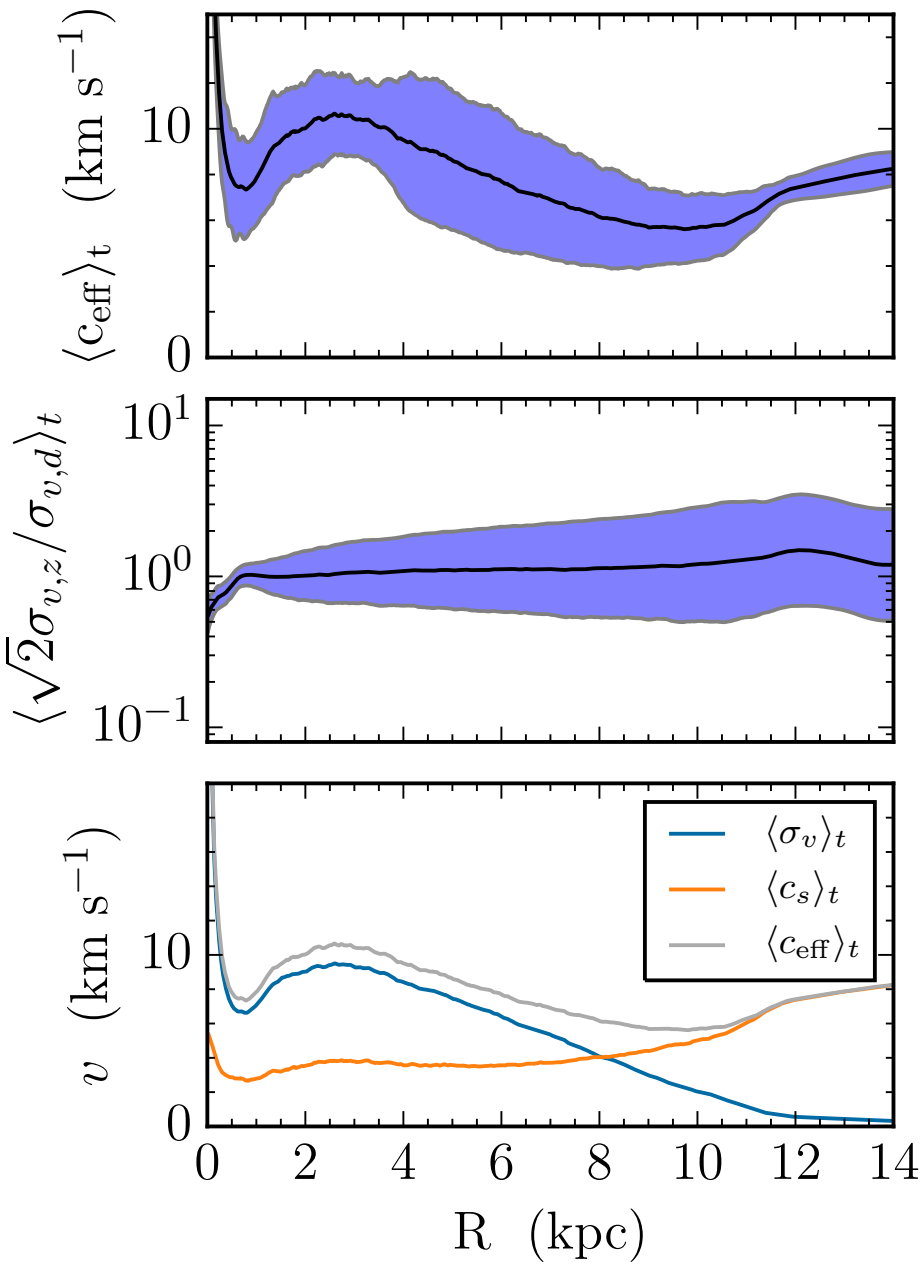

Figure 4.11: The time-averaged gas effective sound speed in the fiducial simulation (top panel), time-averaged velocity dispersion anisotropy (middle panel), and the contribution to the effective sound speed by the velocity dispersion and thermal sound speed (bottom panel). The blue shaded regions in the top two panels indicate 1-σ variance of the plotted quantity as a function radius.

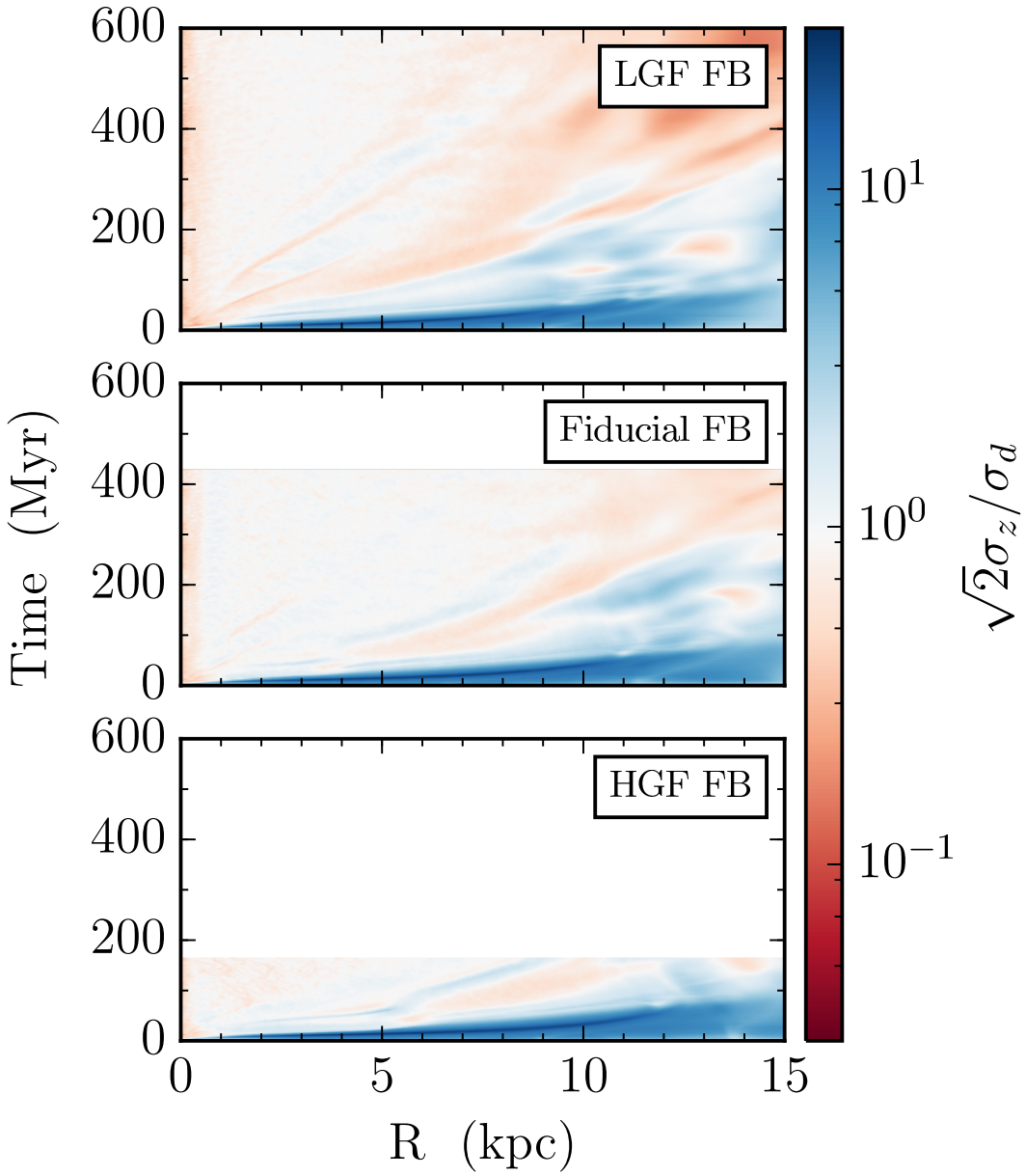

Figure 4.12: The gas velocity dispersion anisotropy as a function of radius and time for all three models.

the disk as it gets thrown out of the midplane by feedback. Typically, we find scale heights of several hundred parsecs throughout the bulk of the disks.

Toomre Q

The susceptibility of a disk to gravitational instability can be characterized via the Toomre Q parameter. We are able to calculate a combined $Q_{\rm total}$ that includes the separate contribution to the stability of the disk from both gas and stars, and accounts for the finite thickness of the gaseous and stellar disks (Romeo & Wiegert, 2011). We found above in the runs with no feedback, that the gaseous component drives $Q_{\rm total}$ to ever-increasing values as the simulation proceeds. We concluded that was primarily due to the exhaustion of gas.

We see from Figure 4.13 that in our runs including stellar feedback, $Q_{\rm total}$ is remarkably stable, showing little variation with radius or time. There is some modulation at the factor-of-two level due to surface density fluctuations — transient rings early in the simulation and spiral density waves later on — but we do not see order of magnitude variations as in the runs without feedback.

Stellar feedback is able to slow down the runaway gravitational instability that would otherwise take hold by efficiently destroying gravitationally bound clouds. The disk attains a quasi-stable state, with $Q_{\rm total} \gtrsim 1$ throughout the disk. Both the gaseous and stellar components show remarkably little variation over the course of the simulation, as we see in Figure 4.14. The gaseous and stellar surface density profile remain smooth, varying exponentially with radius.

We see that stellar feedback is necessary to prevent the runaway fragmenta-

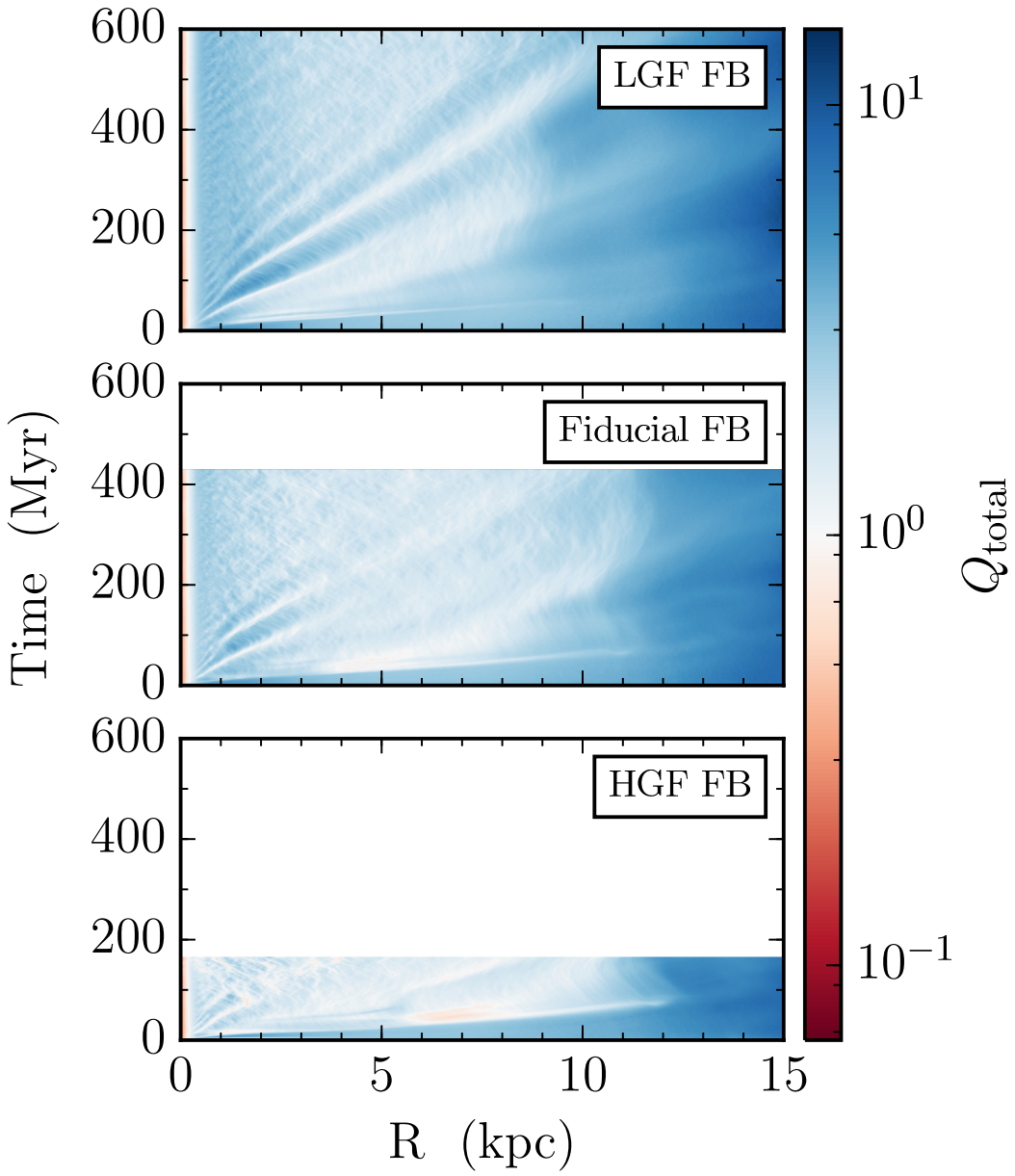

Figure 4.13: The combined Toomre Q parameter as a function of radius and time.

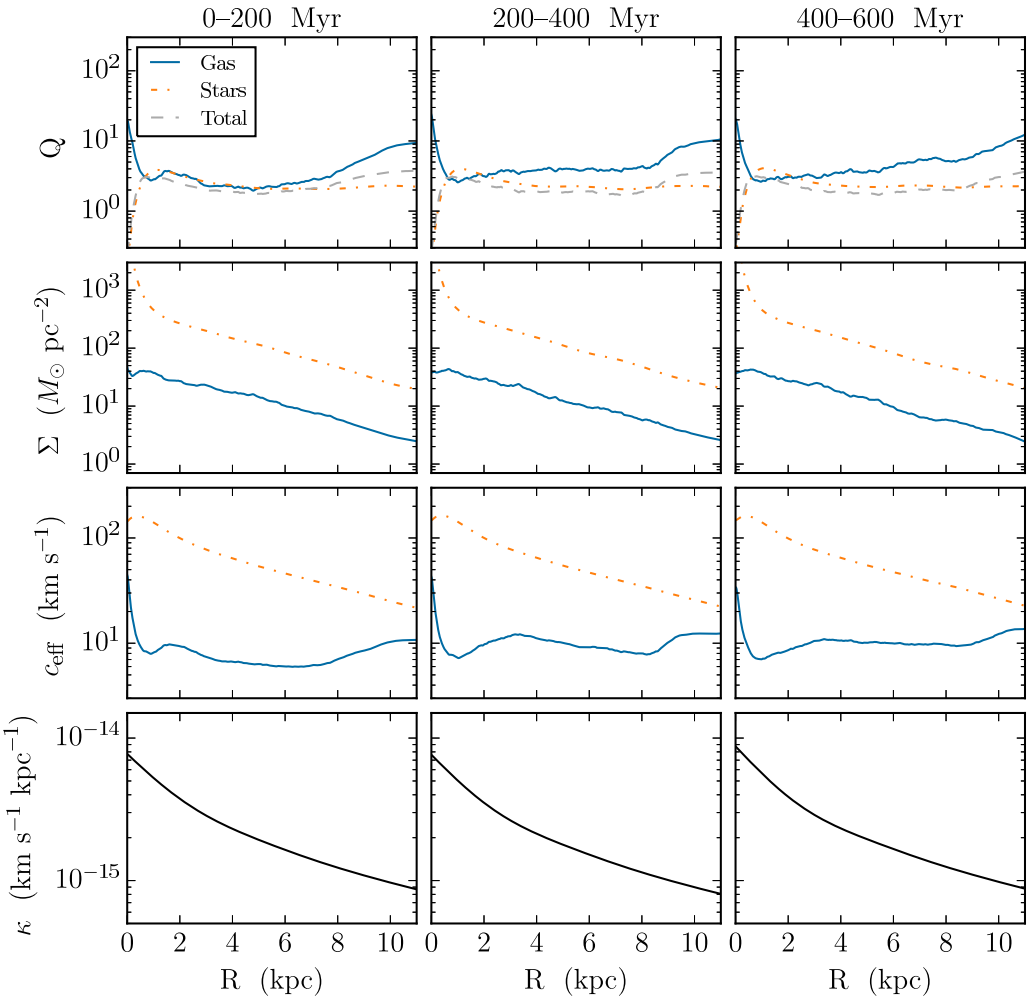

Figure 4.14: The gas, stellar, and total Toomre Q parameter (top row), gas and stellar surface density (second row), gas and stellar effective sound speed (third row) and epicyclic frequency (bottom row) for the low gas fraction simulation.

tion of star forming gaseous disks, although the story is somewhat different from the naive expectation that feedback drives turbulence. Instead, feedback moderates the consumption of gas, keeping $Q_{\rm total}$ close to one, rather than being driven to a high value by the exhaustion of gas. Feedback also prevents gas from reaching $Q_{\rm total} \lesssim 1$, since any substantial accumulation of gas is efficiently destroyed by supernova blastwaves.

Mass Transport

Finally, we focus on the radial mass transport rate in the gaseous disk. In the simulations without feedback, we found that mass transport was dominated by N-body migration of individual giant clumps. We also found that there was a net radial inflow of gas, but that this flow was insufficient to supply the rapid star formation in the wildly gravitationally unstable disks.

The runs with star formation feedback show a very different history. In Figure 4.15, we show the time evolution of the radial mass flux. Compared to the runs without feedback, the early evolution is similar. At early times, the gas mass flux is dominated by rings of inward and outward flux. Since we are mostly interested in the behavior of the disks after they have settled down into statistical equilibrium, we do not consider the portions of radius-time phase space that are strongly influenced by initial transients (indicated by the blue lines in Figure 4.15. In the inner disk ($R \lesssim 1.5$ kpc) of the low gas fraction and fiducial cases, mass transport is effective suppressed. At intermediate radii 1.5 kpc $\lesssim R \lesssim 8$ kpc, the mass flux shows alternating patterns of inward and outward flux, which we associate with the formation of spiral arms. We can't say whether the high gas fraction case shows similar behavior, since it has not

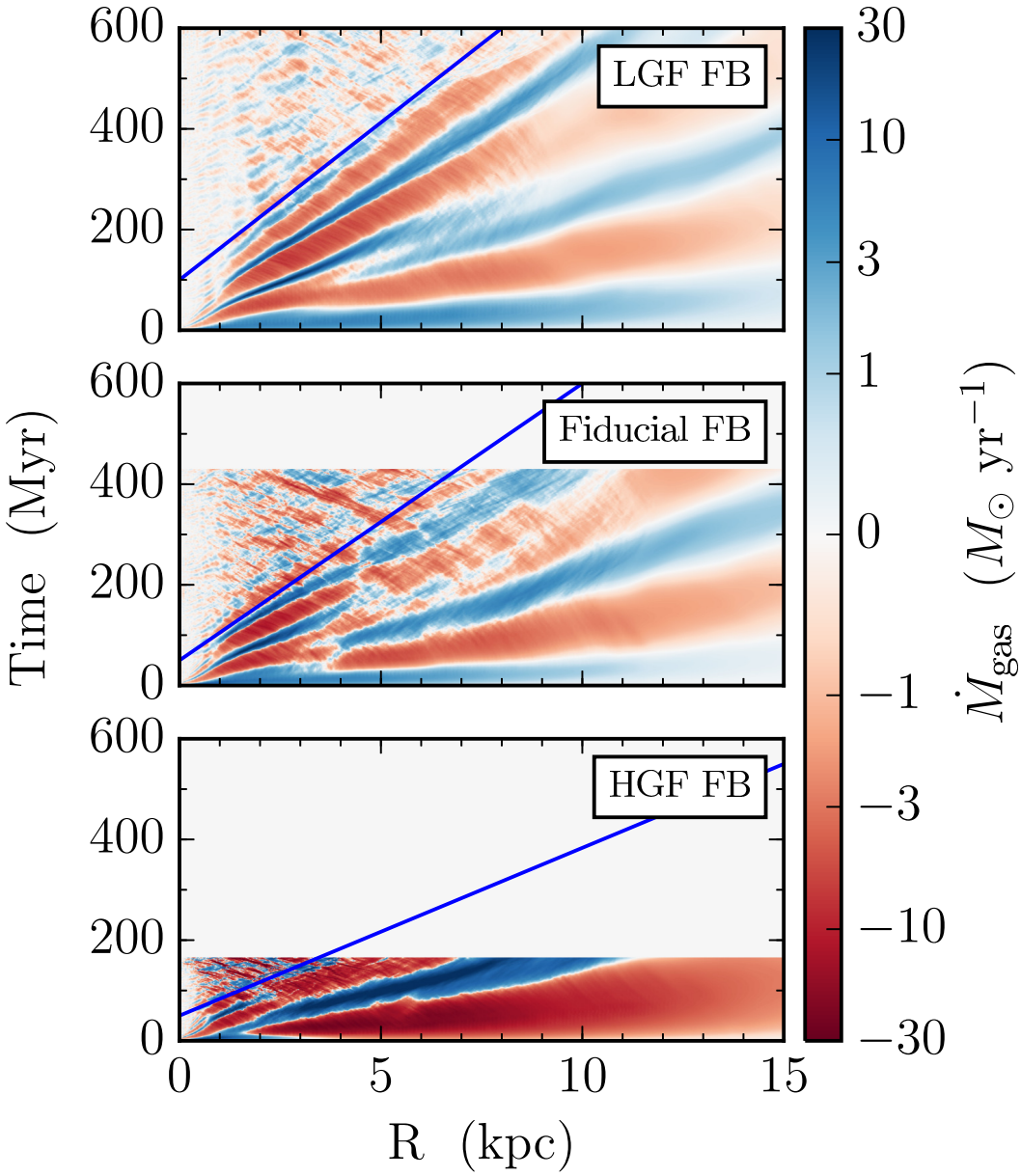

Figure 4.15: The radial mass flux as a function of radius and time. The blue lines indicate the wedge averaging region used to produce Figure 4.11 and Figure 4.16.

run long enough, although we see hints that there is substantial throughout the star forming disk.

Lastly, we have calculated the average mass flux and radially cumulative star star formation rate, which we present in Figure 4.16. We show the *negative* radially cumulative mean star formation rate to guide the eye. At a fixed radius, if the radially cumulative star formation rate is equal to a net inward mass flux, then the mass flux at that radius is sufficient to supply all of the star formation within that radius. For the low gas fraction simulation, we see that over the bulk of the star forming disk ($R \lesssim 5$ kpc), radial mass transport is sufficient to supply the bulk of the star formation. For the fiducial simulation, it is only enough to supply the star formation for $R \lesssim 2$ kpc. Beyond that radius, the gas will be consumed faster than it can be replaced by gas moving in from larger radii. We caution that the net mass flux result for the fiducial simulation is still preliminary since the simulation has not been run to completion. Especially in the other disk, we are sampling $\lesssim 100$ Myr of simulation time, and it is possible that later in the simulation the average mass flux converges to a larger inward flux value.

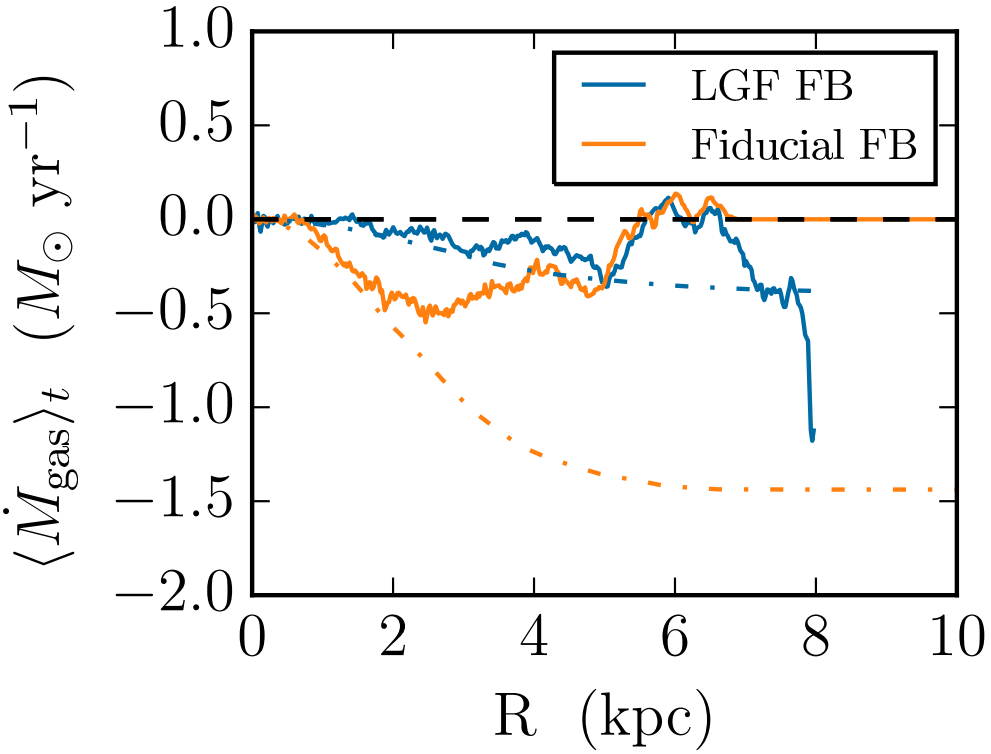

Figure 4.16: The time-averaged radius mass flux as a function of radius for the low gas fraction (blue line) and fiducial (orange line) simulations. We plot the negative one times the time-averaged radially accumulated star formation rate in the background using a dot-dashed line.

4.4 Conclusions

In this chapter we have presented three simulations of Milky Way-like disk galaxies under the influence of gravitational instability and star formation feedback. We found that feedback substantially alters the structure of our model galaxies, producing some major differences relative to the simulations without feedback.

In particular, we find

- Feedback redistributes gas from gravitationally bound clouds into the WNM and CNM, producing an overall smoother ISM structure where gas is more evenly distributed at all radii and all density scales.

- Gravitational Insbility and feedback drive substantial turbulent velocity dispersions, with $\sigma_v > c_s$ throughout the bulk of the portions of our model galaxies that actively form stars.

- Feedback moderates star formation, suppressing the star formation rate by up to a factor of 5, and producing disks where $t_{\rm dep} \sim 2$ Gyr, matching observed depletion times in nearby star forming galaxies.

- The gravitational instability proceeds more slowly in models including feedback, maintains $Q_{\rm total} \sim 2$ for hundreds of millions of years throughout the bulk of our simulated disks.

- We find there is a net inflow of gas due to torques driven by gravitational instability. The radial inflow is at a lower rate than in the simulations without feedback. For the low gas fraction gas, we find that radial infall is sufficient to resupply gas

to the inner disk as it is exhausted by star formation. For the fiducial model, it is insufficient, but can still a replace a substantial fraction of the gas lost to star formation.

Bibliography

Abdo, A. A., Ackermann, M., Ajello, M., et al. 2010, ApJ, 710, 133 [2.7.1]

Abel, T., Bryan, G. L., & Norman, M. L. 2002, Science, 295, 93 [2.4.5]

Agertz, O., Lake, G., Teyssier, R., et al. 2009, MNRAS, 392, 294 [1.2, 3.6.1]

Agertz, O., Romeo, A. B., & Grisdale, K. 2015, MNRAS, 449, 2156 [1.2, 3.1, 3.6.1]

Alves, D. R. 2004, New A Rev., 48, 659 [2.7.2]

Ballesteros-Paredes, J. 2006, MNRAS, 372, 443 [2.8.3]

Ballesteros-Paredes, J., Hartmann, L., & Vázquez-Semadeni, E. 1999, ApJ, 527, 285 [1.3]

Ballesteros-Paredes, J., Hartmann, L. W., Vázquez-Semadeni, E., Heitsch, F., & Zamora-Avilés, M. A. 2011, MNRAS, 411, 65 [2.8.3]

Balser, D. S., Rood, R. T., Bania, T. M., & Anderson, L. D. 2011, ApJ, 738, 27 [1.1]

Behroozi, P. S., Wechsler, R. H., & Conroy, C. 2013, ApJ, 762, L31 [1.1, 3.6.2]

Bertin, G., & Lodato, G. 1999, A&A, 350, 694 [1.2]

Bertin, G., & Romeo, A. B. 1988, A&A, 195, 105 [1.2]

Bertoldi, F., & McKee, C. F. 1992, ApJ, 395, 140 [2.4.2, 2.7.1, 2.7.1]

Bica, E., Claria, J. J., Dottori, H., Santos, Jr., J. F. C., & Piatti, A. E. 1996, ApJS,

102, 57 [2.7.2, 2.7.2]

Bigiel, F., & Blitz, L. 2012, ApJ, 756, 183 [1.1]

Bigiel, F., Leroy, A., Walter, F., et al. 2010, AJ, 140, 1194 [3.6.2]

—. 2008a, AJ, 136, 2846 [1.1, 4.3.2, 4.3.2, 4.8, 4.3.2]

—. 2008b, AJ, 136, 2846 [1.3, 2.4.5]

Bigiel, F., Leroy, A. K., Walter, F., et al. 2011, ApJ, 730, L13 [4.3.2]

Binney, J., & Tremaine, S. 2008, Galactic Dynamics: Second Edition [3.3.2]

Blitz, L., Fukui, Y., Kawamura, A., et al. 2007, Protostars and Planets V, 81 [2.1, 2.7.1, 2.7.1, 2.6, 2.7.1]

Blitz, L., & Shu, F. H. 1980, ApJ, 238, 148 [1.3]

Bolatto, A. D., Leroy, A. K., Rosolowsky, E., Walter, F., & Blitz, L. 2008, ApJ, 686, 948 [2.4.1, 2.7.1, 2.7.1, 2.7.1, 2.8.3]

Bouché, N., Dekel, A., Genzel, R., et al. 2010, ApJ, 718, 1001 [1.1, 3.6.2]

Bournaud, F., & Elmegreen, B. G. 2009, ApJ, 694, L158 [3.6.2]

Bournaud, F., Elmegreen, B. G., Teyssier, R., Block, D. L., & Puerari, I. 2010, MNRAS, 409, 1088 [1.2, 3.6.1]

Bresolin, F., Kennicutt, R. C., & Ryan-Weber, E. 2012, ApJ, 750, 122 [1.1]

Bresolin, F., Ryan-Weber, E., Kennicutt, R. C., & Goddard, Q. 2009, ApJ, 695, 580 [1.1]

Brunt, C. M., Heyer, M. H., & Mac Low, M.-M. 2009, A&A, 504, 883 [2.4.3, 2.1]

Bryan, G. L., Norman, M. L., Stone, J. M., Cen, R., & Ostriker, J. P. 1995, Computer Physics Communications, 89, 149 [3.2.2]

Cen, R., & Ostriker, J. P. 1992, ApJ, 399, L113 [3.2.4, 4.2.2]

Chomiuk, L., & Povich, M. S. 2011, AJ, 142, 197 [3.5.2]

Cioffi, D. F., McKee, C. F., & Bertschinger, E. 1988, ApJ, 334, 252 [4.2.2]

Colella, P., & Woodward, P. R. 1984, Journal of Computational Physics, 54, 174 [3.2.2]

Condon, J. J. 1992, ARA&A, 30, 575 [2.7.2]

Cresci, G., Hicks, E. K. S., Genzel, R., et al. 2009, ApJ, 697, 115 [3.6.2]

Croxall, K. V., van Zee, L., Lee, H., et al. 2009, ApJ, 705, 723 [1.1]

Daddi, E., Dickinson, M., Morrison, G., et al. 2007, ApJ, 670, 156 [1.1]

Daddi, E., Elbaz, D., Walter, F., et al. 2010, ApJ, 714, L118 [4.3.2]

Dekel, A., Sari, R., & Ceverino, D. 2009a, ApJ, 703, 785 [3.6.2]

Dekel, A., Birnboim, Y., Engel, G., et al. 2009b, Nature, 457, 451 [1.1]

Dickel, J. R., McIntyre, V. J., Gruendl, R. A., & Milne, D. K. 2005, AJ, 129, 790 [2.7.2, 2.7.2, 2.7.2]

Dobbs, C. L., Bonnell, I. A., & Pringle, J. E. 2006, MNRAS, 371, 1663 [1.2, 3.2.2]

Dobbs, C. L., Burkert, A., & Pringle, J. E. 2011, MNRAS, 413, 2935 [2.4.5]

Dobbs, C. L., Pringle, J. E., & Duarte-Cabral, A. 2015, MNRAS, 446, 3608 [1.2]

Draine, B. T. 2011, Physics of the Interstellar and Intergalactic Medium [3.2.5]

Elbaz, D., Daddi, E., Le Borgne, D., et al. 2007, A&A, 468, 33 [1.1]

Elmegreen, B. G., & Scalo, J. 2004, ARA&A, 42, 211 [1.3]

Engargiola, G., Plambeck, R. L., Rosolowsky, E., & Blitz, L. 2003, ApJS, 149, 343 [2.4.1, 2.4.5]

Evans, II, N. J., Dunham, M. M., Jørgensen, J. K., et al. 2009, ApJS, 181, 321 [2.4.2]

Falgarone, E., Troland, T. H., Crutcher, R. M., & Paubert, G. 2008, A&A, 487, 247 [2.8.2]

Fall, S. M., Krumholz, M. R., & Matzner, C. D. 2010, ApJ, 710, L142 [2.4.7, 2.6.2]

Faucher-Giguère, C.-A., Quataert, E., & Hopkins, P. F. 2013, MNRAS, 433, 1970 [3.6.1]

Ferguson, A. M. N., & Clarke, C. J. 2001, MNRAS, 325, 781 [1.2]

Field, G. B., Goldsmith, D. W., & Habing, H. J. 1969, ApJ, 155, L149 [4.3.3]

Forbes, J., Krumholz, M., & Burkert, A. 2012, ApJ, 754, 48 [1.2]

Forbes, J. C., Krumholz, M. R., Burkert, A., & Dekel, A. 2014a, MNRAS, 438, 1552 [1.2]

—. 2014b, MNRAS, 443, 168 [1.1, 3.6.2]

Fraternali, F., Marasco, A., Marinacci, F., & Binney, J. 2013, ApJ, 764, L21 [1.1]

Fujimoto, Y., Tasker, E. J., & Habe, A. 2014a, MNRAS, 445, L65 [1.2]

Fujimoto, Y., Tasker, E. J., Wakayama, M., & Habe, A. 2014b, MNRAS, 439, 936 [1.2]

Fukui, Y., & Kawamura, A. 2010, ARA&A, 48, 547 [1.3, 2.4.5, 2.7.2]

Fukui, Y., Kawamura, A., Minamidani, T., et al. 2008, ApJS, 178, 56 [2.7.2]

Genzel, R., Burkert, A., Bouché, N., et al. 2008, ApJ, 687, 59 [3.6.2]

Glover, S. C. O., Federrath, C., Mac Low, M.-M., & Klessen, R. S. 2010, MNRAS, 404, 2 [2.7.1]

Goldbaum, N. J., Krumholz, M. R., & Forbes, J. C. 2015, in prep.a, ApJ [(document)]

—. 2015, in prep.b, ApJ [(document)]

Goldbaum, N. J., Krumholz, M. R., Matzner, C. D., & McKee, C. F. 2011, ApJ, 738, 101 [(document)]

Goldreich, P., & Kwan, J. 1974, ApJ, 189, 441 [1.3]

Green, A. W., Glazebrook, K., McGregor, P. J., et al. 2010, Nature, 467, 684 [3.6.1]

Guedes, J., Callegari, S., Madau, P., & Mayer, L. 2011, ApJ, 742, 76 [3.2.4]

Heiles, C., & Troland, T. H. 2005, ApJ, 624, 773 [2.8.2]

Henry, R. B. C., Kwitter, K. B., Jaskot, A. E., et al. 2010, ApJ, 724, 748 [1.1]

Hernquist, L. 1990, ApJ, 356, 359 [3.2.1]

Heyer, M., Krawczyk, C., Duval, J., & Jackson, J. M. 2009, ApJ, 699, 1092 [2.4.1, 2.1, 2.7.1]

Heyer, M. H., & Brunt, C. M. 2004, ApJ, 615, L45 [2.4.3]

Heyer, M. H., Carpenter, J. M., & Snell, R. L. 2001, ApJ, 551, 852 [1.3, 2.4.1, 2.4.5]

Ho, I.-T., Kudritzki, R.-P., Kewley, L. J., et al. 2015, MNRAS, 448, 2030 [1.1]

Hobbs, A., Read, J., Power, C., & Cole, D. 2013, MNRAS, 434, 1849 [1.1]

Hockney, R. W., & Eastwood, J. W. 1988, [3.2.2]

Hopkins, P. F., Quataert, E., & Murray, N. 2012, MNRAS, 421, 3488 [1.2, 3.4]

Hughes, A., Staveley-Smith, L., Kim, S., Wolleben, M., & Filipović, M. 2007, MNRAS, 382, 543 [2.7.2]

Hughes, A., Wong, T., Ott, J., et al. 2010, MNRAS, 406, 2065 [2.4.1, 2.7.1, 2.7.2, 2.7.2]

Hunter, C. 1977, ApJ, 218, 834 [2.4.5]

Ianjamasimanana, R., de Blok, W. J. G., Walter, F., & Heald, G. H. 2012, AJ, 144, 96 [1.1]

Ianjamasimanana, R., de Blok, W. J. G., Walter, F., et al. 2015, AJ, arXiv:1506.04156, in press, arXiv:1506.04156 [1.1]

Imara, N., Bigiel, F., & Blitz, L. 2011, ApJ, 732, 79 [2.4.5]

Jog, C. J., & Solomon, P. M. 1984a, ApJ, 276, 127 [1.2]

—. 1984b, ApJ, 276, 114 [1.2]

Joung, M. K. R., & Mac Low, M.-M. 2006, ApJ, 653, 1266 [4.2.2, 4.2.2]

Kalberla, P. M. W., & Dedes, L. 2008, A&A, 487, 951 [2.4.5]

Katz, N. 1992, ApJ, 391, 502 [4.2.2]

Kawamura, A., Mizuno, Y., Minamidani, T., et al. 2009, ApJS, 184, 1 [2.7.2, 2.8, 2.7.2, 2.7.2, 2.9]

Kegel, W. H. 1989, A&A, 225, 517 [2.8.3]

Kennicutt, R. C., & Evans, N. J. 2012, ARA&A, 50, 531 [1.1, 4.3.2]

Kennicutt, Jr., R. C. 1998, ApJ, 498, 541 [4.3.2]

Kennicutt, Jr., R. C., & Hodge, P. W. 1986, ApJ, 306, 130 [2.7.2]

Kennicutt, Jr., R. C., Calzetti, D., Walter, F., et al. 2007, ApJ, 671, 333 [1.3]

Kereš, D., Katz, N., Weinberg, D. H., & Davé, R. 2005, MNRAS, 363, 2 [1.1]

Kim, C.-G., Kim, W.-T., & Ostriker, E. C. 2011a, ApJ, 743, 25 [4.2.2, 4.2.2]

Kim, C.-G., & Ostriker, E. C. 2015, ApJ, 802, 99 [4.2.2, 4.2.2]

Kim, J.-h., Wise, J. H., Alvarez, M. A., & Abel, T. 2011b, ApJ, 738, 54 [4.2.2]

Kim, J.-h., Abel, T., Agertz, O., et al. 2014, ApJS, 210, 14 [1.2, 3.2.1, 3.2.4, 3.2.5]

Kim, W.-T., & Ostriker, E. C. 2006, ApJ, 646, 213 [1.3]

Kim, W.-T., Ostriker, E. C., & Stone, J. M. 2002, ApJ, 581, 1080 [1.3]

—. 2003, ApJ, 599, 1157 [1.1, 1.3]

Klessen, R. S., & Hennebelle, P. 2010, A&A, 520, A17 [1.3, 2.6.2]

Kroupa, P. 2002, Science, 295, 82 [2.4.4]

Krumholz, M., & Burkert, A. 2010, ApJ, 724, 895 [1.2]

Krumholz, M. R., Dekel, A., & McKee, C. F. 2012, ApJ, 745, 69 [3.2.4]

Krumholz, M. R., Leroy, A. K., & McKee, C. F. 2011, ApJ, 731, 25 [2.8.3]

Krumholz, M. R., & Matzner, C. D. 2009, ApJ, 703, 1352 [1.3, 2.4.4]

Krumholz, M. R., Matzner, C. D., & McKee, C. F. 2006, ApJ, 653, 361 [1.3, 2.2]

Krumholz, M. R., & McKee, C. F. 2005, ApJ, 630, 250 [2.4.4, 2.1]

Krumholz, M. R., McKee, C. F., & Tumlinson, J. 2008, ApJ, 689, 865 [2.4.5, 2.7.2, 4.3.2]

—. 2009, ApJ, 693, 216 [4.3.2]

Krumholz, M. R., & Tan, J. C. 2007a, ApJ, 654, 304 [2.4.4]

—. 2007b, ApJ, 654, 304 [3.2.4]

Lada, C. J., Lombardi, M., & Alves, J. F. 2010, ApJ, 724, 687 [2.4.2]

Larson, R. B. 1981, MNRAS, 194, 809 [2.4.1, 2.7.1, 2.7.1]

Leitherer, C., Ekström, S., Meynet, G., et al. 2014, ApJS, 212, 14 [4.2.2]

Leitherer, C., Schaerer, D., Goldader, J. D., et al. 1999, ApJS, 123, 3 [4.2.2]

Leitner, S. N., & Kravtsov, A. V. 2011, ApJ, 734, 48 [1.1]

Lejeune, T., & Schaerer, D. 2001, A&A, 366, 538 [2.7.2]

Leroy, A., Bolatto, A., Stanimirovic, S., et al. 2007, ApJ, 658, 1027 [2.7.1]

Leroy, A. K., Walter, F., Brinks, E., et al. 2008a, AJ, 136, 2782 [1.1, 4.3.2]

—. 2008b, AJ, 136, 2782 [2.4.5]

Leroy, A. K., Walter, F., Sandstrom, K., et al. 2013, AJ, 146, 19 [1.1, 3.5.2, 4.3.2]

Li, H., Griffin, G. S., Krejny, M., et al. 2006a, ApJ, 648, 340 [2.8.2]

Li, Y., Mac Low, M.-M., & Klessen, R. S. 2006b, ApJ, 639, 879 [1.3]

Li, Z.-Y., & Nakamura, F. 2006, ApJ, 640, L187 [1.3, 2.6.2]

Li, Z.-Y., Wang, P., Abel, T., & Nakamura, F. 2010, ApJ, 720, L26 [1.3]

Lilly, S. J., Carollo, C. M., Pipino, A., Renzini, A., & Peng, Y. 2013, ApJ, 772, 119 [1.1, 3.6.2]

Lin, C. C., & Shu, F. H. 1966, Proceedings of the National Academy of Science, 55, 229 [1.2]

Lin, D. N. C., & Pringle, J. E. 1987a, MNRAS, 225, 607 [1.2]

—. 1987b, ApJ, 320, L87 [1.2]

Lombardi, M., Alves, J., & Lada, C. J. 2010, A&A, 519, L7 [2.8.3]

Lopez, L. A., Krumholz, M. R., Bolatto, A. D., Prochaska, J. X., & Ramirez-Ruiz, E. 2011, ApJ, 731, 91 [2.4.4]

Mac Low, M.-M., & Klessen, R. S. 2004, Reviews of Modern Physics, 76, 125 [1.3, 2.6.2]

Mac Low, M.-M., Klessen, R. S., Burkert, A., & Smith, M. D. 1998, Physical Review Letters, 80, 2754 [1.3, 2.4.3]

Marinacci, F., Binney, J., Fraternali, F., et al. 2010, MNRAS, 404, 1464 [1.1]

Matzner, C. D. 2001, in Astronomical Society of the Pacific Conference Series, Vol. 243, From Darkness to Light: Origin and Evolution of Young Stellar Clusters, ed. T. Montmerle & P. André, 757 [2.4.1]

Matzner, C. D. 2002, ApJ, 566, 302 [1.3, 2.4.3, 2.4.4, 2.4.4, 2.6.2]

Matzner, C. D., & McKee, C. F. 2000, ApJ, 545, 364 [2.4.7]

McKee, C. F. 1989, ApJ, 345, 782 [1.3, 2.4.1, 2.4.3]

McKee, C. F. 1999, in NATO Advanced Science Institutes (ASI) Series C, Vol. 540, NATO Advanced Science Institutes (ASI) Series C, ed. C. J. Lada & N. D. Kylafis, 29 [2.4.2, 2.1]

McKee, C. F., & Krumholz, M. R. 2010, ApJ, 709, 308 [4.3.2]

McKee, C. F., & Ostriker, E. C. 2007, ARA&A, 45, 565 [1.3, 2.8.2]

McKee, C. F., & Tan, J. C. 2003, ApJ, 585, 850 [2.3, 2.4.5]

McKee, C. F., & Williams, J. P. 1997, ApJ, 476, 144 [2.4.1, 2.1, 2.7.2]

McKee, C. F., & Zweibel, E. G. 1992, ApJ, 399, 551 [2.2, 2.2, 2.4.1, 2.4.2]

Meynet, G., Maeder, A., Schaller, G., Schaerer, D., & Charbonnel, C. 1994, A&AS, 103, 97 [2.7.2]

Mitra, S., Davé, R., & Finlator, K. 2014, ArXiv e-prints, arXiv:1411.1157 [1.1, 3.6.2]

Mizuno, N., Rubio, M., Mizuno, A., et al. 2001, PASJ, 53, L45 [2.4.1]

Mo, H. J., Mao, S., & White, S. D. M. 1998, MNRAS, 295, 319 [3.2.1, 4.2.1]

Moster, B. P., Naab, T., & White, S. D. M. 2013, MNRAS, 428, 3121 [1.1]

Murray, N. 2011, ApJ, 729, 133 [1.3]

Navarro, J. F., Frenk, C. S., & White, S. D. M. 1996, ApJ, 462, 563 [3.2.1]

Noeske, K. G., Weiner, B. J., Faber, S. M., et al. 2007, ApJ, 660, L43 [1.1]

Norman, C., & Silk, J. 1980, ApJ, 238, 158 [1.3]

Olivier, S. S., Primack, J. R., & Blumenthal, G. R. 1991, MNRAS, 252, 102 [1.2]

Onodera, S., Kuno, N., Tosaki, T., et al. 2010, ApJ, 722, L127 [1.3]

Ossenkopf, V., & Mac Low, M.-M. 2002, A&A, 390, 307 [2.4.3]

Parravano, A., Hollenbach, D. J., & McKee, C. F. 2003, ApJ, 584, 797 [2.7.2, 4.2.2]

Petric, A. O., & Rupen, M. P. 2007, AJ, 134, 1952 [1.1]

Pilyugin, L. S., Vílchez, J. M., & Contini, T. 2004, A&A, 425, 849 [1.1]

Piontek, R. A., & Ostriker, E. C. 2004, ApJ, 601, 905 [1.1]

—. 2005, ApJ, 629, 849 [1.1]

—. 2007, ApJ, 663, 183 [1.1]

Portinari, L., & Chiosi, C. 2000, A&A, 355, 929 [1.1]

Regan, M. W., Thornley, M. D., Helfer, T. T., et al. 2001, ApJ, 561, 218 [1.1]

Renaud, F., Bournaud, F., Emsellem, E., et al. 2013, MNRAS, 436, 1836 [1.2]

Roman-Duval, J., Jackson, J. M., Heyer, M., Rathborne, J., & Simon, R. 2010, ApJ, 723, 492 [1.3]

Romeo, A. B., & Wiegert, J. 2011, MNRAS, 416, 1191 [1.2, 3.3.6, 4.3.4]

Rosolowsky, E. 2005, PASP, 117, 1403 [1.3]

—. 2007, ApJ, 654, 240 [1.3, 2.4.1]

Rosolowsky, E., & Leroy, A. 2006, PASP, 118, 590 [2.7.1]

Saintonge, A., Kauffmann, G., Wang, J., et al. 2011, MNRAS, 61 [3.6.2]

Scannapieco, C., Tissera, P. B., White, S. D. M., & Springel, V. 2006, MNRAS, 371, 1125 [4.2.2]

Schaerer, D., Meynet, G., Maeder, A., & Schaller, G. 1993, A&AS, 98, 523 [2.7.2]

Schlegel, D. J., Finkbeiner, D. P., & Davis, M. 1998, ApJ, 500, 525 [2.7.2]

Schruba, A., Leroy, A. K., Walter, F., Sandstrom, K., & Rosolowsky, E. 2010, ApJ, 722, 1699 [1.3, 4.3.2]

Schruba, A., Leroy, A. K., Walter, F., et al. 2011a, AJ, 142, 37 [1.1]

—. 2011b, AJ, 142, 37 [1.3]

Shu, F. H. 1977, ApJ, 214, 488 [2.4.5]

—. 1992, Physics of Astrophysics, Vol. II [3.3.2]

Simpson, C. M., Bryan, G. L., Hummels, C., & Ostriker, J. P. 2014, ArXiv e-prints, arXiv:1410.3822 [4.2.2, 4.2.2]

Smith, R. J., Glover, S. C. O., Clark, P. C., Klessen, R. S., & Springel, V. 2014, MNRAS, 441, 1628 [1.2]

Solomon, P. M., Rivolo, A. R., Barrett, J., & Yahil, A. 1987, ApJ, 319, 730 [2.4.1, 2.7.1, 2.7.1, 2.7, 2.7.1]

Spitoni, E., & Matteucci, F. 2011, A&A, 531, A72 [1.1]

Springel, V., Di Matteo, T., & Hernquist, L. 2005, MNRAS, 361, 776 [3.2.1, 3.2.1, 4.2.1]

Springel, V., & Hernquist, L. 2003, MNRAS, 339, 289 [4.2.2]

Stahler, S. W., Shu, F. H., & Taam, R. E. 1980, ApJ, 241, 637 [2.3]

Stark, A. A., & Lee, Y. 2006, ApJ, 641, L113 [1.3]

Stilp, A. M., Dalcanton, J. J., Skillman, E., et al. 2013, ApJ, 773, 88 [1.1]

Stinson, G., Seth, A., Katz, N., et al. 2006, MNRAS, 373, 1074 [4.2.2]

Stone, J. M., Ostriker, E. C., & Gammie, C. F. 1998, ApJ, 508, L99 [1.3, 2.4.3, 2.4.3]

Strong, A. W., & Mattox, J. R. 1996, A&A, 308, L21 [2.7.1]

Tamburro, D., Rix, H.-W., Leroy, A. K., et al. 2009, AJ, 137, 4424 [1.1, 3.6.1]

Tamburro, D., Rix, H.-W., Walter, F., et al. 2008, AJ, 136, 2872 [1.3]

Tan, J. C., Krumholz, M. R., & McKee, C. F. 2006, ApJ, 641, L121 [1.3]

Tan, J. C., & McKee, C. F. 2004, ApJ, 603, 383 [2.4.5]

Tasker, E. J. 2011, ApJ, 730, 11 [1.2, 2.4.5, 3.2.5]

Tasker, E. J., & Tan, J. C. 2009, ApJ, 700, 358 [1.2, 1.3, 3.2.2]

Tasker, E. J., Wadsley, J., & Pudritz, R. 2015, ApJ, 801, 33 [1.2]

The Enzo Collaboration, Bryan, G. L., Norman, M. L., O'Shea, B. W., et al. 2014, ApJS, 211, 19 [3.2, 3.2.3, 3.2.4, 3.2.5]

Thilker, D. A., Braun, R., & Walterbos, R. A. M. 2002, in Astronomical Society of the Pacific Conference Series, Vol. 276, Seeing Through the Dust: The Detection of HI and the Exploration of the ISM in Galaxies, ed. A. R. Taylor, T. L. Landecker, & A. G. Willis, 370 [2.4.5]

Thompson, T. A., Quataert, E., & Murray, N. 2005, ApJ, 630, 167 [3.6.1]

Toomre, A. 1964, ApJ, 139, 1217 [1.2, 3.5.1]

Tremonti, C. A., Heckman, T. M., Kauffmann, G., et al. 2004, ApJ, 613, 898 [1.1]

Troland, T. H., & Crutcher, R. M. 2008, ApJ, 680, 457 [2.8.2]

Truelove, J. K., Klein, R. I., McKee, C. F., et al. 1998, ApJ, 495, 821 [3.2.3]

Turk, M. J., Smith, B. D., Oishi, J. S., et al. 2011, ApJS, 192, 9 [3.3]

van Dishoeck, E. F., & Black, J. H. 1988, ApJ, 334, 771 [2.4.6, 2.1]

van Zee, L., & Bryant, J. 1999, AJ, 118, 2172 [1.1]

Vázquez, G. A., & Leitherer, C. 2005, ApJ, 621, 695 [4.2.2]

Vázquez-Semadeni, E., Ballesteros-Paredes, J., & Rodríguez, L. F. 1997, ApJ, 474, 292 [2.8.3]

Vázquez-Semadeni, E., Colín, P., Gómez, G. C., Ballesteros-Paredes, J., & Watson,

A. W. 2010, ApJ, 715, 1302 [1.3]

Vila-Costas, M. B., & Edmunds, M. G. 1992, MNRAS, 259, 121 [1.1]

Wang, B., & Silk, J. 1994, ApJ, 427, 759 [1.2]

Wang, P., & Abel, T. 2008, ApJ, 672, 752 [1.3]

Wang, P., Li, Z.-Y., Abel, T., & Nakamura, F. 2010, ApJ, 709, 27 [2.6.2]

Werk, J. K., Putman, M. E., Meurer, G. R., & Santiago-Figueroa, N. 2011, ApJ, 735, 71 [1.1]

Williams, J. P., & McKee, C. F. 1997, ApJ, 476, 166 [1.3, 2.4.5]

Wise, J. H., & Abel, T. 2007, ApJ, 665, 899 [1.3]

Wolfire, M. G., Hollenbach, D., & McKee, C. F. 2010, ApJ, 716, 1191 [2.4.5, 2.4.6]

Wolfire, M. G., McKee, C. F., Hollenbach, D., & Tielens, A. G. G. M. 2003, ApJ, 587, 278 [4.3.3]

Wong, T., & Blitz, L. 2002, ApJ, 569, 157 [1.3]

Wong, T., Hughes, A., Fukui, Y., et al. 2009, ApJ, 696, 370 [2.4.5]

Yang, C.-C., Gruendl, R. A., Chu, Y.-H., Mac Low, M.-M., & Fukui, Y. 2007, ApJ, 671, 374 [2.4.5]

Zuckerman, B., & Evans, II, N. J. 1974, ApJ, 192, L149 [1.3]